Development of a predictive self-consistent fluid model for optimizing inductive RF coupling of powerful negative hydrogen ion sources

Dissertation

zur Erlangung des akademischen Grades

Dr. rer. nat.

eingereicht an der

Mathematisch-Naturwissenschaftlich-Technischen Fakultät

der Universität Augsburg

von

Dominikus Zielke

Augsburg, Juni 2021

Tag der mündlichen Prüfung: 14.09.2021

Erster Gutachter: apl. Prof. Dr.-Ing. U. Fantz

Zweiter Gutachter: Prof. Dr. L. Chioncel

Dritter Gutachter: Assoc. Prof. S. Lishev, PhD

Abstract

Magnetized confinement fusion devices such as ITER will be heated and fueled by large and powerful neutral beam injection systems, where neutralized negative hydrogen and deuterium ions are used. The negative ions are produced in an ion source plasma, which is sustained by powerful radio-frequency (RF) generators at 1 MHz. The power is transferred by a coil wrapped around a cylinder (called driver) via inductive coupling to the low pressure (up to 0.3 Pa) low temperature plasma. In ion sources used at the ITER neutral beam injection system there will be eight drivers, each powered with up to 100 kW. Voltages of several kilovolts are applied, wherefore electrical breakdowns are likely. Only a certain fraction η of the generator power is absorbed by the plasma, whereas the rest is lost by Joule heating of the coil and metallic components. By maximizing η, lower generator powers and coil voltages become possible. However, various parameters such as magnetic field, pressure, power, driving frequency, as well as driver and coil geometry influence η. To get insight into the power coupling mechanism and to optimize η, a predictive self-consistent fluid model is established. No predictive model existed hitherto due to the complexity of the power coupling at low driving frequencies and the dynamics of the plasma and neutral species at low pressures and high powers. It is shown that the nonlinear RF Lorentz force and the electron viscosity are crucial for describing power coupling in this regime. Model validation is accomplished by systematic comparison with measurements of the plasma and electrical parameters that are performed for the first time at the ITER prototype RF ion source. Here η is around 0.5. The capability of the model to scan the broad parameter space and disentangle the various nonlinear effects provides a valuable guideline for experimental efforts towards optimizing the RF power coupling in ion sources. By optimizing the two parameters with maximum impact, driving frequency and driver length, η is increased from 0.5 to 0.9.

Contents

1 Introduction

Future fusion devices such as ITER [1] will contain magnetically confined plasmas that have to be heated up to temperatures of around 10^8 K. These extreme temperatures are necessary for the nuclear fusion process to happen often enough to harness energy from it [2]. In the ITER experiment fast neutral particles with energies of 1 MeV are injected into the fusion plasma to heat it via collisions [3]. The fast neutral beam is produced from accelerated ions that are subsequently neutralized [4]. For hydrogen at particle energies of 1 MeV it is energetically by far more efficient to strip an electron from a negative ion than adding an electron to a positive ion [5]. For this reason fast **N**eutral **B**eam **I**njection (NBI) systems rely exclusively on **N**egative ions, hence the abbreviation NNBI.

The negative ions are produced in a hydrogen or deuterium low temperature plasma. The plasma is sustained via inductive coupling in a compact cylindrical vessel, called driver. A coil that is wound around the driver produces an electromagnetic field that oscillates at a radio-frequency (RF) of 1 MHz. An internal Faraday screen suppresses capacitive coupling. In this way the cylindrical driver wall is protected from undesired plasma sputtering and subsequent erosion as well as the plasma from pollution. The electric component of the inductive RF field heats the electrons in the plasma, producing typical electron densities and temperatures in the driver of $10^{18}\,\mathrm{m}^{-3}$ and 10 eV, respectively. The plasma expands from the driver into an expansion region. Here negative ions are created on the plasma facing surface of an extraction grid system via conversion of impinging atoms and positive ions. The negative ion yield is considerably enhanced when the surface is covered by a thin cesium layer with a low work function [6]. This is ensured by evaporating cesium into the ion source. A low gas pressure of 0.3 Pa is necessary to reduce the losses of negative ions in the extraction grid system [3]. The ion source design for the ITER experiment is based on the reference RF ion source which has

been developed at the Max-Planck-Institut für Plasmaphysik and is in operation at the BUG (1/8 of ITER ion source size) and ELISE (1/2 of ITER ion source size) test beds in Garching [7–10].

For ITER, among several other challenges such as producing a uniform high current (tens of Ampères) beam, while efficiently suppressing co-extracted electrons (especially in deuterium), pulse lengths of up to one hour are required [3, 11–13]. Throughout the full pulse length the NNBI systems have to operate reliably. Each NNBI system has one ion source with eight modular drivers attached to it. The ion source is powered by a total amount of 800 kW, i.e. 100 kW are used per driver. The high powers are associated with large currents well above 100 A and high voltages of around 10 kV. At these high voltages electrical breakdowns and subsequent arcs are likely. As a consequence, the RF coil and the driver could be destroyed resulting in outages and a decreased reliability of the whole NNBI system. For this reason it is desirable to reduce the generator power and thereby the currents and voltages.

It is well known that in inductively coupled plasmas a certain fraction of the generator power is not coupled to the plasma. This power is mainly lost by eddy currents in conductive components such as the Faraday screen as well as by direct Joule heating of components in the matching network and in the RF coil [14–17]. A quantity to describe the fraction of power that is absorbed by the plasma is the *RF power transfer efficiency*

$$\eta = \frac{P_{\text{plasma}}}{P_{\text{generator}}}, \tag{1.1}$$

where P_{plasma} and $P_{\text{generator}}$ are the power absorbed by the plasma and the generator output power, respectively. The goal is to minimize $P_{\text{generator}}$ while retaining P_{plasma}, i.e. η has to be maximized. Various external parameters such as the applied frequency and power, pressure, gas type (hydrogen or deuterium), and also driver geometry and RF coil layout affect η. Also magnetostatic fields present in the ion source influence η. By means of experiments alone it is hardly possible to systematically investigate this broad parameter space and even impossible to study some of the fundamental physical effects that take place in the discharge. However, this is possible by numerical modeling.

A predictive numerical model of the ion source has to be self-consistent. This means that it must account for the bidirectional coupling between the plasma and the RF fields in time and space. The ion source operates in an unusual regime, i.e. the driving frequency is 1 MHz, which is low compared to the standard frequency of 13.56 MHz, where most inductively coupled plasmas in industrial applications are operated. This low frequency together with the high applied power levels lead to nonlinear effects in the RF coupling mechanism. In addition, the required low pressure of 0.3 Pa results in complex plasma and neutrals dynamics.

First modeling steps have been taken by several authors, where basic simplified systems and different approximations regarding the gas discharge part and the RF power coupling mechanism have been used [18–23]. However, none of these models is self-consistent, mainly because important aspects in the description of the RF power coupling are still missing. Moreover, the RF power coupling mechanisms implemented in these models have not been validated with experimental measurements, which is a necessary step before a model can be considered predictive.

Consequently, the goal of this work is to develop a predictive numerical model that self-consistently simulates the inductive power coupling in RF ion sources. To achieve this, an appropriate modeling approach has to be chosen at first. For this purpose existing state-of-the-art models from the literature are reviewed and their limitations identified. For the validation of the implemented RF power coupling mechanism, calculations with different approximations of the model equations are compared to electrical and plasma parameter measurements from an RF ion source. In this way the various interacting nonlinear mechanisms that influence the RF power coupling can be studied in detail. After the validation, the predictive model can be applied to identify the parameters that optimize the RF power coupling.

2 Fundamentals

2.1 RF-driven ion sources for negative hydrogen ions

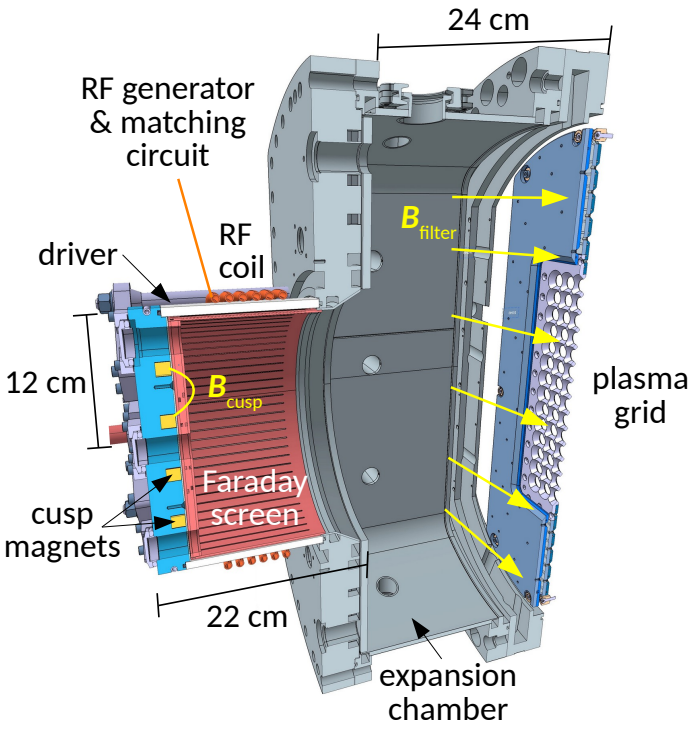

Figure 2.1: *Schematic representation of the ITER prototype RF ion source at the BUG test bed, which is 1/8 of the full ITER ion source. Figure adapted from [24].*

Figure 2.1 shows a schematic representation of the ITER prototype RF ion source, which is operated at the BUG test bed [9]. A low temperature hydrogen or deuterium plasma is produced by inductive RF power coupling in a cylindrical vessel, called driver, where typical electron temperatures and densities are 10 eV and

$10^{18}\,\mathrm{m}^{-3}$, respectively [24]. The plasma confinement in the driver is improved by cusp magnets that are located in the driver back plate [25]. The highly non-uniform cusp field $\boldsymbol{B}_{\mathrm{cusp}}$ decreases from around 500 G directly at the driver back plate to 5 G in the center of the driver, as shown in figure 4.12. At its open side the driver is connected to an expansion chamber into which the plasma expands. Negative ions are mainly produced at the surface of the plasma grid by conversion of impinging atoms and positive ions [26]. Cesium is evaporated into the expansion chamber to reduce the work function of the plasma grid and thus improve the conditions for the surface production of negative ions [27]. The filling pressure, i.e. the pressure of the neutral molecules before plasma formation (cf. equation (2.16)), is measured at several positions in the ion source [28]. Its upper limit for an ion source at ITER is 0.3 Pa, because at this pressure the losses of negative ions by collisions with the background gas (neutrals stripping losses) were estimated not to exceed 30% in the ITER extraction system [29]. A magnetic filter field $\boldsymbol{B}_{\mathrm{filter}}$ of around 50 G in front of the plasma grid reduces the electron temperature there to values below 2 eV [30], at which negative ion losses by electron stripping are effectively suppressed [31]. At the same time the magnetic filter decreases the number of co-extracted electrons by decreasing the electron density in front of the plasma grid [32].

RF generator output powers of up to 100 kW at a driving frequency of 1 MHz are applied to reach discharge parameters that are sufficient for producing the amount of negative ions that complies with the need for heating and fueling of an ITER fusion plasma. The high generator output powers are associated with voltages of several kilovolts, where a considerable strain is imposed on the RF components such as the coil, the internal Faraday screen, the matching network and on the RF generator. Even though the individual coil windings are protected by an isolation oil with a high dielectric strength, electrical breakdowns are still a severe problem, since they can lead to electric arcs that form e.g. between the individual coil windings or between the coil and the surrounding metallic structure. The consequences of electric arcs are potential catastrophic failures and fire hazards in the ion source, wherefore a reliable operation of the whole neutral beam injection system is at risk.

2.2 Low temperature hydrogen plasmas

In this section no specific distinction is made between hydrogen and its isotope deuterium, i.e. if not specifically mentioned otherwise, hydrogen can as well be replaced by deuterium.

Distribution function, temperature and mean free path

A plasma is an ionized gas, wherefore the kinetic theory of gases is well suited to describe it [33, 34]. The fundamental object that characterizes a particle species α in a plasma is its distribution function f_α. If the particles within the species α are in thermal equilibrium, then $f_{\alpha,\mathrm{m}}$ is a Maxwell-Boltzmann distribution function

$$f_{\alpha,\mathrm{m}}(\boldsymbol{r},\boldsymbol{v},t)\,\mathrm{d}^3\boldsymbol{v} = \frac{n_\alpha}{\pi^{3/2}v_{\alpha,\mathrm{p}}^3}\exp\left(-\frac{|\boldsymbol{v}|^2}{v_{\alpha,\mathrm{p}}^2}\right)\mathrm{d}^3\boldsymbol{v} \tag{2.1}$$

with the number density n_α and the most probable speed

$$v_{\alpha,\mathrm{p}} = \left(\frac{2k_\mathrm{B}T_\alpha}{m_\alpha}\right)^{1/2}, \tag{2.2}$$

where k_B denotes the Boltzmann constant. In this case the distribution of particle velocities is fully determined by the mass m_α and the temperature T_α, which is measured in Kelvin. The distribution function $f_{\alpha,\mathrm{m}}$ is normalized, such that $\iiint f_{\alpha,\mathrm{m}}\,\mathrm{d}^3\boldsymbol{v} = n_\alpha$. The local flux as a consequence of the thermal particle motion that crosses any particular plane is calculated as

$$n_\alpha u_{\alpha,\mathrm{eff}} = \int_{-\infty}^{\infty}\mathrm{d}v_x\int_{-\infty}^{\infty}\mathrm{d}v_y\int_{0}^{\infty}\mathrm{d}v_z v_z f_{\alpha,\mathrm{m}}(\boldsymbol{r},\boldsymbol{v},t) = n_\alpha\frac{v_{\alpha,\mathrm{p}}}{2\pi^{1/2}}. \tag{2.3}$$

Here the flux in the positive z direction and hence the $x-y$ plane are chosen without loss of generality. Since $f_{\alpha,\mathrm{m}}$ does not depend on the velocity $\boldsymbol{v}$ but only on the speed $v = |\boldsymbol{v}|$, one can integrate over the solid angle and derive a distribution function for the speeds as

$$f_{\alpha,\mathrm{m}}(\boldsymbol{r},v,t)\,\mathrm{d}v = n_\alpha\frac{4\pi v^2}{\pi^{3/2}v_{\alpha,\mathrm{p}}^3}\exp\left(-\frac{v^2}{v_{\alpha,\mathrm{p}}^2}\right)\mathrm{d}v. \tag{2.4}$$

From equation (2.4) it becomes evident, why $v_{\alpha,\mathrm{p}}$ is called the most probable speed, since it can be calculated from

$$\frac{\partial f_{\alpha,\mathrm{m}}}{\partial v} = 0 \Leftrightarrow v = v_{\alpha,\mathrm{p}}. \tag{2.5}$$

The average or also called thermal speed $v_{\alpha,\mathrm{th}}$ is calculated as

$$v_{\alpha,\mathrm{th}} = \frac{1}{n_\alpha}\int_0^\infty v f_{\alpha,\mathrm{m}}\,\mathrm{d}v = \frac{2}{\pi^{1/2}} v_{\alpha,\mathrm{p}} \overset{(2.2)}{=} \left(\frac{8 k_\mathrm{B} T_\alpha}{\pi m_\alpha}\right)^{1/2}. \tag{2.6}$$

Another variable transformation

$$\epsilon = \frac{m_\alpha}{2} v^2 \tag{2.7}$$

yields the distribution function of the particle energies

$$f_{\alpha,\mathrm{m}}(\boldsymbol{r}, \epsilon, t)\,\mathrm{d}\epsilon = n_\alpha \frac{2}{\pi^{1/2}\epsilon_{\alpha,\mathrm{p}}^{3/2}} \epsilon^{1/2} \exp\left(-\frac{\epsilon}{\epsilon_{\alpha,\mathrm{p}}}\right)\mathrm{d}\epsilon, \tag{2.8}$$

where the energy associated with the most probable speed is

$$\epsilon_{\alpha,\mathrm{p}} = \frac{m_\alpha}{2} v_{\alpha,\mathrm{p}}^2 \overset{(2.2)}{=} k_\mathrm{B} T_\alpha. \tag{2.9}$$

With equations (2.8) and (2.9) the thermal energy is calculated as

$$\epsilon_{\alpha,\mathrm{th}} = \frac{1}{n_\alpha}\int_0^\infty \epsilon f_{\alpha,\mathrm{m}}\mathrm{d}\epsilon = \frac{3}{2} k_\mathrm{B} T_\alpha. \tag{2.10}$$

In a plasma there are charged particles such as free electrons and ions as well as neutral particles. The electrons in an inductively coupled plasma are directly heated by the RF electric field, as further explained in section 2.3. Therefore T_e reaches high values around 10 eV. Note that the electron temperature is expressed in electron volts in this work. The conversion to Kelvin is given by the relation

$$k_\mathrm{B} T_\alpha^{[\mathrm{K}]} = \mathrm{e} T_\alpha^{[\mathrm{eV}]}, \tag{2.11}$$

where e denotes the elementary charge. Hence T_e expressed in Kelvin is approximately $1.16 \cdot 10^5\,\mathrm{K}$. Collisions between the electrons and the heavy particles are typically not frequent enough at gas pressures below 1 Pa, wherefore the different particle species are not in thermal equilibrium among each other. Since ions and neutrals are not directly heated by the RF electric field, they remain at a few 1000 K or colder [33]. Note that heavy species temperatures are expressed in Kelvin in this work.

As at the low pressures there are not enough collisions to randomize the particles velocities, sometimes not even the species α itself is in thermal equilibrium. A measure for estimating the efficiency of the Maxwellianization process is the *mean free path*

$$\lambda_{\alpha,\mathrm{mfp}} = \frac{v_{\alpha,\mathrm{th}}}{\nu_{\alpha,\mathrm{n}}}, \tag{2.12}$$

where $\nu_{\alpha,\mathrm{n}}$ is the collision frequency of species α and the neutrals, as defined in equation (3.16). If $\lambda_{\alpha,\mathrm{mfp}}$ is small compared to the typical discharge size, the distribution function is a Maxwellian. However, at low pressures the mean free paths of all particles becomes comparable or even larger than the discharge size [35]. In this case the distribution function can substantially deviate from a Maxwellian. To approximately describe this situation analytically, a multi-Maxwellian $f_{\alpha,\mathrm{mm}}$ with s individual ensembles

$$f_{\alpha,\mathrm{mm}}(\boldsymbol{r},\epsilon,t)\,\mathrm{d}\epsilon = \sum_{j=1}^{s} x_j n_j \frac{2}{\pi^{1/2}\epsilon_{\alpha,\mathrm{p}_j}^{3/2}} \epsilon^{1/2} \exp\left(-\frac{\epsilon}{\epsilon_{\alpha,\mathrm{p}_j}}\right) \mathrm{d}\epsilon \tag{2.13}$$

can be used, where $\sum_{j=1}^{s} x_j = 1$ and $\sum_{j=1}^{s} x_j n_j = n_\alpha$ to properly normalize the distribution function.

Ionization degree and neutral depletion

The *ionization degree* χ of a low temperature plasma is typically rather low [33], i.e. in hydrogen

$$\chi = \frac{\sum_\mathrm{i} n_\mathrm{i}}{\sum_\mathrm{i} n_\mathrm{i} + n_\mathrm{n}} \lesssim 0.1, \tag{2.14}$$

where $\mathrm{i} \in \{\mathrm{H}^+, \mathrm{H}_2^+, \mathrm{H}_3^+\}$ and $\mathrm{n} \in \{\mathrm{H}, \mathrm{H}_2\}$. The *total pressure*

$$p = n_\mathrm{e} \mathrm{e} T_\mathrm{e} + \sum_\mathrm{i} n_\mathrm{i} k_\mathrm{B} T_\mathrm{i} + \sum_\mathrm{n} n_\mathrm{n} k_\mathrm{B} T_\mathrm{n} \tag{2.15}$$

is the sum of the partial pressures of all species in the plasma. In contrast to that the *filling pressure*

$$p_\mathrm{fill} = n_{\mathrm{H}_2} k_\mathrm{B} T_{\mathrm{H}_2} \tag{2.16}$$

is the pressure of the molecules before plasma ignition. For electron densities and temperatures of around $10^{18}\,\mathrm{m}^{-3}$ and 10 eV respectively, the electron pressure can contribute significantly to the total pressure, especially when the ionization degree is around 0.1 [28]. In this case a phenomenon called neutral depletion occurs. Hereby the molecular neutral density is considerably decreased during plasma operation compared to the one before the presence of plasma. Main reasons for neutral depletion are ionization and gas heating [36].

The free electrons and ions in a plasma react to electric and magnetic fields, wherefore the plasma exhibits collective behavior (as opposed to a gas). The most important consequences of this remarkable feature are introduced in the following.

Static shielding and quasi-neutrality

Due to their large mobility the free electrons in the plasma shield an electrostatic field introduced by any net charge [37]. The length scale of this static shielding is the *Debye length*

$$\lambda_\mathrm{De} = \left(\frac{\epsilon_0 T_\mathrm{e}}{\mathrm{e} n_\mathrm{e}} \right)^{1/2}, \tag{2.17}$$

where ϵ_0 denotes the vacuum permittivity. In a typical low temperature plasma with $T_\mathrm{e} \approx 10\,\mathrm{eV}$ and $n_\mathrm{e} \approx 10^{18}\,\mathrm{m}^{-3}$ equation (2.17) yields $\lambda_\mathrm{De} \approx 20\,\mu\mathrm{m}$. On length scales L being large compared to λ_De, the bulk of the plasma is free of large electric

potentials or fields, wherefore the plasma is considered *quasi-neutral* for $L \gg \lambda_{\mathrm{De}}$, i.e. to a good approximation

$$\sum_{\mathrm{i}} n_{\mathrm{i}} \approx n_{\mathrm{e}} \tag{2.18}$$

is fulfilled [37], where n_{i} denotes the ion number density. A typical hydrogen low temperature plasma consists of three different positive ion species $\mathrm{i} \in \{\mathrm{H}^+, \mathrm{H}_2^+, \mathrm{H}_3^+\}$ [31].

Plasma sheath

The plasma shields itself electrostatically against any bulk object that is introduced into it, such as e.g. a probe or wall. The plasma electrons have lower mass and higher temperature than the ions, wherefore initially the electron thermal flux towards the bulk object according to equation (2.3) is considerably larger than the corresponding ion flux. For this reason negative space charge accumulates at the bulk object, wherefore a potential drop evolves. Subsequent electrons are retarded by the electrostatic field that is created by the space charge, whereas ions are accelerated towards the bulk object. Hence the drop of the electron density towards the bulk object is more pronounced than the one of the ion density. In this way a plasma sheath forms with a characteristic length scale of around 100 µm, i.e. several Debye lengths. Within the plasma sheath, the plasma is not quasi-neutral. In hydrogen plasmas, the potential drop is around four times the electron temperature, i.e. an electron temperature of 10 eV produces a potential drop of around 40 V [33]. When leaving the quasi-neutral plasma the ions are accelerated to at least the Bohm speed

$$u_{\mathrm{i,Bohm}} = \left(\frac{\mathrm{e}T_{\mathrm{e}}}{m_{\mathrm{i}}}\right)^{1/2}. \tag{2.19}$$

In equation (2.19) only one positive ion species with mass m_{i} is assumed for simplicity. In a plasma with multiple ion species the more complicated generalized Bohm criterion has to be applied [38].

Wall processes

Electrons and ions produced in the plasma volume are mainly lost at the discharge walls, where they recombine to neutral particles that enter the discharge [39]. This recombination mechanism couples the ion and neutral particle- as well as energy-fluxes. Typically a fraction of the energy inherent in the directed ion motion (gained in the plasma sheath) is converted into thermal energy of the neutrals, which facilitates heating of the latter [22].

Magnetostatic fields

A charged particle of species α is magnetized, if a magnetic field $\boldsymbol{B}$ is strong enough to significantly alter its trajectory. To make this statement quantitative, the *Larmor radius*

$$\rho_{\alpha,\mathrm{Larmor}} = \frac{m_\alpha v_{\alpha,\mathrm{p}}}{q_\alpha |\boldsymbol{B}|} \tag{2.20}$$

and the *cyclotron frequency*

$$\omega_{\alpha,\mathrm{c}} = \frac{q_\alpha |\boldsymbol{B}|}{m_\alpha} \tag{2.21}$$

need to be introduced, where q_α denotes the particle's charge. Using these definitions, a particle is considered magnetized if the two conditions

$$\rho_{\alpha,\mathrm{Larmor}} \ll L \quad \text{and} \quad \omega_{\alpha,\mathrm{c}} \gg \nu_{\alpha,\mathrm{n}} \tag{2.22}$$

are fulfilled [40]. This means that the Larmor radius must be small compared to the discharge size L. At the same time the cyclotron frequency must be large compared to the elastic momentum transfer collision frequency $\nu_{\alpha,\mathrm{n}}$. By defining the *Hall parameter*

$$h_\alpha = \frac{\omega_{\alpha,\mathrm{c}}}{\nu_{\alpha,\mathrm{n}}} = \mu_\alpha |\boldsymbol{B}|, \tag{2.23}$$

where the mobility is $\mu_\alpha = q_\alpha m_\alpha^{-1} \nu_{\alpha,\mathrm{n}}^{-1}$, one can rewrite the condition $\omega_{\alpha,\mathrm{c}} \gg \nu_{\alpha,\mathrm{n}}$ as $h_\alpha \gg 1$.

Magnetic fields typically encountered in an ion source plasma are in the order of 50 G [41]. At these field strengths electrons are fully magnetized, since the electron Larmor radius is only several millimeters and thus considerably smaller than the typical discharge size (cf. figure 2.1). The electron cyclotron frequency is in the range of GHz and thus around three orders of magnitude larger than $\nu_{\mathrm{e,n}}$. For the ions the situation is ambiguous, depending on the ion mass and temperature. Here the Larmor radius is in the range of centimeters, beeing smaller than the typical discharge size. However, the ion cyclotron frequency is around 0.1 MHz, which is comparable to $\nu_{\mathrm{i,n}}$ [42]. For this reason the ions are not fully magnetized.

2.3 Inductive power coupling

Figure 2.2 shows the simplified RF circuit of the BUG ion source. Depicted on

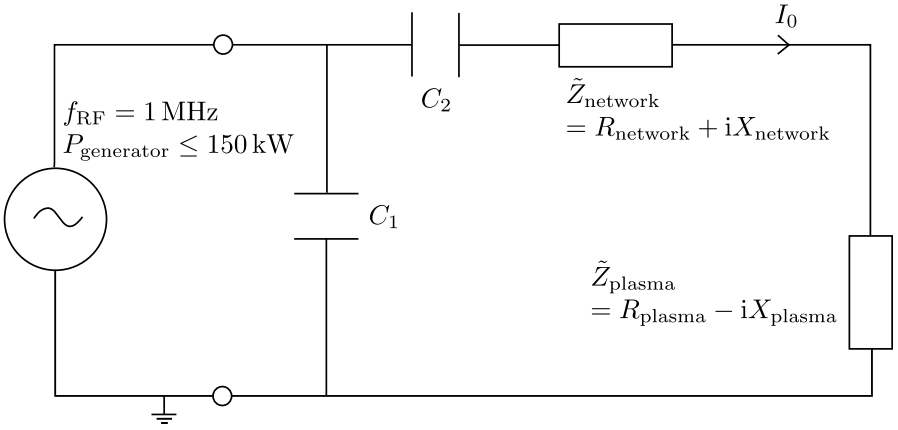

Figure 2.2: *Simplified electrical circuit of the BUG ion source with the RF power generator on the left and the RF circuit on the right.*

the left is the RF generator that is designed to operate at a driving frequency of 1 MHz with a maximum output power of 150 kW [43]. However, the ion source is usually operated at lower generator powers up to 80 kW, because at higher powers electrical breakdowns and arcing become likely. The ion source is at a high potential around 60 kV to accelerate the negative ions in the extraction system [8]. At ITER, the RF generator and circuit will be on the same potential as the ion source [4]. In contrast to that at the BUG test bed the RF generator is on ground

potential. This saves space and eases the power that has to be supplied via a high voltage transformer. One drawback of this solution is that an additional matching transformer is required to electrically isolate the grounded generator from the ion source [7, 44]. This matching transformer is subject to nonlinear magnetization losses in its ferrite core, which have been experimentally quantified in a separate study [24]. Consequently, it is neither used in the experimental setup, nor is it modeled in this work.

The RF circuit consists of two air cooled matching capacitors C_1 and C_2 that are used for impedance matching, i.e. they are adjusted such that the equivalent resistance of the RF circuit, as presented to the RF generator at its output is $50\,\Omega$ [45, 46]. In this way it is ensured that no power is reflected from the RF circuit that could destroy the generator. The network losses in the RF coil, Faraday screen (both water cooled) and other surrounding structure are described by R_{network}, whereas the inductive reactance X_{network} is generated by the RF coil and slightly reduced by the Faraday screen. The complex quantity $\tilde{Z}_{\mathrm{plasma}}$ models the inductively coupled plasma, wherefore it consists of a real part that is responsible for power absorption and an imaginary part that accounts for the inductive behavior of the plasma. Note that X_{plasma} slightly decreases the total reactive inductance in the branch of the RF coil [47]. The amplitude of the current flowing through the RF coil is denoted by I_0. The RF coil 'antenna' length is small compared to the wavelength (which is 300 m at 1 MHz), wherefore the electromagnetic wave that is transmitted outside the coil is negligible. For this reason no power is lost via electromagnetic radiation.

From the RF circuit in figure 2.2 follows that the generator output power must be dissipated either in the plasma or in the RF network, i.e.

$$P_{\mathrm{generator}} = P_{\mathrm{plasma}} + \frac{1}{2} R_{\mathrm{network}} I_0^2. \tag{2.24}$$

With this equation and with $P_{\mathrm{plasma}} = \frac{1}{2} R_{\mathrm{plasma}} I_0^2$ follows for the *RF power transfer efficiency*

$$\eta = \frac{P_{\mathrm{plasma}}}{P_{\mathrm{generator}}} = \frac{R_{\mathrm{plasma}}}{R_{\mathrm{plasma}} + R_{\mathrm{network}}}. \tag{2.25}$$

Note that R_{network} and R_{plasma} are independent of each other. Hence, to increase η, R_{network} must be decreased and R_{plasma} must be increased. At the same time electric arcs in the RF coil and the surrounding metallic structure have to be avoided. For this reason optimization measures target not only to increase η but also to decrease the *effective coil voltage*

$$U_{\text{coil,eff}} = |\tilde{Z}_{\text{network}} + \tilde{Z}_{\text{plasma}}| \cdot \frac{I_0}{\sqrt{2}} \approx \omega_{\text{RF}} L_{\text{network}} \frac{I_0}{\sqrt{2}}, \tag{2.26}$$

which causes the arcs. Herein the approximations $R_{\text{network}}, R_{\text{plasma}} \ll \omega_{\text{RF}} L_{\text{network}}$ and $X_{\text{network}} \gg X_{\text{plasma}}$ are used. The first approximation is well fulfilled, since typically $R_{\text{network}}, R_{\text{plasma}} < 1\,\Omega$ and $L_{\text{network}} > 10\,\mu\text{H}$ resulting in $\frac{R_{\text{network}}}{\omega_{\text{RF}} L_{\text{network}}} < \frac{1}{10 \cdot 2\pi} \approx 0.01 \ll 1$ at 1 MHz. The second approximation cannot be justified without further information about the plasma. However, since X_{plasma} acts to decrease the total reactive inductance, equation (2.26) approximates the worst case, i.e. the highest coil voltage.

2.3.1 Network losses

The network losses consist of two parts: (i) Joule heating of the RF coil, where an RF current is directly applied and (ii) Joule heating of the Faraday screen and the back plates, where eddy currents are induced by the time varying magnetic field that is generated by the current in the RF coil. At radio-frequencies there is a pronounced skin effect, i.e. the RF current is pushed towards the outside of a conductor and transported through a *skin depth* [48]

$$\delta_{\text{RF,conductor}} = \left(\frac{2}{\mu_0 \mu_r \omega_{\text{RF}} \sigma_{\text{conductor}}} \right)^{1/2}. \tag{2.27}$$

Herein μ_0, μ_r, $\omega_{\text{RF}} = 2\pi f_{\text{RF}}$ and $\sigma_{\text{conductor}}$ denote vacuum and relative permeability, angular frequency and material specific electric conductivity, respectively. The RF coil as well as the Faraday screen are made out of copper, where with $\sigma_{\text{copper}} =$

$5.9 \cdot 10^7\,\mathrm{Sm}^{-1}$ [49] and equation (2.27) follows $\delta_{\mathrm{RF,copper}} = 65\,\mu\mathrm{m}$ at 1 MHz. A lumped resistance is calculated as

$$R = \frac{l}{\sigma A}, \tag{2.28}$$

where l and A denote the length and the surface (assumed constant) through which the RF current is transported, respectively. For a cylindrical tube of known dimensions the surface A is determined via the skin depth, i.e. $A \approx 2\pi r_{\mathrm{tube}}\delta_{\mathrm{RF}}$. The absorbed power by Joule heating in the conductor is then straight forwardly determined by using the standard text book formula $P = \frac{1}{2}RI_0^2$ [48], where I_0 is the applied RF current amplitude. To calculate the induced eddy currents, Ampère's circuital law and Faraday's law of induction have to be solved taking the full 3D geometry of the RF coil, Faraday screen and back plates into account.

2.3.2 RF power coupling to plasma

In contrast to the modeling of the network resistance, modeling the RF power coupling in a plasma is considerably more complicated. The starting point for the power coupling in an inductively coupled plasma is a current density that oscillates harmonically with an applied angular frequency ω_{RF} along a conductive tube. According to Ampère's law this time dependent current density generates an oscillating magnetic field surrounding the tube. This time-dependent magnetic field in turn produces an electric field via Faraday's law of induction. The maximum frequency of an external field up to which the free electrons in the plasma can respond is the *plasma frequency* [33]

$$\omega_{\mathrm{e,p}} = \left(\frac{\mathrm{e}^2 n_{\mathrm{e}}}{\epsilon_0 m_{\mathrm{e}}}\right)^{1/2}. \tag{2.29}$$

Using $n_{\mathrm{e}} \approx 10^{18}\,\mathrm{m}^{-3}$ yields $\omega_{\mathrm{e,p}} \approx 50\,\mathrm{GHz}$. Since this frequency is around four orders of magnitude larger than the applied $\omega_{\mathrm{RF}} = 2\pi \cdot 1\,\mathrm{MHz}$ the electrons are able to respond to the RF field and thus dynamically shield the plasma from external RF fields.

Also the free ions in the plasma can follow the electric RF field, i.e. as for the electrons $\omega_{\mathrm{RF}} \ll \omega_{\mathrm{i,p}} \approx 10^9\,\mathrm{Hz}$ is true. However, from equation (2.32) it becomes evident why the ion's contribution to the RF current density and thus to the inductive power coupling is nevertheless negligible. The main reason is the comparatively larger ion mass, i.e. the ion contribution to the plasma conductivity $\tilde{\sigma}_{\mathrm{plasma}}$ is reduced by a factor of $\frac{m_{\mathrm{i}}}{m_{\mathrm{e}}} \approx 1800$ compared to the one of the electrons. For this estimation $n_{\mathrm{e}} \approx n_{\mathrm{i}}$ and $\nu_{\mathrm{e,n}} \approx 10 \cdot \nu_{\mathrm{i,n}}$ are used, where the elastic collision cross sections are obtained from the references given in table 3.2. Hence only the inductive electron heating is of practical interest in the following discussion.

Assuming a local collisional regime in the plasma, this results in a transverse electromagnetic wave, i.e. the complex wave vector $\tilde{\boldsymbol{k}}$ that indicates the direction of propagation and the direction of the electric and magnetic RF field are pairwise perpendicular. The associated *dispersion relation* reads [33]

$$\tilde{k} = \pm\frac{\omega_{\mathrm{RF}}}{c_0}\tilde{\epsilon}_r^{1/2}. \tag{2.30}$$

Herein c_0, $\tilde{k}$ and $\tilde{\epsilon}_r$ denote the speed of light in vacuum, the complex amplitude of the wave vector $\tilde{\boldsymbol{k}}$ and the complex *relative dielectric permittivity*, respectively. The latter is defined as [33]

$$\tilde{\epsilon}_r = 1 - \mathrm{i}\frac{\tilde{\sigma}_{\mathrm{plasma}}}{\epsilon_0\omega_{\mathrm{RF}}}, \tag{2.31}$$

where the complex *electrical plasma conductivity*

$$\tilde{\sigma}_{\mathrm{plasma}} = \frac{\mathrm{e}^2 n_{\mathrm{e}}}{m_{\mathrm{e}}\left(\mathrm{i}\omega_{\mathrm{RF}} + \nu_{\mathrm{e,n}}\right)} \tag{2.32}$$

from the collisional cold plasma approximation [33] is used. Since the wave cannot propagate because of $\omega_{\mathrm{RF}} \ll \omega_{\mathrm{e,p}}$, it follows the classical RF skin effect, where the electric and magnetic RF field amplitudes are exponentially damped in the *RF skin depth* [33]

$$\delta_{\mathrm{RF}} = \frac{1}{|\mathrm{Im}\{\tilde{k}\}|}. \tag{2.33}$$

In the context of a plasma, δ_{RF} is also called thickness of the RF sheath. Typical values are $\delta_{\mathrm{RF}} \approx 5\,\mathrm{mm}$, which is more than one order of magnitude larger than the thickness of the plasma sheath. Note that equation (2.27) follows as an approximation of equation (2.33) for the case of a good conductor, where $\sigma_{\mathrm{conductor}}$ has no imaginary part.

The electric field component $\boldsymbol{E}$ of the RF field exerts a force $\boldsymbol{F} = -\mathrm{e}\boldsymbol{E}$ on the free electrons in the plasma. Applying this force along some displacement $\mathrm{d}\boldsymbol{x}$ yields the amount of work that is done. From this follows the instantaneous power absorbed by the electron as the work done per time

$$P = \frac{\mathrm{d}W}{\mathrm{d}t} = \frac{\boldsymbol{F} \cdot \mathrm{d}\boldsymbol{x}}{\mathrm{d}t} = -\mathrm{e}\boldsymbol{E} \cdot \boldsymbol{v}. \tag{2.34}$$

For $\boldsymbol{E}$ and the electron velocity $\boldsymbol{v}$ oscillating with angular frequency ω_{RF}, the average power over one period can be expressed as [48]

$$P_{\mathrm{av}} = \frac{\omega_{\mathrm{RF}}}{2\pi} \int_0^{2\pi/\omega_{\mathrm{RF}}} -\mathrm{e}\boldsymbol{E} \cdot \boldsymbol{v}\, \mathrm{d}t = \frac{1}{2}\mathrm{Re}\{-\mathrm{e}\tilde{\boldsymbol{E}} \cdot \tilde{\boldsymbol{v}}^*\}, \tag{2.35}$$

where the tilde indicates a complex amplitude and the asterisk denotes complex conjugation. In the picture of a forced harmonic oscillator applying a harmonic external electric force to a particle results in a harmonic oscillation of the latter. In this case a phase difference of 90° between the electric field component and the particle velocity sets in and according to equation (2.35) no average power is absorbed over the course of one period.

One mechanism that leads to power absorption are collisions, i.e. by introducing collisions in the simple picture of the forced harmonic oscillator, the 90° phase shift is reduced and thus power is absorbed, as is evident from equation (2.35). This well known phenomena is dominating in local conditions when there are enough particles for the oscillating electron to collide with. In this case local Ohm's law evolves and the current density is directly connected to the electric field via the plasma conductivity from equation (2.32). The resulting heating region is confined to the classical collisional RF sheath δ_{RF}, as introduced in equation (2.33) [33].

2.3.3 RF skin effect and heating regimes

Figure 2.3 shows the three different RF skin effect regimes that can be observed in an inductively coupled plasma depending on the filling pressure p_{fill} and magnetic RF field strength B_{RF}. The idea for this figure is from [50], where B_{RF} is plotted over a changing driving frequency. However, collisions are not accounted for in [50], whereas they are retained in figure 2.3.

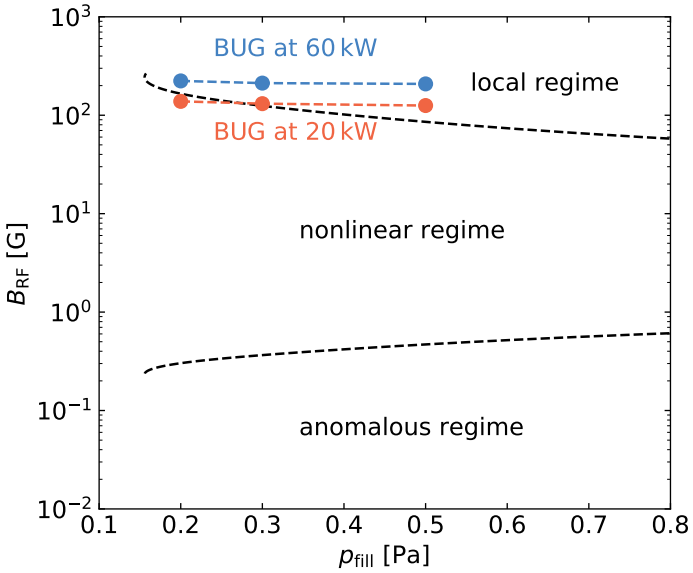

Figure 2.3: *RF skin effect regimes for various filling pressures p_{fill} at a fixed driving frequency $f_{\mathrm{RF}} = 1\,\mathrm{MHz}$. Electrical and plasma parameters ($n_{\mathrm{e}} \approx 10^{18}\,\mathrm{m}^{-3}$) from the BUG ion source driver are used to obtain the regime boundaries as well as the operation points at generator powers of 20 and 60 kW, respectively.*

At lower pressures and rather small magnetic RF fields there is the anomalous skin effect regime. In this regime, collisionless heating predominates over collisional heating [51]. Here the electrons resonantly interact with the RF electric field in the anomalous RF sheath and thereby absorb power [52, 53]. For magnetic fields larger than 0.3 G discharges are in the nonlinear skin effect regime. In this regime the nonlinear RF Lorentz force caused by the RF magnetic field becomes comparable to the electric RF force and thus starts to affect the movement of the electrons [50, 54]. At higher magnetic RF fields (for 0.3 Pa at roughly 100 G) the Larmor radius becomes considerably smaller than the RF skin depth, wherefore

there is a transition to the local regime. Using measured RF coil current amplitudes I_0 between 150 and 300 A to estimate $B_{\mathrm{RF}} \approx \mu_0 \frac{N}{l} I_0$ (with number of turns per length $\frac{N}{l} \approx \frac{6}{0.1\,\mathrm{m}} = 60\,\mathrm{m}^{-1}$) yields that typical discharges in the BUG driver are located in the 'high magnetic RF field region' of the local skin effect regime just above the nonlinear regime.

2.3.4 Modeling challenges and state-of-the-art models

Inductively driven negative hydrogen ion sources are operated under unusual conditions, resulting in several challenges when attempting to model these discharges [22]. One major point is the operation at a driving frequency of 1 MHz, which is more than one order of magnitude lower than the industry standard frequency of 13.56 MHz. It follows from Faraday's law of induction that to produce the same electric RF field strength at a lower frequency the magnetic RF field must be increased. For this reason the RF Lorentz force (associated with the RF magnetic field) becomes comparable or even larger than the electric RF field at 1 MHz. This introduces considerable nonlinearities, leading to the ponderomotive effect, where the plasma is compressed by the RF Lorentz force [55–58]. Another point is the transport of electrons and ions, which is heavily affected by the plasma potential. The plasma potential in turn is highly dependent of the plasma sheath that evolves in front of the discharge walls. Since the plasma species and the neutrals are strongly coupled via neutralization and recombination processes at the walls, the plasma potential has to be calculated from the space charge distribution and quasi-neutrality cannot be assumed a priori, as is commonly done in plasma fluid models [33, 37]. Also because of the strong coupling via wall processes the neutral atoms and molecules cannot be described as a uniform background but have to be modeled via particle, momentum and energy balances. This becomes especially important at high powers of up to 100 kW. Here the low neutral densities are even further decreased by electrons that ionize the neutrals. This phenomenon is called neutral depletion via ionization [36]. Adding to the complexity is that at the low pressure around 0.3 Pa nonlinear ion inertia is important. Furthermore, magnetostatic fields present in ion sources strongly magnetize the electrons. Another aspect are the numerous elastic

and inelastic processes that take place between charged particles and neutrals in a hydrogen plasma [31].

All the above points directly or indirectly affect the RF power coupling, wherefore it is mandatory to consider them in a self-consistent model. Several authors devised RF power coupling models using basic simplified systems. Jain et al. [18, 19] used uniform electron plasma parameters as model inputs. The local skin effect regime was assumed, and collisionless heating taken into account by a stochastic collision frequency to calculate the skin depth. The plasma was coupled to the RF fields by means of a transformer model. However, a self-consistent description of transport processes and the RF Lorentz force are missing, wherefore this model cannot be used for design optimization studies. Lishev et al. [20, 21] solved transport equations for the spatial profiles of the charged particles and the electron energy. The local skin effect regime was assumed for the RF power coupling. However, the RF Lorentz force was neglected, wherefore nonlinear effects that impact on the RF power coupling are still missing. Hagelaar et al. [22, 23] spatially resolved the transport of the plasma species as well as the one of the neutrals. However, in the description of the RF power coupling the RF Lorentz force was apparently not retained in all components of the electron momentum balance. Collisionless heating was included by means of an effective viscosity formulation, assuming an anomalous skin effect regime [51]. However, at a driving frequency of 1 MHz no steady state solution was achieved, wherefore results were published for an applied frequency of 10 MHz.

3 Simulation model

3.1 Selecting a modeling approach

A plasma is an ionized gas, wherefore common plasma modeling approaches are based on the kinetic gas theory. Here the microscopic dynamics of a thermodynamic system that is not in a state of equilibrium is described by the Boltzmann kinetic equation (3.1). Depending on the level of approximation of the kinetic equation,

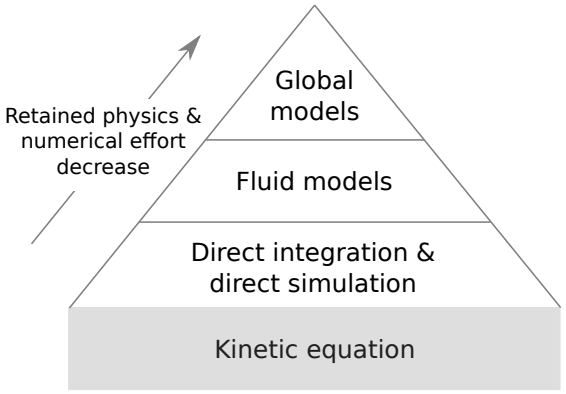

Figure 3.1: *Plasma models hierarchy, where all models involve different approximations of the Boltzmann kinetic equation* (3.1)*. The direct methods take the microscopic particle perspective, whereas the fluid models take the macroscopic continuum perspective. Global models are even further simplified fluid models. The retained physics as well as the numerical effort decrease from bottom to top.*

plasma models can be classified in a hierarchy as shown in figure 3.1: on the microscopic level the kinetic equation can be solved either by direct integration [59] or direct simulation methods [60]. However, on the macroscopic continuum level, fluid or even more simplified global models are used to describe the dynamics of the system. Depending on the type of plasma and the physics aspects of interest, a

modeling choice has to be made. Hereby the computational power at hand is an important restriction.

Starting on the microscopic level, the time evolution of a distribution function $f_\alpha(\boldsymbol{r}, \boldsymbol{v}, t)$ in phase space ($\boldsymbol{r}$,$\boldsymbol{v}$) is described by the *kinetic equation* (cf. [61])

$$\partial_t f_\alpha + \boldsymbol{v} \cdot \nabla_{\boldsymbol{r}} f_\alpha + \frac{\boldsymbol{F}_\alpha}{m_\alpha} \cdot \nabla_{\boldsymbol{v}} f_\alpha = \mathcal{C}_\alpha. \tag{3.1}$$

In a plasma there are three different types of particle species: ions, electrons and neutrals, i.e. $\alpha \in \{\mathrm{i}, \mathrm{e}, \mathrm{n}\}$ with masses m_α. Because the ions and electrons carry charges q_a, they are subject to the forces arising from electric and magnetic fields

$$\boldsymbol{F}_\alpha = q_\alpha(\boldsymbol{E} + \boldsymbol{v} \times \boldsymbol{B}). \tag{3.2}$$

The integral operator $\mathcal{C}_\alpha$ on the right hand side of the kinetic equation gives the change per unit time of f_α due to collisions with other species. Even in its simplest approximation of a binary collision, its concrete form is very complex, and it depends e.g. on whether the collision is elastic or inelastic [59, 61]. To obtain a self-consistent solution set $\{f_\mathrm{i}, f_\mathrm{e}, f_\mathrm{n}, \boldsymbol{E}, \boldsymbol{B}\}$, a set of kinetic equations for each species coupled to Maxwell's equations has to be solved. This problem can be tackled in various ways.

The most straight forward approaches are *direct integration* [59] and *direct simulation* [60]. Solutions obtained with these methods fully retain features associated with non-equilibrium thermodynamics, such as e.g. different species being not in thermodynamic equilibrium or even no thermodynamic equilibrium within one species. However, both methods suffer from severe numerical performance issues. The direct integration method is numerically very expensive since $f_\alpha(\boldsymbol{r}, \boldsymbol{v}, t)$ depends on seven independent dimensions (one for the time t and three each for the position $\boldsymbol{r}$ and for the velocity $\boldsymbol{v}$). The numerical effort can be estimated by assuming 100 uniformly distributed elements in each dimension. This yields $100^7 = 10^{14}$ calculations that have to be performed, which is only possible in a reasonable amount of time when highly parallelized super computers are used [62]. The direct simulation method reduces the numerical effort by following a set of computational particles in real space, which is divided up into cells, wherefore this method is also

called particle-in-cell (PIC) method. Here collisions are accounted for by means of a stochastic Monte Carlo method (MCC) [63]. In the PIC-MCC method an approximation of f_α is obtained from the discrete particles velocities in a specific cell. However, for the PIC-MCC method to produce stable and accurate solutions (e.g. statistical noise and numerical heating are common issues [62]), fundamental length- and time-scales such as the Debye length, as given by equation (2.17), and the plasma frequency, as given by equation (2.29), restrict the discretization in typical low pressure low temperature hydrogen plasmas to cell sizes and time steps in the order of $10^{-5}\,\mathrm{m}$ and $10^{-9}\,\mathrm{s}$, respectively. Hence the direct simulation of the BUG ion source with its large volume of around $40\,\ell$ and its high plasma particle densities of around $10^{18}\,\mathrm{m}^{-3}$ is not feasible on a common workstation but rather a task for a highly parallelized super computer that would run for months to obtain a steady state solution [64–66].

Located at the top of the model hierarchy in figure 3.1 are zero dimensional *global models* [67, 68]. They perform very well numerically, because no spatial and no velocity dimensions are considered. The resulting system of ordinary differential equations, where the time t is the only remaining dimension, is solved for the particle number densities and energies. However, by neglecting the space dimensions, the interaction of the particles with the electric and magnetic fields cannot be resolved, wherefore global models cannot be used to study the RF power coupling.

As shown in figure 3.1, there is a third approach situated in between these two extremes: the *fluid models*. Here, transport equations for the spatially resolved macroscopic quantities particle number density, momentum and energy are derived from the kinetic equation. Because the transport equations are resolved in space and time they can be coupled to Maxwell's equations. In this way the electric and magnetic fields can be solved self-consistently along with the macroscopic plasma quantities, which makes the fluid model a viable tool for studying the RF power coupling. Since the macroscopic quantities do not depend on any of the three velocity dimensions, fluid models are numerically not as demanding as the kinetic methods. Owing to the macroscopic character of the equations, restrictions for spatial and time discretization are more relaxed compared to the kinetic methods, i.e. cell sizes as large as 1 cm are possible and implicit time stepping methods are in principle only restricted by the numerical error. The advantages of the fluid model

are its numerical efficiency as well as that it is easy and intuitive to interpret the resulting macroscopic quantities. However, one inherent drawback is the assumption of a distribution function that is close to a Maxwellian one. This becomes relevant at low pressures, where as a consequence of the infrequent collisions the distribution functions of the individual particle species can deviate from a Maxwellian one. When quantitatively comparing results from a fluid model to values obtained from the experiment, the question has to be asked, whether kinetic effects (resulting from a distribution function that is *not* close to a Maxwellian) are responsible for the deviation. The answer to this question can either be provided by a direct measurement of the distribution function, as performed for the electrons in [69] or a direct simulation of the distribution function, as done for the neutrals in [35].

3.2 Simulation domain

The spatial dimensions of the BUG ion source are shown in figure 2.1, where driver and expansion chamber occupy a volume of $7\,\ell$ and $33\,\ell$, respectively. Because of these large volumes a super computer rather than a workstation would be necessary when a 3D simulation domain is used. To avoid this, cylindrical symmetry is assumed yielding the 2D simulation domain shown in figure 3.2. The driver in the experimental setup is cylindrically shaped, wherefore the axial length $L_{\mathrm{driver}} = 17.4\,\mathrm{cm}$ and radius $R_{\mathrm{driver}} = 11.85\,\mathrm{cm}$ are directly used in the simulation domain. The expansion chamber in the experimental setup is a cuboid with an axial length of 24.35 cm, which is also directly used in the simulation domain. The height of 54.6 cm and width of 31.1 cm are approximated by $R_{\mathrm{expansion}} = 18.8\,\mathrm{cm}$. This is chosen such that the cylindrical expansion volume in the simulation domain has the same volume to surface ratio as in the experiment, since the plasma parameters are sensitive to this ratio [23].

An RF coil with six turns is positioned axially central between the driver- and source-backplate (BP). It is formed from a hollow (for the water cooling) copper tube with an outer diameter of 6 mm. The radius of the RF coil is $R_{\mathrm{coil}} = 13.6\,\mathrm{cm}$ and from the constant coil pitch follows a distance of 1.2 cm between the coil windings. Owing to the cylindrically symmetric simulation domain the RF coil is realized as six individual windings. Because of the well pronounced skin effect at

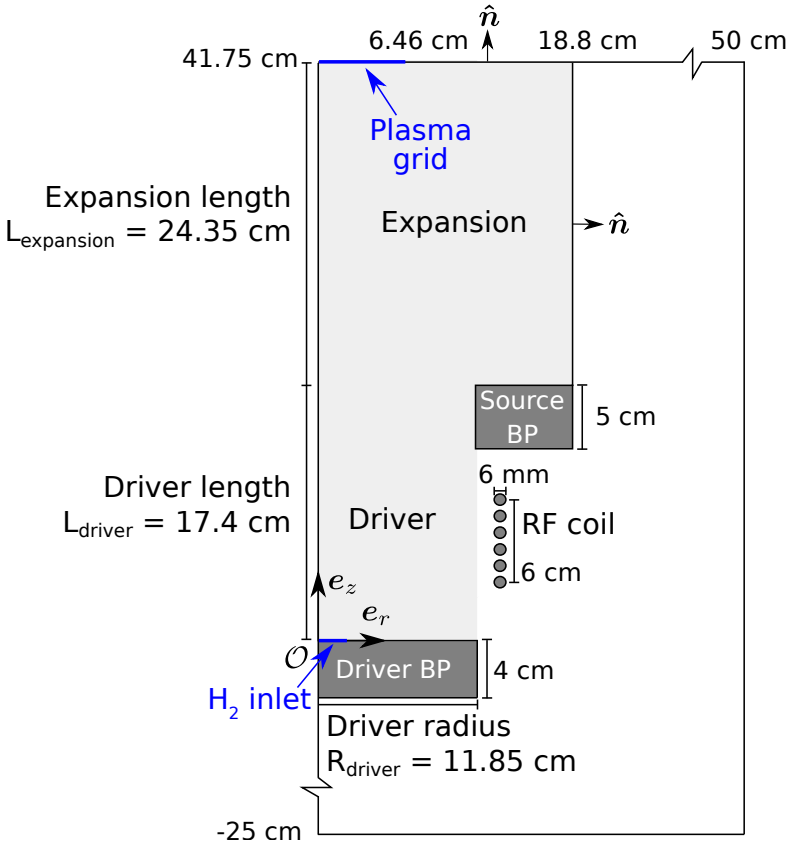

Figure 3.2: *Cylindrically symmetric (i.e. $\partial_\varphi = 0$) simulation domain of the BUG ion source. The driver- and source-backplates as well as the inside of the RF coil windings (shaded in dark grey) are excluded from the simulation domain.*

1 MHz, the coil windings in the simulation domain are treated as surfaces (circles), whose volume is excluded from the simulation domain. For the same reason the conducting driver and source back plates are excluded from the simulation domain. The internal Faraday screen is not cylindrically symmetric because of the axial slits at discrete positions on its circumference, as shown in figure 2.1. For this reason it is also not included in the simulation domain. The losses in the network components RF coil, Faraday screen and back plates are quantified by the network resistance, as explained in section 2.3.1.

3.3 Fluid approach

3.3.1 Transport equations

Instead of solving for the distribution function f_α itself, the fluid approach considers spatially resolved macroscopic quantities such as the particle number density n_α, the mean velocity $\boldsymbol{u}_\alpha$ and the temperature T_α. These quantities are obtained as velocity moments of increasing order of $f_\alpha(\boldsymbol{r},\boldsymbol{v},t)$ (cf. [34, 61, 70]):

$$n_\alpha(\boldsymbol{r},t) = \int f_\alpha \,\mathrm{d}^3\boldsymbol{v} \tag{3.3a}$$

$$\boldsymbol{u}_\alpha(\boldsymbol{r},t) = \frac{1}{n_\alpha}\int \boldsymbol{v} f_\alpha \,\mathrm{d}^3\boldsymbol{v} \tag{3.3b}$$

$$k_\mathrm{B}T_\alpha(\boldsymbol{r},t) = \frac{1}{n_\alpha}\int \frac{m_\alpha}{3}(\boldsymbol{v}-\boldsymbol{u}_\alpha)^2 f_\alpha \,\mathrm{d}^3\boldsymbol{v} \tag{3.3c}$$

Integrating the kinetic equation (3.1) over velocity space yields the *particle transport equation* for n_α:

$$\partial_t n_\alpha + \nabla\cdot(n_\alpha \boldsymbol{u}_\alpha) = \mathcal{R}_\alpha, \tag{3.4}$$

where $\mathcal{R}_\alpha$ is the number of particles created respectively destroyed by inelastic collisions per unit volume and unit time. The *momentum transport equation* is obtained by multiplying the kinetic equation with $m_\alpha\boldsymbol{v}$ and integrating over velocity space. Here, the dependent variable is the average velocity $\boldsymbol{u}_\alpha$:

$$m_\alpha n_\alpha \frac{\mathrm{D}\boldsymbol{u}_\alpha}{\mathrm{D}t} = -\nabla p_\alpha - \nabla\cdot\underline{\underline{\boldsymbol{\pi}}}_\alpha + n_\alpha q_\alpha(\boldsymbol{E}+\boldsymbol{u}_\alpha\times\boldsymbol{B}) + \boldsymbol{\mathcal{F}}_\alpha - m_\alpha\mathcal{S}_\alpha\boldsymbol{u}_\alpha. \tag{3.5}$$

$\frac{\mathrm{D}}{\mathrm{D}t} = \partial_t + \boldsymbol{u}_\alpha\cdot\nabla$ is the material derivative. Its convective part $\boldsymbol{u}_\alpha\cdot\nabla$ describes the transport of a macroscopic quantity in the flow field $\boldsymbol{u}_\alpha$. On the right hand side of the momentum transport equation are the forces that change the momentum such as the pressure gradient force $-\nabla p_\alpha$ that pushes the fluid elements in the direction of decreasing pressure. The force that results from the anisotropic part of the pressure tensor (= stress tensor $(\underline{\underline{\boldsymbol{\pi}}}_\alpha)_{i,j}$) is calculated as the tensor divergence $\nabla\cdot\underline{\underline{\boldsymbol{\pi}}} = \partial_{x_j}\pi_{ji}\boldsymbol{e}_i$, where the Einstein sum convention is applied. When a particle species carries charge q_α, it is subject to forces due to electric and magnetic fields,

as given by $q_\alpha(\boldsymbol{E} + \boldsymbol{u}_\alpha \times \boldsymbol{B})$. Momentum gains or losses in elastic collisions are denoted by $\boldsymbol{\mathcal{F}}_\alpha$. Also the momentum loss due to inelastic collisions plays a role via the term $-m_\alpha \mathcal{S}_\alpha \boldsymbol{u}_\alpha$. It follows from reinsertion of the particle transport equation in the derivation of the convective form of the momentum transport equation. Only newly created particles contribute to this momentum loss, wherefore $\mathcal{S}_\alpha$ comprises only the positive contributions of $\mathcal{R}_\alpha$.

The *energy transport equation* is obtained by multiplying the kinetic equation with $\frac{m_\alpha}{2}\boldsymbol{v}^2$ and integrating over velocity space. Here, the dependent variable is the temperature T_α:

$$\partial_t(n_\alpha \frac{m_\alpha}{2}\boldsymbol{u}_\alpha^2 + n_\alpha \frac{3+\zeta_{\alpha,\mathrm{int}}}{2} k_\mathrm{B} T_\alpha) + \nabla \cdot \boldsymbol{Q}_\alpha = q_\alpha n_\alpha \boldsymbol{u}_\alpha \cdot \boldsymbol{E} + \mathcal{P}_\alpha. \tag{3.6}$$

Energy gains and losses via collisional processes are denoted by $\mathcal{P}_\alpha$. The energy flux density

$$\boldsymbol{Q}_\alpha = (\frac{m_\alpha}{2}\boldsymbol{u}_\alpha^2 + \frac{3+\zeta_{\alpha,\mathrm{int}}}{2} k_\mathrm{B} T_\alpha) n_\alpha \boldsymbol{u}_\alpha + p_\alpha \boldsymbol{u}_\alpha + \underline{\underline{\boldsymbol{\pi}}}_\alpha \boldsymbol{u}_\alpha + \boldsymbol{q}_\alpha \tag{3.7}$$

consists of transported kinetic and thermal energy, the work of the (an-)isotropic pressure forces and the heat flux density $\boldsymbol{q}_\alpha$ that is associated exclusively with the random particle motion. Equations (3.6) and (3.7) explicitly account for the internal degrees of freedom $\zeta_{\alpha,\mathrm{int}} = \zeta_{\alpha,\mathrm{vib}} + \zeta_{\alpha,\mathrm{rot}}$ where equipartition of the translational, vibrational (ζ_vib) and rotational (ζ_rot) energy modes is assumed.

The particle, momentum and energy transport equations (3.4), (3.5) and (3.6) are coupled, i.e. every lower order equation depends on a higher order moment: the particle transport equation depends on $\boldsymbol{u}_\alpha$, the momentum transport equation on T_α (expressed as $p_\alpha = n_\alpha k_\mathrm{B} T_\alpha$) and the energy transport equation on the stress tensor $\underline{\underline{\boldsymbol{\pi}}}_\alpha$ and on the heat flux density $\boldsymbol{q}_\alpha$. Since the system is truncated at this level, $\underline{\underline{\boldsymbol{\pi}}}_\alpha$ and $\boldsymbol{q}_\alpha$ have to be expressed as functions of the lower order moments $n_\alpha, \boldsymbol{u}_\alpha$ and T_α. This is done using the Chapman-Enskog asymptotic scheme [71]. Here, the distribution function f_α is written as an equilibrium Maxwellian $f_{\alpha,0}$ and an unknown non-Maxwellian disturbance $f_{\alpha,1}$, i.e.

$$f_\alpha(\boldsymbol{r}, \boldsymbol{v}, t) = f_{\alpha,0}(\boldsymbol{r}, \boldsymbol{v}, t) + \epsilon f_{\alpha,1}(\boldsymbol{r}, \boldsymbol{v}, t). \tag{3.8}$$

The small expansion parameter $\epsilon = \lambda_{\mathrm{mfp}}/L \ll 1$ depends on the mean free path λ_{mfp} and the length scale of variation L. The kinetic equation is then linearized and $f_{\alpha,1}$ is expanded in velocity space yielding an infinite set of algebraic equations with unknown coefficients. By keeping only the first two terms of this expansion, the now finite system can be solved and thus $f_{\alpha,1}$ can be expressed as a function of $f_{\alpha,0}$ and the expansion coefficients.

$$\underline{\underline{\boldsymbol{\pi}}}_{\alpha} = -m_\alpha n_\alpha \eta_\alpha \left(\nabla \boldsymbol{u}_\alpha + (\nabla \boldsymbol{u}_\alpha)^\top - \frac{2}{3}(\nabla \cdot \boldsymbol{u}_\alpha)\underline{\underline{I}} \right) \tag{3.9}$$

and

$$\boldsymbol{q}_\alpha = -\kappa_\alpha \nabla k_{\mathrm{B}} T_\alpha \tag{3.10}$$

can then be found by evaluating the corresponding moments using $f_{\alpha,1}$. In the expression for the stress tensor, η_α denotes the kinematic viscosity and the dyadic $\nabla \boldsymbol{u}_\alpha = (\partial_{x_i} u_j)_{i,j}$. In the expression for the heat flux density κ_α denotes the thermal conductivity coefficient. Note that the direction of heat flow is opposite to the temperature gradient. For uniform density n_α and kinematic viscosity η_α it is possible to simplify $\nabla \cdot \underline{\underline{\boldsymbol{\pi}}}_{\alpha}$ in equation (3.5) to

$$\nabla \cdot \underline{\underline{\boldsymbol{\pi}}}_{\alpha} = -m_\alpha n_\alpha \eta_\alpha (\nabla^2 \boldsymbol{u}_\alpha + \frac{1}{3}\nabla(\nabla \cdot \boldsymbol{u}_\alpha)) \tag{3.11}$$

by using the identities $\nabla \cdot \nabla \boldsymbol{u}_\alpha = \nabla^2 \boldsymbol{u}_\alpha$ and $\nabla \cdot (\nabla \boldsymbol{u}_\alpha)^\top = \nabla(\nabla \cdot \boldsymbol{u}_\alpha)$.

Also the collision terms $\mathcal{R}_\alpha, \boldsymbol{\mathcal{F}}_\alpha$ and $\mathcal{P}_\alpha$ have to be expressed in terms of the lower order moments to make the system complete. Deriving the expressions for the stress tensor, the heat flux and for the collision terms is called closure problem in the literature. As indicated above, during this process it is assumed that the distribution function is close to a Maxwellian distribution function. To make the system well-posed, the transport equations and Maxwell's equations have to be supplied with boundary conditions. For the transport equations, this again involves the assumption of a specific type of velocity distribution function. This is discussed in detail in section 3.3.3.

3.3.2 Collisional processes

Multi-body collisions are negligible in low temperature plasmas [33, 39], wherefore only binary collisions between species α and β have to be considered. In this case the reaction rate per unit volume for a specific process l is defined as

$$\mathcal{R}_l = \iint \sigma_l(v) v f_\alpha(\boldsymbol{v}_\alpha) f_\beta(\boldsymbol{v}_\beta)\, \mathrm{d}^3\boldsymbol{v}_\alpha \mathrm{d}^3\boldsymbol{v}_\beta, \tag{3.12}$$

where the collision cross section $\sigma_l(v)$ depends on the relative speed $v = |\boldsymbol{v}_\alpha - \boldsymbol{v}_\beta|$. When f_α and f_β are both Maxwellian as defined in equation (2.1), than it is possible to obtain an analytic expression for equation (3.12) when transformed from the laboratory into the center-of-mass system [70]. Changing to energy space after the transformation by means of $\epsilon = \frac{\mu_{\alpha,\beta}}{2} v^2$ results in

$$\begin{aligned} \mathcal{R}_l &= n_\alpha n_\beta \int_0^\infty \sigma_l(\epsilon) \left(\frac{2\epsilon}{\mu_{\alpha,\beta}}\right)^{1/2} \frac{2}{\pi^{1/2}\epsilon_{\alpha,\beta}^{3/2}} \epsilon^{1/2} \exp\left(-\frac{\epsilon}{\epsilon_{\alpha,\beta}}\right) \mathrm{d}\epsilon \\ &=: n_\alpha n_\beta X_l(\mu_{\alpha,\beta}, \epsilon_{\alpha,\beta}) \end{aligned} \tag{3.13}$$

The rate coefficient X_l is thus a convenient expression to quantify the reaction rate. It depends on the reduced mass

$$\mu_{\alpha,\beta} = \frac{m_\alpha m_\beta}{m_\alpha + m_\beta} \tag{3.14}$$

and on the energy

$$\epsilon_{\alpha,\beta} = \frac{m_\alpha k_\mathrm{B} T_\beta + m_\beta k_\mathrm{B} T_\alpha}{m_\alpha + m_\beta}. \tag{3.15}$$

Foremost for the elastic processes between an impacting particle α on a particle β it is convenient to use the rate coefficient for this elastic collision $X_{\alpha,\beta}$ to define a collision frequency $\nu_{\alpha,\beta}$ as

$$\nu_{\alpha,\beta} = n_\beta X_{\alpha,\beta}. \tag{3.16}$$

In the special case of an electron impact collision a light electron $\alpha = \mathrm{e}$ strikes on a heavy particle β. Here $T_\mathrm{e} \gg T_\beta$ and $m_\mathrm{e} \ll m_\beta$, wherefore equations (3.14) and (3.15) simplify to $\mu_{\mathrm{e},\beta} \approx m_\mathrm{e}$ and $\epsilon_{\mathrm{e},\beta} \approx k_\mathrm{B} T_\mathrm{e}$. In this case the rate coefficient is to a good approximation a function of T_e, i.e. $X_l = X_l(T_\mathrm{e})$.

Table 3.1: *Inelastic collisional processes included in the model. Reactions that solely contribute as electron energy loss are marked by* †.

Partner	Process	Reaction equation	References
		Electron impact processes	
H	$3 \times$ electronic excitation†	$\mathrm{e} + \mathrm{H}(n=1) \rightarrow \mathrm{e} + \mathrm{H}(n=2,3,4)$	[31]
	Ionization	$\mathrm{e} + \mathrm{H}(n=1) \rightarrow 2\mathrm{e} + \mathrm{H}^+$	[31]
H_2	Non-dissociative ionization	$\mathrm{e} + \mathrm{H_2} \rightarrow 2\mathrm{e} + \mathrm{H_2^+}$	[31]
	$2 \times$ dissociative ionization	$\mathrm{e} + \mathrm{H_2} \overset{X\,^2\Sigma_g^+}{\underset{B\,^2\Sigma_u^+}{\rightarrow}} 2\mathrm{e} + \mathrm{H}^+ + \mathrm{H}$	[31]
	$10 \times$ singlet state excitation† B, B' & $B''\,^1\Sigma_u$; C, D & $D'\,^1\Pi_u$, $EF, H\bar{H}$ & $GK\,^1\Sigma_g^+$; $I\,^1\Pi_g$	$\mathrm{e} + \mathrm{H_2} \rightarrow \mathrm{e} + \mathrm{H_2^*}$	[31]
	$4 \times$ triplet state excitation† $a\,^3\Sigma_g^+$; $e\,^3\Sigma_u^+$; c & $d\,^3\Pi_u$	$\mathrm{e} + \mathrm{H_2} \rightarrow \mathrm{e} + \mathrm{H_2^*}$	[31]
	Dissociation	$\mathrm{e} + \mathrm{H_2} \rightarrow \mathrm{e} + 2\mathrm{H}$	[72, 73]
	$2 \times$ vibrational excitation†	$\mathrm{e} + \mathrm{H_2}(v=0) \rightarrow \mathrm{e} + \mathrm{H_2}(v=1,2)$	[31]
H_2^+	Dissociative excitation	$\mathrm{e} + \mathrm{H_2^+} \rightarrow \mathrm{e} + \mathrm{H}^+ + \mathrm{H}$	[31]
	Dissociative recombination	$\mathrm{e} + \mathrm{H_2^+} \rightarrow 2\mathrm{H}$	[31]
H_3^+	Dissociative excitation	$\mathrm{e} + \mathrm{H_3^+} \rightarrow \mathrm{e} + \mathrm{H}^+ + \mathrm{H_2}$	[31]
	Dissociative recombination	$\mathrm{e} + \mathrm{H_3^+} \rightarrow \mathrm{H} + \mathrm{H_2}$	[31]
		$\mathrm{H_2^+}$ *impact process*	
H_2	H_3^+ formation	$\mathrm{H_2^+} + \mathrm{H_2} \rightarrow \mathrm{H_3^+} + \mathrm{H}$	[74]

A multitude of inelastic collisions between free electrons, positive and negative ion species, atoms and molecules take place in a low temperature hydrogen plasma. In molecules vibrational and rotational excitation occurs beyond electronic excitation.

Preceding works on inelastic collision processes in hydrogen at different discharge conditions were performed by several authors [23, 26, 31, 72, 74–82]. To keep the model numerically efficient, it is necessary to select from these works only those species and collisional processes that affect the discharge in the driver, where the RF power coupling takes place.

A self-consistent description of the surface and volume produced H^- is a very complex task [23, 26, 66, 78, 80, 81, 83–85]. However, it has been shown by global chemical kinetics modeling, that $n_{H^-} \ll n_e$ everywhere in the ion source (except in the direct vicinity of the plasma grid), because the destruction of H^- by electron detachment is very efficient for $T_e > 2\,\mathrm{eV}$ [80]. Hence it is reasonable to exclude surface as well as volume produced H^- from the model.

The cross-sections for different molecular processes such as dissociative electron attachment, dissociation and ionization are sensitive to the vibrational energy levels. However, for a large $T_e \approx 10\,\mathrm{eV}$, as encountered in the driver, the effective rate coefficients with and without considering a vibrational population do not differ substantially [86]. Hence, the individual vibrational energy levels in the hydrogen molecule are not resolved in the model.

The cesium density in the ion source calculated with transport codes [84] and measured with laser absorption spectroscopy technique [87] is globally low, i.e. $n_{Cs}, n_{Cs^+} \ll n_e$. For this reason cesium is also not included in the model.

In this way the simplified set of inelastic reactions shown in table 3.1 is obtained, where only electrons, three different positive ion species H^+, H_2^+, H_3^+ and the ground state atoms and molecules are modeled. The rates for all inelastic processes are calculated using equation (3.13).

The elastic collision processes included in the model are specified in table 3.2, with collision cross sections from the given references.

Table 3.2: *References for the elastic collision cross sections used in the model.*

	Impacting species					
	e	H^+	H_2^+	H_3^+	H	H_2
H	[88–90]	[91]	[92]	n/a	[91]	[91, 93]
H_2	[72]	[93]	[94]	[93]	[91, 93]	[42]

There is no reference available for the elastic collision cross section between H_3^+ and H, wherefore a value in the same order of the other elastic ion neutral rate coefficients is assumed. Since H_3^+ is the minority species in the driver, this assumption has almost no impact on the plasma parameters there.

3.3.3 Boundary conditions

The particle and energy transport equations (3.4) and (3.6) require boundary conditions. The *particle flux towards the discharge boundary* is

$$n_\alpha \boldsymbol{u}_\alpha \cdot \hat{\boldsymbol{n}} = n_\alpha u_{\alpha,\mathrm{eff}} - (1 - t_{\mathrm{grid}})\Gamma_{\alpha,\mathrm{back}} - \Gamma_{\alpha,\mathrm{inj}}. \tag{3.17}$$

Herein $\hat{\boldsymbol{n}}$ is the normal vector perpendicular to the boundary, as indicated in figure 3.2. This state-of-the-art formulation was developed by Hagelaar et al. [22], to account for surface processes such as reflection and recombination that considerably affect the spatial profiles of the neutrals and plasma parameters at low pressures. The boundary flux consists of three parts. The first part $n_\alpha u_{\alpha,\mathrm{eff}}$ is an effective forward flux, whereas the second part $\Gamma_{\alpha,\mathrm{back}}$ is a back flux. On the plasma grid boundary $\Gamma_{\alpha,\mathrm{back}}$ is reduced by a constant factor $(1 - t_{\mathrm{grid}})$. Here the *plasma grid transparency* $t_{\mathrm{grid}} \in [0,1]$ models the effect that there is no back flux at the grid holes without having to resolve the individual holes in space. The third part $\Gamma_{\alpha,\mathrm{inj}}$ (which is applied solely at the inlet boundary) is subtracted to account for an inwards pointing influx.

The effective forward flux $n_\alpha u_{\alpha,\mathrm{eff}}$ is calculated from kinetic theory, i.e.

$$n_\alpha u_{\alpha,\mathrm{eff}} = \int_{-\infty}^{\infty} \mathrm{d}v_x \int_{-\infty}^{\infty} \mathrm{d}v_y \int_{0}^{\infty} \mathrm{d}v_z v_z f_\alpha, \tag{3.18}$$

where without loss of generality the wall is assumed to be in the xy - plane. For a drifting Maxwell-Boltzmann distribution function

$$f_\alpha(\boldsymbol{r}, \boldsymbol{v}, t)\,\mathrm{d}^3\boldsymbol{v} = \frac{n_\alpha}{\pi^{3/2} v_{\alpha,\mathrm{p}}^3} \exp\left(-\frac{v_x^2 + v_y^2 + (v_z - u_{\alpha,\perp})^2}{v_{\alpha,\mathrm{p}}^2}\right) \mathrm{d}^3\boldsymbol{v} \tag{3.19}$$

with drift velocity $u_{\alpha,\perp}$ in positive z direction, the triple integral in equation (3.18) is solved analytically. This yields

$$n_\alpha u_{\alpha,\mathrm{eff}} = \frac{n_\alpha}{2\pi^{1/2}} \left(\pi^{1/2} u_{\alpha,\perp} (1 + \mathrm{erf}\left(\frac{u_{\alpha,\perp}}{v_{\alpha,\mathrm{p}}} \right)) + v_{\alpha,\mathrm{p}} \exp\left(\frac{-u_{\alpha,\perp}^2}{v_{\alpha,\mathrm{p}}^2} \right) \right), \tag{3.20}$$

where erf denotes the Gauss error function. Without a drift, i.e. for $u_{\alpha,\perp} = 0$, equation (3.20) simplifies to

$$n_\alpha u_{\alpha,\mathrm{eff}} = n_\alpha \frac{v_{\alpha,\mathrm{p}}}{2\pi^{1/2}}. \tag{3.21}$$

The back flux Γ_α is due to particle conversion of species $\beta \neq \alpha$ into species α and due to reflection for $\beta = \alpha$, i.e.

$$\Gamma_{\alpha,\mathrm{back}} = \sum_\beta \frac{A_\beta}{A_\alpha} p_{\beta,\alpha} n_\beta u_{\beta,\mathrm{eff}}. \tag{3.22}$$

Herein A_β denotes the mass number of species β and $p_{\beta,\alpha}$ the probability that an impinging particle of species $\beta \neq \alpha$ is converted into species α or reflected, if $\beta = \alpha$, respectively.

The *energy flux towards the boundary* is

$$\boldsymbol{Q}_\alpha \cdot \hat{\boldsymbol{n}} = n_\alpha u_{\alpha,\mathrm{eff}} U_\alpha - (1 - t_{\mathrm{grid}}) \Theta_{\alpha,\mathrm{back}} - \Theta_{\alpha,\mathrm{inj}}. \tag{3.23}$$

It is defined similar as the particle boundary flux in equation (3.17). For a drifting Maxwellian, the effective forward energy flux $n_\alpha u_{\alpha,\mathrm{eff}} U_\alpha$ for a fluid with translational and internal energy is obtained from kinetic theory as

$$\begin{aligned} n_\alpha u_{\alpha,\mathrm{eff}} U_\alpha &= \int_{-\infty}^{\infty} \mathrm{d}v_x \int_{-\infty}^{\infty} \mathrm{d}v_y \int_0^{\infty} \mathrm{d}v_z \left(\frac{m_\alpha}{2} v^2 + \frac{\zeta_{\alpha,\mathrm{int}}}{2} k_\mathrm{B} T_\alpha \right) v_z f_\alpha \\ &= \frac{n_\alpha m_\alpha}{8\pi^{1/2}} (\pi^{1/2} w_{\alpha,\perp} (3v_{\alpha,\mathrm{p}}^2 + 2w_{\alpha,\perp}^2)(1 + \mathrm{erf}\left(\frac{u_{\alpha,\perp}}{v_{\alpha,\mathrm{p}}} \right)) \\ &\quad + \frac{n_\alpha m_\alpha}{8\pi^{1/2}} (2v_{\alpha,\mathrm{p}} (v_{\alpha,\mathrm{p}}^2 + w_{\alpha,\perp}^2) \exp\left(\frac{-w_{\alpha,\perp}^2}{v_{\alpha,\mathrm{p}}^2} \right)) \\ &\quad + n_\alpha u_{\alpha,\mathrm{eff}} (1 + \frac{\zeta_{\alpha,\mathrm{int}}}{2}) k_\mathrm{B} T_\alpha \end{aligned} \tag{3.24}$$

Without a drift, i.e. for $u_{\alpha,\perp} = 0$, equation (3.24) simplifies to

$$n_\alpha u_{\alpha,\mathrm{eff}} U_\alpha = n_\alpha \frac{v_{\alpha,\mathrm{p}}}{2\pi^{1/2}} (2 + \frac{\zeta_{\alpha,\mathrm{int}}}{2}) k_\mathrm{B} T_\alpha. \tag{3.25}$$

The energy back flux $\Theta_{\alpha,\mathrm{back}}$ is again due to conversion of species $\beta \neq \alpha$ into species α or due to reflection of species β. The wall accommodation coefficient $\alpha_{\beta,\alpha} \in [0,1]$ specifies the energy of the back injected particle. It varies between the two extreme cases $\alpha_{\beta,\alpha} = 0$, where the converted or reflected particle is coming back from the wall with the total energy of the incident particle U_β, and $\alpha_{\beta,\alpha} = 1$, where its energy is fully accommodated to the wall energy, i.e.

$$\Theta_\alpha = \sum_\beta \frac{A_\beta}{A_\alpha} p_{\beta,\alpha} n_\beta u_{\beta,\mathrm{eff}} \left((1 - \alpha_{\beta,\alpha}) U_\beta + \alpha_{\beta,\alpha} (2 + \frac{\zeta_{\alpha,\mathrm{int}}}{2}) k_\mathrm{B} T_\mathrm{wall} \right). \tag{3.26}$$

The expressions for the effective forward particle and energy boundary fluxes according to equation (3.20) and (3.24), respectively are calculated without any further simplifications, i.e. they are valid even if the drift velocity is not small compared to the thermal velocity. This is not the case in other fluid models (see e.g. [22] and [35]), where a Taylor approximation is used in the derivation of the boundary fluxes.

3.4 Neutrals module

3.4.1 Transport equations

Particle transport equation

The *particle transport equations* for the neutral atoms and molecules $\mathrm{n} \in \{\mathrm{a}, \mathrm{m}\}$ follow from equation (3.4). The particle number densities n_n are thus calculated using

$$\partial_t n_\mathrm{n} + \nabla \cdot (n_\mathrm{n} \boldsymbol{u}_\mathrm{n}) = \mathcal{R}_\mathrm{n}. \tag{3.27}$$

The reaction rates $\mathcal{R}_\mathrm{n}$ follow from the processes as specified in table 3.1, where equation (3.13) is used to calculate the reaction rate for each process.

Momentum transport equation

The *momentum transport equation* solved for the average fluid velocities $\boldsymbol{u}_\mathrm{n}$ is obtained from equation (3.5) as

$$m_\mathrm{n} n_\mathrm{n} \left(\partial_t \boldsymbol{u}_\mathrm{n} + (\boldsymbol{u}_\mathrm{n} \cdot \nabla)\boldsymbol{u}_\mathrm{n}\right) = -\nabla p_\mathrm{n} + m_\mathrm{n} n_\mathrm{n} \eta_\mathrm{n} \left(\nabla^2 \boldsymbol{u}_\mathrm{n} + \frac{1}{3}\nabla(\nabla \cdot \boldsymbol{u}_\mathrm{n})\right) + \boldsymbol{\mathcal{F}}_\mathrm{n}. \tag{3.28}$$

Herein the drag due to newly created neutrals in inelastic collisions is omitted, because $|m_\mathrm{n}\mathcal{S}_\mathrm{n}\boldsymbol{u}_\mathrm{n}| \ll |\boldsymbol{\mathcal{F}}_\mathrm{n}|$. The divergence of the stress tensor is simplified according to equation (3.11). The kinematic viscosity is calculated as [22]

$$\eta_\mathrm{n} = \mathrm{Sc}\frac{k_\mathrm{B} T_\mathrm{n}}{\sum_\mathrm{j} \mu_{\mathrm{n,j}} \nu_{\mathrm{n,j}}}, \tag{3.29}$$

where $\mathrm{Sc} \approx 0.7$ denotes the Schmidt number and j runs over all species including self collisions, i.e. j = n. The drag force per unit volume due to elastic collisions is

$$\boldsymbol{\mathcal{F}}_\mathrm{n} = -\sum_{\mathrm{j}\neq\mathrm{n}} \mu_{\mathrm{n,j}} n_\mathrm{n} \nu_{\mathrm{n,j}} (\boldsymbol{u}_\mathrm{n} - \boldsymbol{u}_\mathrm{j}). \tag{3.30}$$

The rate coefficients needed to calculate the collision frequencies $\nu_{\mathrm{n,j}} = X_{\mathrm{n,j}} n_\mathrm{j}$ are obtained using the cross sections from the references given in table 3.2.

Energy transport equation

The *energy transport equation* for the neutrals follows from equation (3.6), when the drift velocity is assumed small compared to the most probable speed, i.e. $|\boldsymbol{u}_n| \ll v_{\mathrm{n,p}}$:

$$\partial_t \left(n_\mathrm{n} \frac{3 + \zeta_{\mathrm{n,int}}}{2} \mathrm{k_B} T_\mathrm{n}\right) + \nabla \cdot \boldsymbol{Q}_\mathrm{n} = \mathcal{P}_\mathrm{n}. \tag{3.31}$$

For atoms only translation is relevant, wherefore $\zeta_{\mathrm{a,int}} = 0$. In molecular hydrogen $\zeta_{\mathrm{m,int}} = 3$, because two rotational and one vibrational modes are available for storing energy. The heat flux $\boldsymbol{Q}_{\mathrm{n}}$ is due to convection and conduction:

$$\boldsymbol{Q}_{\mathrm{n}} = \frac{3+\zeta_{\mathrm{n,int}}}{2} k_{\mathrm{B}} T_{\mathrm{n}} n_{\mathrm{n}} \boldsymbol{u}_{\mathrm{n}} + p_{\mathrm{n}} \boldsymbol{u}_{\mathrm{n}} - \kappa_{\mathrm{n}} \nabla k_{\mathrm{B}} T_{\mathrm{n}}, \tag{3.32}$$

where the thermal conductivity coefficient (measured in $\mathrm{m}^{-1}\mathrm{s}^{-1}$) is [22]

$$\kappa_{\mathrm{n}} = \mathrm{Le} \frac{\frac{5+\zeta_{\mathrm{n,int}}}{2} n_{\mathrm{n}} k_{\mathrm{B}} T_{\mathrm{n}}}{\sum_{\mathrm{j}} \mu_{\mathrm{n,j}} \nu_{\mathrm{n,j}}}. \tag{3.33}$$

The Lewis number is denoted by $\mathrm{Le} = \mathrm{Sc}/\mathrm{Pr} \approx 1$, where $\mathrm{Pr} \approx \frac{2}{3}$ is the Prandtl number. The neutrals gain or loose energy due to elastic collisions, directed energy transfer and inelastic collisions, i.e.

$$\mathcal{P}_{\mathrm{n}} = + \sum_{j \neq \mathrm{n}} \frac{3}{2} k_{\mathrm{j,n}} n_{\mathrm{n}} \nu_{\mathrm{n,j}} (k_{\mathrm{B}} T_{\mathrm{j}} - k_{\mathrm{B}} T_{\mathrm{n}}) \tag{3.34}$$

$$+ \sum_{j \neq \mathrm{n}} \frac{1}{2} k_{\mathrm{j,n}} n_{\mathrm{n}} \nu_{\mathrm{n,j}} \left(m_{\mathrm{j}} |\boldsymbol{u}_{\mathrm{j}}|^2 + (m_{\mathrm{n}} - m_{\mathrm{j}}) \boldsymbol{u}_{\mathrm{j}} \cdot \boldsymbol{u}_{\mathrm{n}} - m_{\mathrm{n}} |\boldsymbol{u}_{\mathrm{n}}|^2 \right) \tag{3.35}$$

$$+ \sum_{l_{\mathrm{n}}} \mathcal{R}_{l_{\mathrm{n}}} \Delta \epsilon_{l_{\mathrm{n}}}. \tag{3.36}$$

Herein, the coefficient of energy transfer $k_{\mathrm{j,n}} = \frac{2\mu_{\mathrm{j,n}}}{m_{\mathrm{j}} + m_{\mathrm{n}}}$ and l_{n} runs over all inelastic processes from table 3.1, where a particle of species n is created. Since there are no hydrogen molecules created in the volume, l_{m} is an empty set. Atoms however gain energy when created in the volume e.g. via dissociation of H_2, where with a threshold of energy of 7.4 eV it follows $\Delta\epsilon = 3.7\,\mathrm{eV}$ per atom created [73].

3.4.2 Boundary conditions

From equation (3.17) follow the *boundary fluxes for the neutral atoms and molecules* $\mathrm{n} \in \{\mathrm{a}, \mathrm{m}\}$ as

$$n_{\mathrm{n}} \boldsymbol{u}_{\mathrm{n}} \cdot \hat{\boldsymbol{n}} = n_{\mathrm{n}} u_{\mathrm{n,eff}} - (1 - t_{\mathrm{grid}}) \Gamma_{\mathrm{n,back}} - \Gamma_{\mathrm{n,inj}}. \tag{3.37}$$

Assuming that the neutrals drift towards the walls with a Maxwellian distribution function the effective forward flux is obtained from equation (3.20) as

$$n_{\mathrm{n}} u_{\mathrm{n,eff}} = \frac{n_{\mathrm{n}}}{2\pi^{1/2}} \left(\pi^{1/2} u_{\mathrm{n},\perp} (1 + \mathrm{erf} \left(\frac{u_{\mathrm{n},\perp}}{v_{\mathrm{n,p}}} \right)) + v_{\mathrm{n,p}} \exp \left(\frac{-u_{\mathrm{n},\perp}^2}{v_{\mathrm{n,p}}^2} \right) \right). \tag{3.38}$$

The back flux according to equation (3.22) is

$$\Gamma_{\mathrm{n,back}} = \sum_{\mathrm{j}} \frac{A_{\mathrm{j}}}{A_{\mathrm{n}}} p_{\mathrm{j,n}} n_{\mathrm{j}} u_{\mathrm{j,eff}}, \tag{3.39}$$

where j runs over all heavy particle species. The values for $p_{\mathrm{j,n}}$ are summarized in table 3.3. The molecules are the only species that are injected at the inlet boundary. For $\Gamma_{\mathrm{m,inj}}$ the experimentally measured flux is used, as explained in section 4.2.1. The *energy flux towards the boundary* is obtained from equation (3.23) as

$$\boldsymbol{Q}_{\mathrm{n}} \cdot \hat{\boldsymbol{n}} = n_{\mathrm{n}} u_{\mathrm{n,eff}} U_{\mathrm{n}} - (1 - t_{\mathrm{grid}}) \Theta_{\mathrm{n,back}} - \Theta_{\mathrm{n,inj}}. \tag{3.40}$$

The effective forward energy fluxes are obtained from equation (3.24) as

$$\begin{aligned} n_{\mathrm{n}} u_{\mathrm{n,eff}} U_{\mathrm{n}} = {} & \frac{n_{\mathrm{n}} m_{\mathrm{n}}}{8\pi^{1/2}} (\pi^{1/2} u_{\mathrm{n},\perp} (3 v_{\mathrm{n,p}}^2 + 2 u_{\mathrm{n},\perp}^2)(1 + \mathrm{erf} \left(\frac{u_{\mathrm{n},\perp}}{v_{\mathrm{n,p}}} \right)) \\ & + \frac{n_{\mathrm{n}} m_{\mathrm{n}}}{8\pi^{1/2}} (2 v_{\mathrm{n,p}} (v_{\mathrm{n,p}}^2 + u_{\mathrm{n},\perp}^2) \exp \left(\frac{-u_{\mathrm{n},\perp}^2}{v_{\mathrm{n,p}}^2} \right)) \\ & + n_{\mathrm{n}} u_{\mathrm{n,eff}} (1 + \frac{\zeta_{\mathrm{n,int}}}{2}) k_{\mathrm{B}} T_{\mathrm{n}}. \end{aligned} \tag{3.41}$$

Without a drift, i.e. for $u_{\mathrm{n},\perp} = 0$ follows

$$n_{\mathrm{n}} u_{\mathrm{n,eff}} U_{\mathrm{n}} = n_{\mathrm{n}} \frac{v_{\mathrm{n,p}}}{2\pi^{1/2}} (2 + \frac{\zeta_{\mathrm{n,int}}}{2}) k_{\mathrm{B}} T_{\mathrm{n}}. \tag{3.42}$$

The energy back flux Θ_{n} is obtained from equation (3.26)

$$\Theta_{\mathrm{n,back}} = \sum_{\mathrm{j}} \frac{A_{\mathrm{j}}}{A_{\mathrm{n}}} p_{\mathrm{j,n}} n_{\mathrm{j}} u_{\mathrm{j,eff}} \left((1 - \alpha_{\mathrm{j,n}}) U_{\mathrm{j}} + \alpha_{\mathrm{j,n}} (2 + \frac{\zeta_{\mathrm{n,int}}}{2}) k_{\mathrm{B}} T_{\mathrm{wall}} \right). \tag{3.43}$$

For hydrogen atoms $\zeta_{\mathrm{a,int}} = 0$ and for hydrogen molecules $\zeta_{\mathrm{m,int}} = 3$, accounting for one vibrational and two rotational modes. The wall accommodation coefficients are specified in table 3.3. For the inlet energy flux the expression

$$\Theta_{\mathrm{m,inj}} = \Gamma_{\mathrm{m,inj}}(2 + \frac{\zeta_{\mathrm{m,int}}}{2})k_{\mathrm{B}}T_{\mathrm{m,inj}} \tag{3.44}$$

is used, where room-temperature $T_{\mathrm{m,inj}} = 300\,\mathrm{K}$ is assumed for the molecules at the inlet.

Table 3.3: *Probability for wall recombination* $p_{\mathrm{j,n}}$ *of species* j *into either an atom* a *or molecule* m *and wall accommodation coefficient* $\alpha_{\mathrm{j,n}}$ *of species* j *coming back from the wall as atom or molecule, respectively. All values are taken from [23, 35], where molybdenum coated, i.e. conducting discharge walls are assumed.*

Species j towards wall	$p_{\mathrm{j,a}}$	$p_{\mathrm{j,m}}$	$\alpha_{\mathrm{j,a}}$	$\alpha_{\mathrm{j,m}}$
H^+	0.6	0.4	0.5	1
H_2^+	0.8	0.2	1	1
H_3^+	2/3	1/3	1	1
H	0.6	0.4	0.5	1
H_2	0	1	n/a	1

3.5 Plasma module

3.5.1 Electrostatic field

As explained in section 2.3.4 the plasma sheath is highly affected by the wall processes, wherefore a self-consistent description of the plasma potential is essential [22]. This excludes using the commonly applied quasi-neutrality assumption [37]. Instead ϕ_{plasma} has to be calculated from the *Poisson equation*

$$\nabla^2\phi_{\mathrm{plasma}} = -\frac{\mathrm{e}\,(\sum_{\mathrm{i}} n_{\mathrm{i}} - n_{\mathrm{e}})}{\epsilon_0}, \tag{3.45}$$

where ϵ_0 denotes the vacuum permittivity. The space charge density in the numerator of the right-hand side of equation (3.45) is due to the three positive ion

species $\mathrm{i} \in \{\mathrm{H}^+, \mathrm{H}_2^+, \mathrm{H}_3^+\}$ and the electrons. The electrostatic field calculated from the plasma potential as $\boldsymbol{E} = -\nabla\phi_{\mathrm{plasma}}$ is used in the ion momentum transport equations in section 3.5.2 and in the electron momentum and energy transport equations in section 3.5.4.

3.5.2 Ion transport equations

Particle transport equation

For each of the three positive hydrogen *ion species particle transport equations*

$$\partial_t n_\mathrm{i} + \nabla \cdot n_\mathrm{i}\boldsymbol{u}_\mathrm{i} = \mathcal{R}_\mathrm{i} \tag{3.46}$$

are solved for the particle number densities n_i. The reaction rates $\mathcal{R}_\mathrm{i}$ follow from the processes as specified in table 3.1, where equation (3.13) is used to calculate the reaction rate for each process.

Momentum transport equation

To obtain the average fluid velocities $\boldsymbol{u}_\mathrm{i}$, *momentum transport equations*

$$m_\mathrm{i} n_\mathrm{i} \left(\partial_t \boldsymbol{u}_\mathrm{i} + (\boldsymbol{u}_\mathrm{i} \cdot \nabla)\boldsymbol{u}_\mathrm{i}\right) = e n_\mathrm{i} \boldsymbol{E} - \nabla n_\mathrm{i} k_\mathrm{B} T_\mathrm{i} + \boldsymbol{\mathcal{F}}_\mathrm{i} - m_\mathrm{i} \mathcal{S}_\mathrm{i} \boldsymbol{u}_\mathrm{i} \tag{3.47}$$

are solved. As explained in section 2.2, the ions are not magnetized, wherefore the Lorentz force is neglected in equation (3.47). The distribution function of the ions is expected to be quite anisotropic because of the high electrostatic field in front of the walls. Nevertheless the force due to the divergence of the stress tensor is neglected in equation (3.47) because it is small compared to the electrostatic force and the convective $(\boldsymbol{u}_\mathrm{i} \cdot \nabla)\boldsymbol{u}_\mathrm{i}$ term that are dominant at low pressure [22]. The latter term considerably increases the nonlinearity of the ion momentum balances making their numerical treatment difficult. The force per unit volume acting on the ions due to elastic collisions between the ions and the neutrals is

$$\boldsymbol{\mathcal{F}}_\mathrm{i} = -\sum_\mathrm{n} \mu_{\mathrm{i,n}} n_\mathrm{i} \nu_{\mathrm{i,n}} (\boldsymbol{u}_\mathrm{i} - \boldsymbol{u}_\mathrm{n}). \tag{3.48}$$

The rate coefficients needed to calculate the collision frequencies $\nu_{\mathrm{i,n}} = n_{\mathrm{n}} X_{\mathrm{i,n}}$ are obtained using the cross sections from the references given in table 3.2. The drag resulting from newly created ions via inelastic collisions $-m_{\mathrm{i}} \mathcal{S}_{\mathrm{i}} \boldsymbol{u}_{\mathrm{i}}$ is important at low pressures, wherefore this term is retained in equation (3.47).

No energy transport equation is solved for the ions. Instead it is assumed that the H^+ ions are thermalized with the atoms, whereas the H_2^+ and H_3^+ ions are thermalized with the molecules, i.e. $T_{\mathrm{H}^+} = T_{\mathrm{a}}$ and $T_{\mathrm{H}_2^+} = T_{\mathrm{H}_3^+} = T_{\mathrm{m}}$ is used. The ion pressure plays only a minor role in the momentum transport equation, wherefore the values assumed for T_{i} hardly affect the plasma parameters at low pressures [22].

3.5.3 Electromagnetic fields

The electric and magnetic RF fields $\boldsymbol{E}_{\mathrm{RF}}$ and $\boldsymbol{B}_{\mathrm{RF}}$ are related by *Ampère-Maxwell's law* and *Faraday's law of induction*:

$$\nabla \times \boldsymbol{B}_{\mathrm{RF}} = \mu_0 \boldsymbol{J}_{\mathrm{RF}} + c_0^{-2} \partial_t \boldsymbol{E}_{\mathrm{RF}} \tag{3.49a}$$

$$\nabla \times \boldsymbol{E}_{\mathrm{RF}} = -\partial_t \boldsymbol{B}_{\mathrm{RF}}. \tag{3.49b}$$

Herein μ_0 and c_0 denote the permeability and the speed of light in vacuum, respectively. The RF current density in the plasma is denoted by $\boldsymbol{J}_{\mathrm{RF}}$. It is assumed that $\boldsymbol{X}_{\mathrm{RF}} \in \{\boldsymbol{E}_{\mathrm{RF}}, \boldsymbol{B}_{\mathrm{RF}}, \boldsymbol{J}_{\mathrm{RF}}\}$ oscillates harmonically at the angular frequency ω_{RF}. This approximation considerably reduces the calculation time of the model, since the RF time scale does not have to be resolved. The resulting time steps are as large as 0.1 s towards the end of the simulation compared to time steps that are restricted to 10^{-8} s when the time harmonic approximation is not applied. The disadvantage of this approximation is that effects such as e.g. generation of higher harmonics [56, 95] cannot be studied. However, a study retaining the full time dependency in Maxwell's equations at a fixed neutral particles background revealed, that the main nonlinear effects relevant for the power absorption such as e.g. the RF Lorentz force are still described reasonably accurate when the time

harmonic approximation is used. The harmonically oscillating quantities are thus written as

$$\boldsymbol{X}_{\mathrm{RF}}(\boldsymbol{r},t) = \mathrm{Re}\{\tilde{\boldsymbol{X}}_{\mathrm{RF}}(\boldsymbol{r})\exp(\mathrm{i}\omega_{\mathrm{RF}}t)\}, \tag{3.50}$$

where $\mathrm{Re}\{\cdot\}$ denotes the real part and the tilde indicates a complex quantity. Then, Maxwell's equations (3.49) can be rewritten as

$$\nabla \times \tilde{\boldsymbol{B}}_{\mathrm{RF}} = \mu_0 \tilde{\boldsymbol{J}}_{\mathrm{RF}} \tag{3.51a}$$

$$\nabla \times \tilde{\boldsymbol{E}}_{\mathrm{RF}} = -\mathrm{i}\omega \tilde{\boldsymbol{B}}_{\mathrm{RF}}. \tag{3.51b}$$

In the Ampère's law equation (3.51a), the displacement current density $\mathrm{i}\omega_{\mathrm{RF}} c_0^{-2} \tilde{\boldsymbol{E}}_{\mathrm{RF}}$ is neglected. How good this assumption is fulfilled can be estimated by comparing the local expression for $\tilde{\boldsymbol{J}}_{\mathrm{RF}}$ from equation (3.68) with the displacement current density. This yields

$$\mu_0 \mathrm{Im}\{\tilde{\sigma}_{\mathrm{plasma}}\} \gg \omega_{\mathrm{RF}} c_0^{-2} \Leftrightarrow \omega_{\mathrm{e,p}}^2 \gg \omega_{\mathrm{RF}}^2 + \nu_{\mathrm{e,n}}^2. \tag{3.52}$$

For discharges with $n_{\mathrm{e}} \gtrsim 10^{17}\,\mathrm{m}^{-3}$ the elecron plasma frequency $\omega_{\mathrm{e,p}}$ is well above 10 GHz, whereas the driving frequency ω_{RF} and the momentum transfer frequency $\nu_{\mathrm{e,n}}$ are in the MHz range. Thus inequality (3.52) is well fulfilled and the neglect of the displacement current density justified. Because of the assumed cylindrical symmetry it follows

$$\boldsymbol{B}_{\mathrm{RF}}(r,z,t) = \mathrm{Re}\{(\tilde{B}_{\mathrm{RF},r}(r,z)\boldsymbol{e}_r + \tilde{B}_{\mathrm{RF},z}(r,z)\boldsymbol{e}_z)\exp(\mathrm{i}\omega_{\mathrm{RF}}t)\} \tag{3.53a}$$

$$\boldsymbol{J}_{\mathrm{RF}}(r,z,t) = \mathrm{Re}\{\tilde{J}_{\mathrm{RF},\varphi}(r,z)\exp(\mathrm{i}\omega_{\mathrm{RF}})\}\boldsymbol{e}_\varphi \tag{3.53b}$$

$$\boldsymbol{E}_{\mathrm{RF}}(r,z,t) = \mathrm{Re}\{\tilde{E}_{\mathrm{RF},\varphi}(r,z)\exp(\mathrm{i}\omega_{\mathrm{RF}})\}\boldsymbol{e}_\varphi. \tag{3.53c}$$

Due to the large mass of the ions compared to the electrons only the electrons are heated directly by the RF electric field component. The RF current density in equation (3.53b) is thus calculated from the electron RF velocity

$$u_{\mathrm{e,RF},\varphi}(r,z,t) = \mathrm{Re}\{\tilde{u}_{\mathrm{e,RF},\varphi} \exp(\mathrm{i}\omega_{\mathrm{RF}})\} \tag{3.54}$$

as

$$\tilde{J}_{\mathrm{RF},\varphi} = -\mathrm{e}n_{\mathrm{e}}\tilde{u}_{\mathrm{e,RF},\varphi}. \tag{3.55}$$

The calculation of the electron RF velocity $\tilde{u}_{\mathrm{e,RF},\varphi}$ is detailed in equation (3.62) in the following section. Equation (3.53c) implies that capacitive coupling, i.e. electric RF field components in r and z direction, is not included in the model. This is a good approximation because of the presence of the Faraday screen and because of the high plasma densities $n_{\mathrm{e}} > 10^{18}\,\mathrm{m}^{-3}$ [39].

3.5.4 Electron transport equations

Electron particle transport equation

For the electrons the *particle transport equation*

$$\partial_t n_{\mathrm{e}} + \nabla \cdot n_{\mathrm{e}}\boldsymbol{u}_{\mathrm{e}} = \mathcal{R}_{\mathrm{e}} \tag{3.56}$$

is solved for their number density n_{e}. The reaction rate $\mathcal{R}_{\mathrm{e}}$ follows from the processes as specified in table 3.1, where equation (3.13) is used to calculate the reaction rate for each process.

Electron momentum transport equation

The *momentum transport equation* is obtained from equation (3.5) as

$$m_{\mathrm{e}}n_{\mathrm{e}}\frac{\mathrm{D}\boldsymbol{u}_{\mathrm{e}}}{\mathrm{D}t} = -\mathrm{e}n_{\mathrm{e}}(\boldsymbol{E} + \boldsymbol{u}_{\mathrm{e}} \times \boldsymbol{B}_{\mathrm{RF}}) - \nabla n_{\mathrm{e}}\mathrm{e}T_{\mathrm{e}} - \nabla \cdot \underline{\underline{\boldsymbol{\pi}}}_{\mathrm{e}} + \boldsymbol{\mathcal{F}}_{\mathrm{e}}. \tag{3.57}$$

The force per unit volume due to elastic momentum transfer collisions is [70]

$$\boldsymbol{\mathcal{F}}_\mathrm{e} = -\sum_\mathrm{n} \mu_\mathrm{e,n} n_\mathrm{e} \nu_\mathrm{e,n} (\boldsymbol{u}_\mathrm{e} - \boldsymbol{u}_\mathrm{n}) \approx -\sum_\mathrm{n} m_\mathrm{e} n_\mathrm{e} \nu_\mathrm{e,n} \boldsymbol{u}_\mathrm{e}. \tag{3.58}$$

For electrons $|m_\mathrm{e}\mathcal{S}_\mathrm{e}\boldsymbol{u}_\mathrm{e}| \ll |\boldsymbol{\mathcal{F}}_\mathrm{e}|$ wherefore the former term is omitted in equation (3.57). The momentum transport equation is a vector equation and thus has r, φ and z components in cylindrical symmetry. The RF Lorentz force in equation (3.57) is calculated as

$$\begin{aligned}
\boldsymbol{F}_\mathrm{L} &= -\mathrm{e}\boldsymbol{u_e} \times \boldsymbol{B}_\mathrm{RF} \\
&= -\mathrm{e}(u_{\mathrm{e},r}\boldsymbol{e}_r + u_{\mathrm{e,RF},\varphi}\boldsymbol{e}_\varphi + u_{\mathrm{e},z}\boldsymbol{e}_z) \times (B_{\mathrm{RF},r}\boldsymbol{e}_r + B_{\mathrm{RF},z}\boldsymbol{e}_z) \\
&= -\mathrm{e}u_{\mathrm{e,RF},\varphi}B_{\mathrm{RF},z}\boldsymbol{e}_r - \mathrm{e}(u_{\mathrm{e},z}B_{\mathrm{RF},r} - u_{\mathrm{e},r}B_{\mathrm{RF},z})\boldsymbol{e}_\varphi + \mathrm{e}u_{\mathrm{e,RF},\varphi}B_{\mathrm{RF},r}\boldsymbol{e}_z.
\end{aligned} \tag{3.59}$$

The RF-averaged Lorentz force $\bar{\boldsymbol{F}}_\mathrm{L}$ is calculated from equation (3.59) as [48]

$$\begin{aligned}
\bar{\boldsymbol{F}}_\mathrm{L} &= -\mathrm{e}\frac{\omega_\mathrm{RF}}{2\pi}\int_0^{2\pi/\omega_\mathrm{RF}} \boldsymbol{u}_\mathrm{e} \times \boldsymbol{B}_\mathrm{RF}\,\mathrm{d}t \\
&= -\mathrm{e}\frac{1}{2}\mathrm{Re}\{\tilde{u}_{\mathrm{e,RF},\varphi}\tilde{B}^*_{\mathrm{RF},z}\boldsymbol{e}_r - \tilde{u}_{\mathrm{e,RF},\varphi}\tilde{B}^*_{\mathrm{RF},r}\boldsymbol{e}_z\},
\end{aligned} \tag{3.60}$$

where the asterisk indicates complex conjugate. Note that in the process of time averaging over one RF period only the r and z components of $\bar{\boldsymbol{F}}_\mathrm{L}$ remain. On timescales larger than the RF timescale the r and z components of the material derivative and of the divergence of the stress tensor are small compared to the respective components of the pressure gradient force [22, 96]. It is thus possible to simplify equation (3.57) to an analytic expression for the electron flux as

$$n_\mathrm{e}\boldsymbol{u}_\mathrm{e} = -\mu_\mathrm{e} n_\mathrm{e}\boldsymbol{E} + \frac{\mu_\mathrm{e} n_\mathrm{e}}{\mathrm{e}}\bar{\boldsymbol{F}}_\mathrm{L} - \mu_\mathrm{e}\nabla n_\mathrm{e} T_\mathrm{e}, \tag{3.61}$$

where the electron mobility $\mu_\mathrm{e} = \frac{\mathrm{e}}{m_\mathrm{e}\nu_\mathrm{e,n}}$ is measured in units of $\mathrm{m^2V^{-1}s^{-1}}$. Note that equation (3.61) has only r and z components, since $\partial_\varphi\phi_\mathrm{plasma} = \partial_\varphi n_\mathrm{e}T_\mathrm{e} = 0$.

By using equation (3.54) the φ component of equation (3.57) is expressed as algebraic equation

$$\mathrm{i}\omega_{\mathrm{RF}} m_{\mathrm{e}} \tilde{u}_{\mathrm{e,RF},\varphi} = -\mathrm{e}\tilde{E}_{\mathrm{RF},\varphi} + \tilde{F}_{\mathrm{L},\varphi} - \frac{1}{n_{\mathrm{e}}}[\nabla \cdot \underline{\underline{\boldsymbol{\pi}}}_{\mathrm{e}}]_{\varphi} - \sum_{\mathrm{n}} \mu_{\mathrm{e,n}} \nu_{\mathrm{e,n}} \tilde{u}_{\mathrm{e,RF},\varphi}, \tag{3.62}$$

where the time derivative and the viscosity $[\nabla \cdot \underline{\underline{\boldsymbol{\pi}}}_{\mathrm{e}}]_{\varphi}$ are retained but the advection term is neglected, as suggested by Chang et al. [96]. The φ component of the RF Lorentz force is calculated in equation (3.59) as

$$\tilde{F}_{\mathrm{L},\varphi} = -\mathrm{e}\left(u_{\mathrm{e},z}\tilde{B}_{\mathrm{RF},r} - u_{\mathrm{e},r}\tilde{B}_{\mathrm{RF},z}\right). \tag{3.63}$$

The interplay between $\tilde{F}_{\mathrm{L},\varphi}$ and the viscosity are of high relevance for the RF power coupling and often omitted, as further detailed in sections 3.5.5 and 4.4.

Electron energy transport equation

The energy transport equation for the electrons is derived from equation (3.6). With $|\boldsymbol{u}_e| \ll v_{\mathrm{e,p}}$ follows

$$\partial_t(n_{\mathrm{e}}\frac{3}{2}\mathrm{e}T_{\mathrm{e}}) + \nabla \cdot \boldsymbol{Q}_{\mathrm{e}} = \bar{\mathcal{E}}_{\mathrm{ind}} - \mathcal{P}_{\mathrm{e}} - \mathrm{e}\, n_{\mathrm{e}} \boldsymbol{u}_{\mathrm{e}} \cdot \boldsymbol{E}, \tag{3.64}$$

where the inductive heating term $\bar{\mathcal{E}}_{\mathrm{ind}}$ is calculated in section 3.5.5. The electron energy losses due to elastic and inelastic collisions are

$$\mathcal{P}_{\mathrm{e}} = \sum_{\mathrm{n}} \frac{3}{2} k_{\mathrm{n,e}} n_{\mathrm{e}} \nu_{\mathrm{n,e}} (\mathrm{e}T_{\mathrm{e}} - k_{\mathrm{B}} T_{\mathrm{n}}) + \sum_{l_{\mathrm{e}}} \mathcal{R}_{l_{\mathrm{e}}} \Delta\epsilon_{l_{\mathrm{e}}}. \tag{3.65}$$

The variable l_{e} runs over all inelastic electron impact processes as stated in table 3.1 and the corresponding threshold energies $\Delta\epsilon_{l_{\mathrm{e}}}$ are taken from the references in the same table. Electrons can also gain energy from the electrostatic field $\boldsymbol{E}$ by Joule heating if $n_{\mathrm{e}}\boldsymbol{u}_{\mathrm{e}} \cdot \boldsymbol{E} < 0$ or loose energy for sustaining the electrostatic field when $n_{\mathrm{e}}\boldsymbol{u}_{\mathrm{e}} \cdot \boldsymbol{E} > 0$. The latter is typically the case in the plasma sheath. The electron

energy flux has three parts: convection, conduction and a part due to the viscous stress tensor

$$\boldsymbol{Q}_\mathrm{e} = \frac{5}{2}\mathrm{e}T_\mathrm{e} n_\mathrm{e} \boldsymbol{u}_\mathrm{e} + \boldsymbol{q}_\mathrm{e} + \overline{\underline{\boldsymbol{\pi}}_\mathrm{e} \boldsymbol{u}_\mathrm{e}}. \tag{3.66}$$

From equation (3.10) follows the electron heat flux density

$$\boldsymbol{q}_\mathrm{e} = -\overbrace{\frac{5}{2}\frac{n_\mathrm{e}\mathrm{e}T_\mathrm{e}}{m_\mathrm{e}\nu_\mathrm{e,n}}}^{\kappa_\mathrm{e}} \nabla \mathrm{e}T_\mathrm{e}, \tag{3.67}$$

where the thermal conductivity coefficient is denoted by κ_e. The momentum transfer frequency $\nu_\mathrm{e,n}$ due to collisions of the electrons with atoms and molecules is calculated according to equation (3.16). The RF-averaged contribution from the stress tensor in the electron energy flux is detailed in section 3.5.5.

3.5.5 Inductive RF power coupling

An electron is able to follow the electric RF field because of its small mass, i.e. $\omega_\mathrm{RF} \ll \omega_\mathrm{e,p} \approx 5.6 \cdot 10^{10}\,\mathrm{Hz}$ at $n_\mathrm{e} \approx 10^{18}\,\mathrm{m}^{-3}$, where the electron plasma frequency $\omega_\mathrm{e,p}$ is defined in equation (2.29). Hence the electrons contribute to the RF current density according to equation (3.55) that is needed to calculate the power absorption according to equation (2.35). $\tilde{u}_{\mathrm{e,RF},\varphi}$ in turn is obtained from the φ component of the electron momentum balance equation (3.62). Depending on the assumed skin effect regime as shown in figure 2.3 (local, anomalous or nonlinear) there are different approximations of equation (3.62).

In the *local regime* equation (3.62) is considerably simplified, i.e. the RF Lorentz force as well as the viscosity are neglected. This yields Ohm's law

$$\tilde{J}_{\mathrm{RF},\varphi} = \tilde{\sigma}_\mathrm{plasma} \tilde{E}_{\mathrm{RF},\varphi} \tag{3.68}$$

with the complex plasma conductivity from equation (2.32). This approach is commonly used to describe the power coupling in ICP models at pressures larger than 1 Pa and driving frequencies larger than 10 MHz, i.e. at small magnetic RF field amplitudes [97–99].

Discharges in the *anomalous regime* are modeled by retaining the viscosity term in equation (3.62). Using the simplified equation (3.11) yields

$$[\nabla \cdot \underline{\underline{\boldsymbol{\pi}}}_{\mathrm{e}}]_{\varphi} = -m_{\mathrm{e}} n_{\mathrm{e}} \eta_{\mathrm{e}} (\nabla^2 \tilde{u}_{\mathrm{e},\varphi} - \frac{\tilde{u}_{\mathrm{e},\varphi}}{r^2}). \tag{3.69}$$

Hagelaar has shown [51, 100] that the anomalous skin effect regime can be modeled by using an effective kinematic viscosity

$$\eta_{\mathrm{e,stoc}} = \left(\frac{4 c_0^2 \epsilon_0 T_{\mathrm{e}}^2}{\pi^2 m_{\mathrm{e}} \omega_{\mathrm{RF}} n_{\mathrm{e}}} \right)^{1/3}. \tag{3.70}$$

In this non-local limit $\eta_{\mathrm{e,stoc}}$ scales with $T_{\mathrm{e}}^{2/3}$ and does not depend on the collision frequency $\nu_{\mathrm{e,n}}$. It also scales with $\omega_{\mathrm{RF}}^{-1/3}$, i.e. it increases slightly when the applied frequency decreases. As can be seen in figure 2.3, the typical magnetic RF field amplitudes are rather small in the anomalous regime, wherefore the RF Lorentz force is commonly neglected.

Discharges in the *nonlinear regime* have to be described by a momentum balance where the RF Lorentz force is retained, because it plays a significant role in sustaining the discharges [54, 58]. In the region that lies above the nonlinear regime, i.e. at even higher B_{RF}, figure 2.3 suggests that there is a transition back to the local regime, because the Larmor radius of the electrons becomes so small that the particles behave as if they were in the local regime. However, simply using the local formulation from above in this high B_{RF} regime does not reproduce results obtained from experimental measurements. It is shown in section 4.4 that it is necessary to retain the RF Lorentz force and the viscosity term in the local Navier-Stokes limit, where Chang [96] obtains

$$\eta_{\mathrm{e,visc}} = \frac{2}{5} \mathrm{Pr}_{\mathrm{e}} \frac{\kappa_{\mathrm{e}}}{n_{\mathrm{e}}} = \frac{2}{3} \frac{\mathrm{e} T_{\mathrm{e}}}{m_{\mathrm{e}} \nu_{\mathrm{e,n}}}. \tag{3.71}$$

Herein the Prandtl number of the electrons $\mathrm{Pr}_{\mathrm{e}} = 2/3$. In this approximation $\eta_{\mathrm{e,visc}}$ increases with increasing electron temperature and decreases with increasing neutral particles densities, since $\nu_{\mathrm{e,n}} = X_{\mathrm{e,a}} n_{\mathrm{a}} + X_{\mathrm{e,m}} n_{\mathrm{m}}$. Note that also the viscosity from equation (3.71) is an approximation. In its derivation (as in the one for $\eta_{\mathrm{e,stoc}}$) unperturbed trajectories for the electrons are assumed, i.e. the influence of the

nonlinear Lorentz force is not considered. Consequently, the scaling of η_e in the nonlinear regime could be different [50]. However, no analytic method exists for determining the effective viscosity coefficient in the nonlinear skin effect regime.

The interplay between the RF Lorentz force and the viscosity in the electron momentum transport equation is intricate. Moreover, this interplay is fundamentally important for the RF coupling mechanism in the nonlinear regime, as further elaborated in section 4.4.

The inductive heating is accounted for in the electron energy transport equation (3.64) as RF-averaged quantity

$$\bar{\mathcal{E}}_\mathrm{ind} = \frac{\omega_\mathrm{RF}}{2\pi}\int_0^{2\pi/\omega_\mathrm{RF}} -\mathrm{e}\, n_\mathrm{e}\boldsymbol{u}_\mathrm{e}\cdot\boldsymbol{E}_\mathrm{RF}\,\mathrm{d}t = \frac{1}{2}\mathrm{Re}\{-\mathrm{e}\, n_\mathrm{e}\tilde{u}_{\mathrm{e,RF},\varphi}\tilde{E}^*_{\mathrm{RF},\varphi}\}. \tag{3.72}$$

The power absorbed by the plasma is calculated by integrating over the plasma volume, i.e.

$$P_\mathrm{plasma} = \int_{\mathrm{V_{plasma}}} \bar{\mathcal{E}}_\mathrm{ind}\,\mathrm{d}V. \tag{3.73}$$

The energy transport term resulting from the kinematic viscosity in the electron energy transport equation (3.64) is obtained by averaging over one RF period as

$$\nabla\cdot\overline{\underline{\boldsymbol{\pi}}_\mathrm{e}\boldsymbol{u}_\mathrm{e}} = \frac{1}{2}\mathrm{Re}\{\nabla\cdot\left(-m_\mathrm{e}n_\mathrm{e}\eta_\mathrm{e}((\partial_r\tilde{u}_{\mathrm{e,RF},\varphi} - \frac{\tilde{u}_{\mathrm{e,RF},\varphi}}{r})\boldsymbol{e}_r + \partial_z\tilde{u}_{\mathrm{e,RF},\varphi}\boldsymbol{e}_z)\tilde{u}^*_{\mathrm{e,RF},\varphi}\right)\}. \tag{3.74}$$

3.5.6 External magnetostatic field

Because of the cylindrically symmetric simulation domain, an external magnetostatic field is in principle restricted to the following structure:

$$\boldsymbol{B}_0 = B_{0,r}(r,z)\boldsymbol{e}_r + B_{0,\varphi}(r,z)\boldsymbol{e}_\varphi + B_{0,z}(r,z)\boldsymbol{e}_z \tag{3.75}$$

The electrons are - in contrast to the ions - magnetized by the magnetostatic fields, as explained at the end of section 2.2. To account for this magnetization it is convenient to write the magnetized electron flux $n_\mathrm{e}\boldsymbol{u}_{\mathrm{e},\boldsymbol{B}_0}$ as an analytic function of the electron flux $n_\mathrm{e}\boldsymbol{u}_\mathrm{e}$ from equation (3.61) and the magnetic field $\boldsymbol{B}_0$. This is

achieved by combining equation (3.57) with its dot- and cross-products with $\boldsymbol{B}_0$ [22]. It follows

$$n_\mathrm{e}\boldsymbol{u}_{\mathrm{e},\boldsymbol{B}_0} = \frac{1}{1+h_\mathrm{e}^2}\left(n_\mathrm{e}\boldsymbol{u}_\mathrm{e} + \mu_\mathrm{e}^2(\boldsymbol{B}_0 \cdot n_\mathrm{e}\boldsymbol{u}_\mathrm{e})\boldsymbol{B}_0 + \mu_\mathrm{e}\boldsymbol{B}_0 \times n_\mathrm{e}\boldsymbol{u}_\mathrm{e}\right), \tag{3.76}$$

where the Hall parameter for the electrons $h_\mathrm{e} = \mu_\mathrm{e}B_0$ is defined in equation (2.23). By using equation (3.61) the drift flux in the fluid picture $\mu_\mathrm{e}\boldsymbol{B}_0 \times n_\mathrm{e}\boldsymbol{u}_{\mathrm{e},\boldsymbol{B}=0}$ can be written as a sum of an $\boldsymbol{E} \times \boldsymbol{B}_0$ drift, a diamagnetic $\nabla n_\mathrm{e}T_\mathrm{e} \times \boldsymbol{B}_0$ fluid drift (cf. [37, 101]) and a drift that is associated with the RF-averaged component of the Lorentz force. Note that all drifts are in φ direction and therefore form closed loops. Hence the plasma transport in the r and z directions is not affected by these drifts. The magnetized electron heat flux $\boldsymbol{q}_{\mathrm{e},\boldsymbol{B}_0}$ is obtained in a similar way as the electron particle flux in equation (3.76), i.e.

$$\boldsymbol{q}_{\mathrm{e},\boldsymbol{B}_0} = \frac{1}{1+h_\mathrm{e}^2}\left(\boldsymbol{q}_\mathrm{e} + \mu_\mathrm{e}^2(\boldsymbol{B}_0 \cdot \boldsymbol{q}_\mathrm{e})\boldsymbol{B}_0 + \mu_\mathrm{e}\boldsymbol{B}_0 \times \boldsymbol{q}_\mathrm{e}\right). \tag{3.77}$$

3.5.7 Boundary conditions

Electrostatic field

The driver and source back-plates, as well as the walls of the expansion region (inclusive the plasma grid) shown in figure 3.2 are conducting. Hence a zero Dirichlet boundary condition for the potential at these walls is applied, i.e.

$$\phi_\mathrm{plasma}\Big|_\mathrm{wall} = 0. \tag{3.78}$$

Ions

It is assumed that the positive ion species $\mathrm{i} \in \{\mathrm{H}^+, \mathrm{H}_2^+, \mathrm{H}_3^+\}$ recombine at the walls. Hence equation (3.17) reduces for a drifting Maxwellian distribution function (see equation (3.20)) to

$$n_\mathrm{i}\boldsymbol{u}_\mathrm{i} \cdot \hat{\boldsymbol{n}} = n_\mathrm{i}u_{\mathrm{i,eff}} = \frac{n_\mathrm{i}}{2\pi^{1/2}}\left(\pi^{1/2}u_{\mathrm{i},\perp}(1+\mathrm{erf}\left(\frac{u_{\mathrm{i},\perp}}{v_{\mathrm{i,p}}}\right)) + v_{\mathrm{i,p}}\exp\left(\frac{-u_{\mathrm{i},\perp}^2}{v_{\mathrm{i,p}}^2}\right)\right). \tag{3.79}$$

Electromagnetic fields

The metallic surfaces such as the driver-, source- and expansion back-plates as well as the expansion axial wall (see figure 3.2) are assumed to be perfect conductors. For this reason the electric field component parallel to the conducting surface has to vanish, i.e.

$$\hat{\boldsymbol{n}} \times \tilde{\boldsymbol{E}}_{\mathrm{RF}} = 0. \tag{3.80}$$

Also the surfaces that bound the simulation domain are assumed to be perfect conductors. Their distances from any relevant structure such as plasma, the RF coil and the backplates are chosen, such that the effect of this boundary condition on the RF fields around this relevant structure is negligible.

At the coil windings a surface current in φ direction $J_{\mathrm{surf},\varphi}$ is applied to excite the system, i.e.

$$\hat{\boldsymbol{n}} \times \tilde{\boldsymbol{B}}_{\mathrm{RF}} = \mu_0 J_{\mathrm{surf},\varphi}. \tag{3.81}$$

Electrons

As introduced in section 2.2 the electron mean free path is large compared to the size of the plasma sheath, which is in the order of the Debye length. Therefore the plasma sheath is assumed to be collisionless. Hence the electron flux towards the wall is calculated using a Maxwellian distribution function without a drift. From equation (3.21) follows

$$n_{\mathrm{e}} \boldsymbol{u}_{\mathrm{e}} \cdot \hat{\boldsymbol{n}} = n_{\mathrm{e}} \frac{v_{\mathrm{e,p}}}{2\pi^{1/2}}. \tag{3.82}$$

Consequently, the electron heat flux towards the walls is calculated from equation (3.25) as

$$\boldsymbol{Q}_{\mathrm{e}} \cdot \hat{\boldsymbol{n}} = n_{\mathrm{e}} \frac{v_{\mathrm{e,p}}}{2\pi^{1/2}} 2\mathrm{e}T_{\mathrm{e}}. \tag{3.83}$$

3.5.8 Excitation of the system

As described in section 3.5.7, a surface current $J_{\mathrm{surf},\varphi}$ is applied to excite the RF magnetic field. The amplitude of this surface current is related to the the RF current amplitude I_0 as

$$I_0 = \pi d_{\mathrm{coil}} J_{\mathrm{surf},\varphi}. \tag{3.84}$$

Herein $d_{\mathrm{coil}} = 6\,\mathrm{mm}$ is the diameter of the RF coil winding. The RF coil does not produce a relevant far field, wherefore the generator output power $P_{\mathrm{generator}}$ is either absorbed by the plasma or in the RF coil and in other metallic components. These are e.g. the Faraday screen and the back plates, where eddy currents are induced. Hence the power balance for the system

$$P_{\mathrm{generator}} = P_{\mathrm{plasma}} + \frac{1}{2} R_{\mathrm{network}} I_0^2 \tag{3.85}$$

must hold. The network resistance R_{network} is a model input that accounts for the above mentioned losses in the RF coil and in the other metallic components. For the current setup of the BUG ion source, its value is $R_{\mathrm{network}} = (0.6 \pm 0.07)\,\Omega$, as determined in section 4.2.2. For different RF coil, driver and Faraday screen geometries R_{network} varies considerably, wherefore it has to be calculated in these cases. For this purpose a 3D electromagnetic model of the BUG driver was established, as explained in section 3.6.

To excite the system an integral controller controls I_0 at any time t, i.e.

$$I_0(t) = K_{\mathrm{i}} \int_0^t (P_{\mathrm{set}} - P_{\mathrm{is}}(\tau))\mathrm{d}\tau. \tag{3.86}$$

Herein, P stands for either the power absorbed by the plasma P_{plasma} or the generator output power $P_{\mathrm{generator}}$, i.e. the user can either specify a $P_{\mathrm{plasma,set}}$ or $P_{\mathrm{generator,set}}$ at the beginning of each simulation run. The integral gain K_{i} is chosen such that the system is smoothly ramped up to the steady state value of I_0, where the actual plasma power $P_{\mathrm{plasma,is}}$ (or $P_{\mathrm{generator,is}}$) equals the set value $P_{\mathrm{plasma,set}}$ (or $P_{\mathrm{generator,set}}$). The integral gain K_{i} has no influence on the obtained steady state, but changes only the behavior during the plasma startup phase.

3.6 3D EM model to calculate network losses

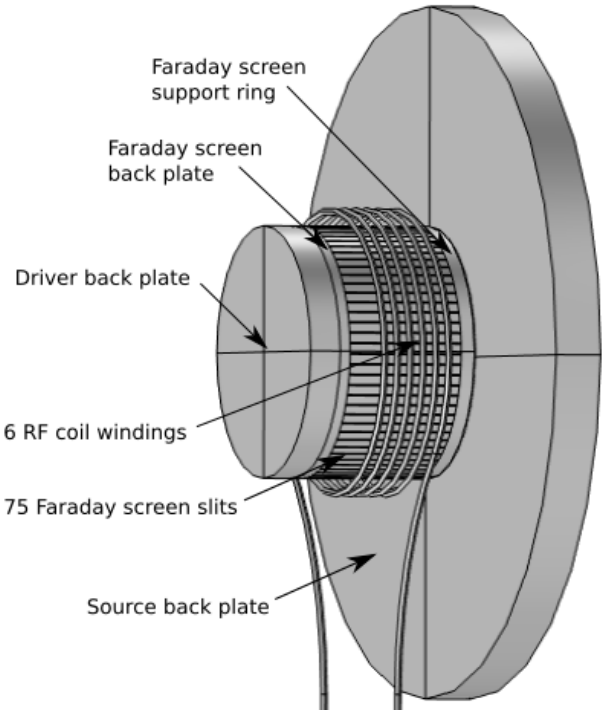

Figure 3.3: *Simulation domain of the 3D electromagnetic model used to calculate the network losses in the components of the BUG ion source driver.*

Measurements at a mock-up of the BUG ion source driver revealed, that eddy current losses in the Faraday screen account for roughly 74% of the network losses, whereas direct Joule heating of the RF coil accounts for 26% of the network losses [24]. Hence only a negligibly small fraction of the power is lost in the back plates. To model the losses in the Faraday screen and in the RF coil as accurately as possible, a 3D electromagnetic (EM) model of the BUG ion source driver has been established in a master thesis [102]. This model is similar to preexisting models [103]. The simulation domain accounts for the complex 3D structure of the Faraday screen, the RF coil and the back plates, as shown in figure 3.3. In this simulation domain, the driver and Faraday screen geometry are simplified. Most importantly, instead of the z-shaped Faraday screen slits as used in the experiment, straight ones are used in this simulation domain, because otherwise it is not possible to solve the model on a workstation due to memory restrictions.

Using the simplified 3D EM model results in a value of R_{network} that is by a factor of $0.6/0.54 \approx 1.11$ too small compared to the experimentally obtained one. However, in the validation of the 3D EM model it was found that the deviation between the experimental and modeled R_{network} stems from the larger surface of the z-shaped Faraday screen slits in the experiment. Further details about the model verification and validation are documented in [102]. The validated 3D EM model is used in this work to calculate the network resistance R_{network} and inductance L_{network} for geometries that deviate from the current BUG ion source configuration. It is important to consider the change in R_{network} to correctly capture the trend of η when an external parameter is changed. This will be shown in the performed optimization studies in chapter 5. The inductance L_{network} is needed to estimate the effective coil voltage via equation (2.26).

3.7 Implementation

The following measures are essential for obtaining a steady state numerical solution of the highly nonlinear coupled system of continuous partial differential equations (PDEs) that describe the evolution of all species as well as the electrostatic and electromagnetic fields. To perform these measures the COMSOL Multiphysics® simulation software [104] is used as indicated in the enumeration below.

1. *Numerical stabilization:* Advection dominates over diffusion in the ion particle and momentum transport equations (3.46) and (3.47). Hence both equations are inherently unstable and oscillations in the densities and velocities occur, which causes the time stepping to seize up [105]. In order to avoid this, a small amount of numerical diffusion proportional to the local mesh cell size and ion drift velocity is added in the ion particle and momentum balances. The added numerical diffusion is small enough such that it does not affect the ion densities and velocities and thus only serves as a numerical stabilization.

2. *Exponential formulation:* Owing to steep gradients of the charged particles densities in the vicinity of the walls (especially during the plasma startup phase), charged particle densities can become smaller than zero for numerical reasons. This is unphysical and produces feedback loops (e.g. the densities

are used in the calculation of the reaction rates) that cause the time stepping to seize up. To avoid this, all densities are transformed with $n = \exp(N) > 0$ and the particle transport equations are formulated for the transformed variable N. The same is done for the electron temperature. In this way the nonlinearity of the system increases but the more robust handling of the steep gradients outweighs this disadvantage by far.

3. *Nonlinearity:* The Joule heating term in equation (3.64), the Lorentz force from equations (3.60) and (3.63) and the terms involving the kinematic viscosity in equations (3.69) and (3.74) considerably increase the nonlinearity of the PDE system. This is especially true during the plasma startup phase and leads to unnecessary restrictive settings in the error tolerance level for the (non)-linear solver. As a consequence the time stepping controller is forced to decrease the time steps to unnecessary small values. To circumvent this problem, the terms from above are introduced smoothly by means of a hyperbolic tangent function only after quasi-neutrality has set in at around 10^{-3} s. It was checked that in this way the same steady state is reached as when the terms are present from the beginning. However the calculation time needed to get to the steady state is reduced by roughly one order of magnitude.

4. *Numerical mesh:* The simulation domain shown in figure 3.2 is superimposed by around 20,000 non-uniform triangles with typical cell sizes not larger than 5 mm in the plasma domain. Near structures such as the RF coil or corners in the plasma domain the mesh size is reduced to around 1 mm. A boundary layer is formed by the last five rectangular elements in front of the plasma facing walls with decreasing cell lengths down to 0.1 mm. This is necessary to resolve the steep density and velocity gradients that develop in the vicinity of the walls. The mesh is generated with COMSOL Multiphysics®.

5. *Spatial discretization:* For the discretization in space, the finite element method is used [105–107]. Continuous weak forms for the Poisson equation, the particle, momentum and energy transport equations of the charged particles (except for the analytic electron particle fluxes (3.61)) and neutrals

are derived and implemented in the weak formulation interface of COMSOL Multiphysics®. Here a formalism similar to the unified form language is used [108]. For the calculation of the electromagnetic RF fields $\boldsymbol{E}_{\mathrm{RF}}$ and $\boldsymbol{B}_{\mathrm{RF}}$ COMSOL Multiphysics® offers the AC/DC physics interface, where the weak forms of the wave equation for the vector potential are provided. These are used for convenience. However, because of the great freedom and flexibility that the direct weak form implementation provides, i.e. every PDE that can be written down on paper can be implemented as a weak form, this approach is generally preferred. For all weak forms linear Lagrangian basis functions are used as shape functions. Using the same basis for the test functions and plugging both into the weak form results in a system of ordinary differential equations (ODEs) for typically around 130,000 unknown nodal coefficients.

6. *Time discretization and time stepping:* The integral controller for the RF current amplitude in equation (3.86) is rewritten as an ODE and implemented in the ODE interface of COMSOL Multiphysics®. Together with the ODE system resulting from the spatial discretization it is then discretized in time by an implicit backward differentiation formula (BFD) method. This discretization as well as the controlling of the time step is automatically done by COMSOL Multiphysics®. The simulation is stopped when the neutrals, which have the slowest time scale, are in a steady state. This is typically the case at around 1 s. Since the BDF method is implicit the Courant-Friedrichs-Lewy condition does not apply. Therefore the time steps are increased considerably from 10^{-11} s for the first few time steps to time steps as large as 0.1 s towards the end of the simulation.

7. *Solving the nonlinear problems:* Since the ODE system is highly nonlinear a damped Newton scheme has to be used in each time step. The systems of linear equations appearing multiple times during this Newton scheme are solved by a direct solver. This is also handled by COMSOL Multiphysics® internally. The user can tune parameters such as damping and error tolerance levels.

8. *Numerical performance:* The model is solved on a workstation with 6 cores (Intel64 Family 6 Model 62 processors at 3.5 GHz) and 128 GB RAM. One run takes approximately three hours to reach the steady state solution.

3.8 Work flow

Performing a simulation involves typically the following steps that have to be executed depending on the specific use case.

1. For all validation studies, the driver and coil geometries as shown in figure 3.2 are the same as in the experiment. Hence the experimentally obtained network resistance is used as an input in the RF power coupling model. However, in the optimization studies, different driver and coil geometries are investigated. In these cases the network resistance R_{network} is calculated from the 3D electromagnetic model, as explained in section 3.6. The resulting R_{network} as a function of the varied geometric quantity is then used in the RF power coupling model as an input.

2. The neutrals module from section 3.4 is executed with hydrogen molecules as the only species, i.e. only the particle and momentum transport equations for the molecules are solved for the variables n_{m} and $\boldsymbol{u}_{\mathrm{m}}$, respectively. The transparency of the plasma grid t_{grid} is adjusted as described in section 4.3. In this way the filling pressure is as measured in the experiment.

3. The RF power coupling model, i.e. the plasma module together with the neutrals module, is solved. Hereby R_{network} from step one and the inlet flux from step two are used. The other input parameters as well as the calculated model outputs are shown in table 3.4.

Table 3.4: *Inputs and outputs of the RF power coupling model.*

Quantity	*Measured or calculated model input*
Set power	Either $P_{\mathrm{generator,set}}$ or $P_{\mathrm{plasma,set}}$
Driving frequency	f_{RF}
Network resistance	R_{network}
Influx of H_2	$\Gamma_{\mathrm{m,inj}}$ and $\Theta_{\mathrm{m,inj}}$
Coil and discharge geometry	see figure 3.2

Quantity	*Calculated model output*
Atoms density	$n_{\mathrm{a}}(r,z,t)$
Atoms velocity	$\boldsymbol{u}_{\mathrm{a}}(r,z,t) = u_{\mathrm{a},r}(r,z,t)\boldsymbol{e}_r + u_{\mathrm{a},z}(r,z,t)\boldsymbol{e}_z$
Atoms temperature	$T_{\mathrm{a}}(r,z,t)$
Molecules density	$n_{\mathrm{m}}(r,z,t)$
Molecules velocity	$\boldsymbol{u}_{\mathrm{m}}(r,z,t) = u_{\mathrm{m},r}(r,z,t)\boldsymbol{e}_r + u_{\mathrm{m},z}(r,z,t)\boldsymbol{e}_z$
Molecular temperature	$T_{\mathrm{m}}(r,z,t)$
Electron density	$n_{\mathrm{e}}(r,z,t)$
Electron (RF) velocity	$\boldsymbol{u}_{\mathrm{e}}(r,z,t) = u_{\mathrm{e},r}(r,z,t)\boldsymbol{e}_r + u_{\mathrm{e},z}(r,z,t)\boldsymbol{e}_z + \mathrm{Re}\{\tilde{u}_{\mathrm{e,RF},\varphi}(r,z)\exp(\mathrm{i}\omega_{\mathrm{RF}}t)\}\boldsymbol{e}_\varphi$
Electron temperature	$T_{\mathrm{e}}(r,z,t)$
Ion densities for $\mathrm{i} \in \{\mathrm{H}^+, \mathrm{H}_2^+, \mathrm{H}_3^+\}$	$n_{\mathrm{i}}(r,z,t)$
Ion velocities	$\boldsymbol{u}_{\mathrm{i}}(r,z,t) = u_{\mathrm{i},r}(r,z,t)\boldsymbol{e}_r + u_{\mathrm{i},z}(r,z,t)\boldsymbol{e}_z$
Electrostatic potential	$\phi_{\mathrm{plasma}}(r,z,t)$
RF electric field	$\boldsymbol{E}_{\mathrm{RF}}(r,z,t) = \mathrm{Re}\{\tilde{E}_{\mathrm{RF},\varphi}(r,z)\exp(\mathrm{i}\omega_{\mathrm{RF}}t)\}\boldsymbol{e}_\varphi$
RF magnetic field	$\boldsymbol{B}_{\mathrm{RF}}(r,z,t) = \mathrm{Re}\{\tilde{B}_{\mathrm{RF},r}(r,z)\exp(\mathrm{i}\omega_{\mathrm{RF}}t)\}\boldsymbol{e}_r + \mathrm{Re}\{\tilde{B}_{\mathrm{RF},z}(r,z)\exp(\mathrm{i}\omega_{\mathrm{RF}}t)\}\boldsymbol{e}_z$
RF coil current amplitude	I_0
Calculated power	Either P_{plasma} or $P_{\mathrm{generator}}$
RF power transfer efficiency	$\eta = P_{\mathrm{plasma}}/P_{\mathrm{generator}}$
Plasma resistance	$R_{\mathrm{plasma}} = 2P_{\mathrm{plasma}}/I_0^2$
Effective coil voltage	$U_{\mathrm{coil,eff}} \approx \omega_{\mathrm{RF}} L_{\mathrm{network}} I_0/\sqrt{2}$

4 Model verification and validation

4.1 Verification

The aim is to verify that the partial differential equations (PDEs) from chapter 3 are implemented correctly. To reduce the complexity of the fully coupled system, the PDEs are verified separately, whenever this is possible.

For solving Maxwell's equations for the electromagnetic fields, the AC/DC physics interface provided by the COMSOL Multiphysics® simulation software is used, as stated in section 3.7. In this interface the weak expressions are implemented in cylindrical symmetry and the user only has to specify boundary conditions and material properties. To reduce errors, dimensional analysis is routinely applied by COMSOL Multiphysics® to verify the user defined expressions. The correct implementation of this physics interface is checked by using a simplified geometry, where analytic solutions are available for comparison. For this purpose a multi-coil arrangement in vacuum is created in cylindrical symmetry. By increasing the number of coil turns it is shown that the calculated fields approach the analytic solution for an infinite coil, as given by the textbook [39]. The same check is successfully repeated by setting a user defined uniform analytic plasma conductivity, as given by equation (2.32).

To verify Poisson's equation in the plasma module, the method of manufactured solutions is applied [109]. In this method a non-trivial analytic function is assumed for the potential ϕ_{plasma}. Hereby care has to be taken that the analytic ϕ_{plasma} satisfies the homogeneous Dirichlet boundary condition from equation (3.78). Inserting the analytic ϕ_{plasma} into Poisson's equation (3.45) results in an analytic expression for the charge density profile, which is used in the implemented weak expression.

Finally, it is checked that the potential calculated from the analytic charge density profile reproduces the analytic potential.

In the neutrals module transport equations for the number density, momentum and energy are solved. When only the molecules are simulated, then it must be true in steady state that the total influx at the inlet equals the total outflux at the plasma grid. This is so since at the walls all incident molecules are reflected, as stated in table 3.3, and there are neither gains nor losses of molecules in the volume. It is checked that in steady state the flux at the inlet is balanced by the outflux through the plasma grid. In this case the resulting directed velocities towards the discharge walls are zero.

The charged particles transport equations in the plasma module are verified by checking their conservation properties in steady state, i.e. for each species the integrated particle flux over all boundaries has to be balanced by the volume particle gains. For the electrons also the energy transport equation is solved. To verify the implementation of this equation, a fixed artificial power deposition profile is assumed. It is then checked that the electron energy gain by the artificial power deposition is equal to the losses for sustaining the electrostatic field, the (in-)elastic losses in volume and the energy losses at all surfaces.

In summary, all PDEs from chapter 3 are verified successfully.

4.2 Experimental setup for validation

The physics of the different modules as described in chapter 3 are validated with experimental measurements performed directly at the BUG ion source. The following subsections provide an overview over the diagnostics used to obtain the most important model input and output quantities (cf. table 3.4) that are used for model validation. A brief overview of the experimental diagnostics and the evaluation methods that are described in the following subsections have already been published [24].

4.2.1 Inlet gas flux

One of the design criteria for the ITER-NNBI is that the filling pressure p_{fill}, i.e. the gas pressure in the ion source before plasma ignition, has to be at or below 0.3 Pa [3]. In the BUG ion source a specific p_{fill} is achieved by setting a specific pV-throughput

$$q_{pV} = p_{\text{m,inj}} \dot{V}_{\text{m,inj}} = \dot{N}_{\text{m,inj}} k_{\text{B}} T_{\text{m,inj}} \tag{4.1}$$

via a gas flow controller. Here the molecular pressure, volume flow, particle flow and temperature are denoted by $p_{\text{m,inj}}$, $\dot{V}_{\text{m,inj}}$, $\dot{N}_{\text{m,inj}}$ and $T_{\text{m,inj}}$, respectively. The filling pressure is measured with pressure gauges at several positions in the expansion chamber. By changing the pV-throughput the gas flow calibration curve

$$q_{pV}(p_{\text{fill}}) = C_{\text{grid}} \left(p_{\text{fill}} - 2.54 \cdot 10^{-2}\,\text{Pa} \right) \tag{4.2}$$

is obtained. Here the experimentally determined vacuum conductivity of the grid stack is $C_{\text{grid}} = 0.9606\,\text{m}^3\text{s}^{-1}$. Equating equations (4.1) and (4.2) yields the particle flux

$$\dot{N}_{\text{m,inj}} = \frac{C_{\text{grid}}}{k_{\text{B}} T_{\text{m,inj}}} \left(p_{\text{fill}} - 2.54 \cdot 10^{-2}\,\text{Pa} \right), \tag{4.3}$$

where $T_{\text{m,inj}} = 300\,\text{K}$ is assumed at the inlet valve.

4.2.2 Electrical diagnostics

The RF coil current amplitude I_0 is obtained with an RF current monitor (Pearson model 8537) that is installed at the straight feed line part of the RF coil, as depicted in figure 4.1. The relative error for this diagnostic results from the reading accuracy on the oscilloscope that displays the value and is thus estimated as $\frac{\Delta I_0}{I_0} \approx \pm 5\%$. Without plasma operation, i.e. for $P_{\text{plasma}} = 0$, equation (2.24) becomes

$$P_{\text{generator}} = \frac{1}{2} R_{\text{network}} I_0^2. \tag{4.4}$$

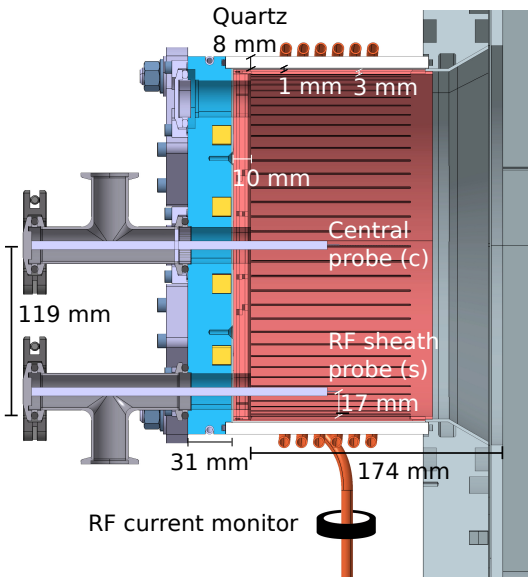

Figure 4.1: *Diagnostics used in the BUG experimental setup. The RF coil current amplitude I_0 is determined by an RF current monitor. The local plasma parameters electron density n_e, temperature T_e and plasma potential ϕ_{plasma} are obtained from two Langmuir probes, one located in the driver center and the other in the RF sheath. Figure adapted from [24].*

The generator output power is measured by directional couplers in the RF generator and the relative error is specified in the datasheet as $\frac{\Delta P_{generator}}{P_{generator}} \leq \pm 10\%$ [46]. Using equation (4.4), the network resistance $R_{network}$ is obtained from the slope of a linear best fit, as shown in figure 4.2. The resulting network resistance is

$$R_{network} = (0.60 \pm 0.07)\,\Omega. \tag{4.5}$$

Its measurement error results from an error calculation where a confidence level of 95% is used. In this experiments only small generator output powers less than 15 kW are used to protect the RF coil and the Faraday screen from high heat loads. Furthermore, it is ensured by slightly changing the applied frequency in the range of a few kHz, that $P_{generator}$ equals the forward power and the reflected power is zero, i.e. perfect matching is achieved. The network resistance is unaffected by the presence of plasma, since the main losses are in the Faraday screen and in the RF coil (cf. [24]), where no plasma is present, which would be capable of screening

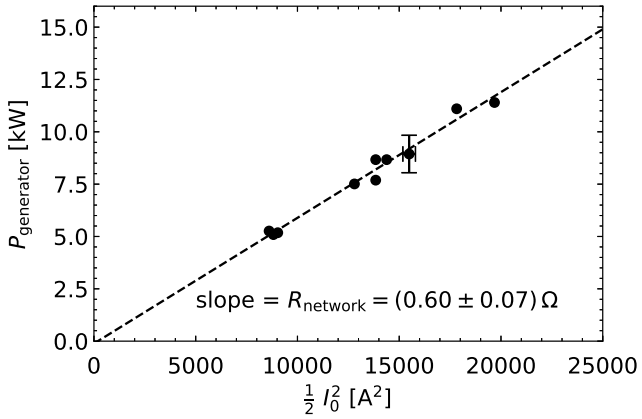

Figure 4.2: *The output generator power $P_{\text{generator}}$ as a function of $\frac{1}{2}I_0^2$. A linear best fit is used to determine the network resistance R_{network} from the slope of the regression line. Figure adapted from [24].*

the RF fields. Hence the RF power transfer efficiency can be calculated using equation (2.24) as

$$\eta = \frac{P_{\text{plasma}}}{P_{\text{generator}}} = 1 - \frac{\frac{1}{2}R_{\text{network}}I_0^2}{P_{\text{generator}}}. \tag{4.6}$$

This so called subtractive method was first described by [14]. The relative measurement error $\frac{\Delta\eta}{\eta} \approx \pm 10\%$ results from a Gaussian error propagation scheme applied to equation (4.6).

4.2.3 Plasma diagnostics

The plasma potential, electron temperature and electron density are obtained from two Langmuir probes, as illustrated in figure 4.1. One probe is located in the center of the driver and the other one 17 mm radially away from the inner surface of the Faraday screen. As introduced in section 2.3.2 the position of the latter probe is in the direct vicinity of the RF skin depth. Quantities obtained with the central probe are denoted by the index c, i.e. $\phi_{\text{plasma,c}}, T_{\text{e,c}}$ and $n_{\text{e,c}}$, whereas quantities obtained with the probe located in the RF sheath are denoted by the index s, i.e. $\phi_{\text{plasma,s}}, T_{\text{e,s}}$ and $n_{\text{e,s}}$. Both probes are not RF compensated, wherefore the electron branches of the obtained I-V characteristics that are exemplarily shown in figure 4.3 are

subject to RF noise [110]. For this reason the commonly used evaluation method,

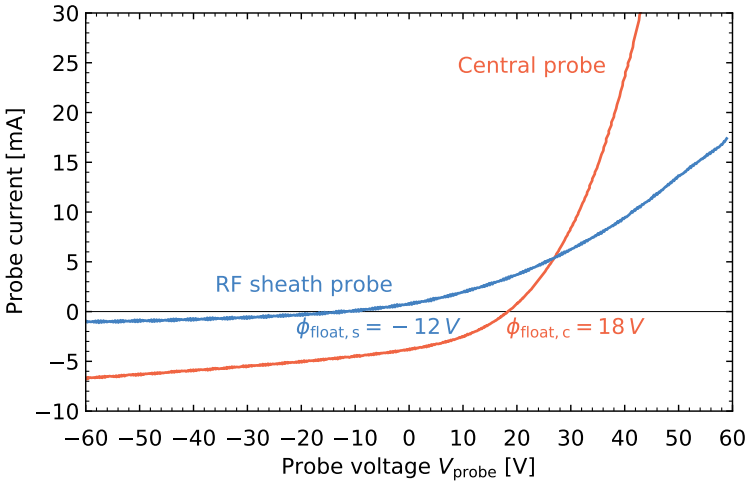

Figure 4.3: *Two typical I-V characteristics, obtained at* $P_{\text{generator}} = 40\,\text{kW}$ *and* $p_{\text{fill}} = 0.5\,\text{Pa}$ *in the driver center and in the RF sheath. The floating potentials are 18 and -12 V, respectively. Figure adapted from [24].*

i.e. directly probing the electron distribution function via the second derivative of the I-V characteristic with the well known Druyvesteyn formula [111] cannot be applied. Hence another approach is followed, as proposed by Chen [110, 112]. Firstly, the effective ion density $n_{\text{i,eff}}$ is obtained from the ion branch of the I-V characteristic, that is not affected by the RF magnetic field. Here the orbital motion limited (OML) theory [113] is applied. For the OML to be applicable the radius of the probe tip r_{probe} has to be smaller than the plasma sheath around the probe, which is around $5\lambda_{\text{De}}$. For a typical plasma in the driver with $T_{\text{e}} \approx 10\,\text{eV}$ and $n_{\text{e}} \approx 10^{18}\,\text{m}^{-3}$ this assumption is reasonably fulfilled, because

$$r_{\text{probe}} = 25\,\mu\text{m} \ll 118\,\mu\text{m} \approx 5\lambda_{\text{De}}. \tag{4.7}$$

Hence the ion branch of the I-V characteristic can directly be fitted by the OML formula

$$I_{\text{i,OML}} = -A_{\text{probe}} n_{\text{i,eff}} \text{e} \frac{\sqrt{2}}{\pi} \left(\frac{\text{e}(\phi_{\text{space}} - V_{\text{probe}})}{m_{\text{i,eff}}} \right)^{1/2}. \tag{4.8}$$

Herein, A_{probe}, V_{probe} and $m_{\mathrm{i,eff}}$ denote the surface of the cylindrical probe tip, the applied probe voltage and the effective ion mass, respectively. The latter is estimated assuming a mixture of 20% H_3^+, 40% H_2^+ and 40% H^+ [69]. The measured I-V characteristic is fitted with equation (4.8), where the two fitting parameters are $n_{\mathrm{i,eff}}$ and the space potential ϕ_{space}.

The fit is done starting from the lowest voltage around -60 V to values of -20 V for the central probe and to -40 V for the RF sheath probe. This ensures that in both cases the measured current is mainly consisting of ions. The measurement error of the evaluated quantities is essentially determined by the boundaries, up to which the ion current is fitted. The resulting relative error is $\frac{\Delta n_{\mathrm{i,eff}}}{n_{\mathrm{i,eff}}} \approx 25\%$. Subtracting the OML ion current from the measured I-V characteristic yields the electron current I_{e}. Quasi-neutrality is then used to obtain the electron density from the effective ion density, i.e. $n_{\mathrm{e}} \approx n_{\mathrm{i,eff}}$. Using this electron density and the assumption of a Maxwellian electron distribution function, the plasma potential ϕ_{plasma} and the electron temperature T_{e} are obtained from a fit to the electron current [110]:

$$I_{\mathrm{e}} = A_{\mathrm{probe}} n_{\mathrm{e}} \mathrm{e} \frac{1}{4} v_{\mathrm{th,e}} \exp\left(\frac{V_{\mathrm{probe}} - \phi_{\mathrm{plasma}}}{\mathrm{e}T_{\mathrm{e}}}\right). \tag{4.9}$$

The relative errors for the electron temperature and for the plasma potential result again from the different voltages up to which the OML fit is done. Its values are estimated as $\frac{\Delta T_{\mathrm{e}}}{T_{\mathrm{e}}} \approx \frac{\Delta \phi_{\mathrm{plasma}}}{\phi_{\mathrm{plasma}}} \approx 20\%$. The different steps described above are also shown in figure 4.4.

Because of the large RF magnetic field well above 100 G in the RF sheath it is not possible to evaluate $T_{\mathrm{e,s}}$ and $\phi_{\mathrm{plasma,s}}$ from the electron branch of the probe in the RF sheath, since the cross field mobility of the electrons onto the probe is considerably decreased. This is evident from the I-V characteristic shown in figure 4.3, where the electron current remains low even for high applied voltages of up to 60 V. However, it is possible to obtain the central $T_{\mathrm{e,c}}$ and $\phi_{\mathrm{plasma,c}}$ as described above, because the RF skin effect considerably damps the RF magnetic field in the center of the driver.

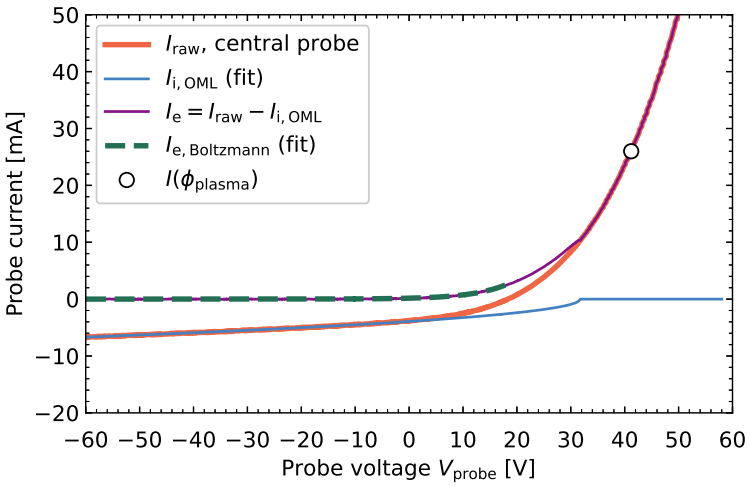

Figure 4.4: *Different steps used in the fitting routine for obtaining the plasma parameters from the I-V characteristic, exemplarily shown for the central probe at* $p_{\text{fill}} = 0.5\,\text{Pa}$ *and* $P_{\text{generator}} = 40\,\text{kW}$.

4.3 Neutrals module validation

As described in section 3.8, an initial run of the fluid model is performed, where only the particle and momentum transport equations of the hydrogen molecules are solved. This is done to find the correct value of the plasma grid transparency t_{grid}. To set up this simulation, the inlet particle flux at the H_2 inlet boundary (see figure 3.2) is set to the experimentally measured value

$$\Gamma_{\text{m,inj}} = \frac{\dot{N}_{\text{m,inj}}}{A_{\text{inlet}}} = \frac{\dot{N}_{\text{m,inj}}}{\pi r_{\text{inlet}}^2}, \tag{4.10}$$

as given by equation (4.3). The radius for the circular inlet is $r_{\text{inlet}} = 1.25\,\text{cm}$, as in the experiment. Using a linearly or parabolically decreasing inlet flux profile instead of the radially constant $\Gamma_{\text{m,inj}}$ in equation (4.10) does not change the molecular density and velocity in the volume but affects only the direct vicinity of the inlet. As cylindrical symmetry is assumed in the model, a direct representation of the rectangular plasma grid shape, as shown in figure 2.1 is not possible. Therefore, the rectangular plasma grid is converted to a circular one by holding the total

area of the plasma grid constant. The resulting radius of the plasma grid in the simulation domain is $r_{\mathrm{grid}} = 6.46\,\mathrm{cm}$, as shown in figure 3.2.

The experimentally obtained gas flow calibration curve as given by equation (4.2) and the numerically calculated ones for three different values of t_{grid} are shown in figure 4.5. Hereby the values of p_{fill} obtained from the model are calculated as

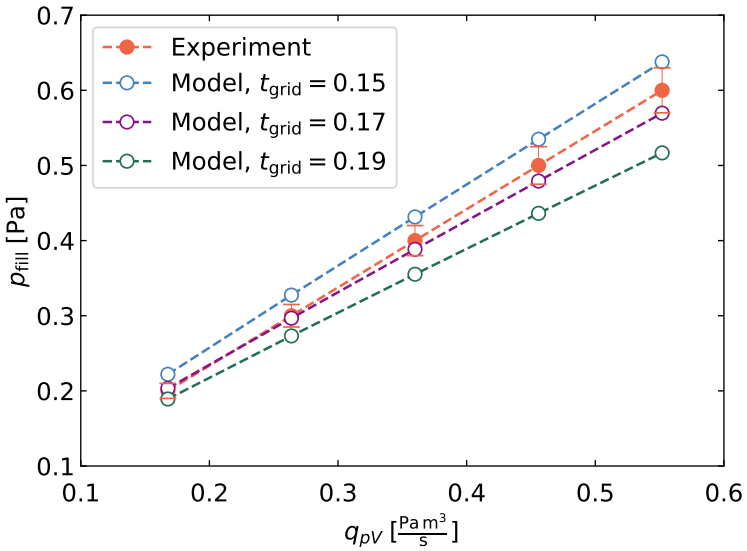

Figure 4.5: *Experimentally obtained gas flow calibration curve (full symbols) and numerically obtained ones (open symbols) for three different plasma grid transparencies t_{grid}. The filling pressure p_{fill} is plotted over the pV-throughput q_{pV} to find the $t_{\mathrm{grid}} = 0.17$, that matches best with the experimental situation (in particular at 0.3 Pa).*

volume averages of $p_{\mathrm{m}} = n_{\mathrm{m}} k_{\mathrm{B}} T_{\mathrm{m}}$, where a uniform $T_{\mathrm{m}} = 300\,\mathrm{K}$ is used. As can be seen in figure 4.5, using $t_{\mathrm{grid}} = 0.17$ fits the experimental data best at the most relevant pressure of 0.3 Pa. Furthermore, all modeled filling pressures are within the experimental error bars. Therefore $t_{\mathrm{grid}} = 0.17$ is used in all simulations in this work. In this way the correct relation between the influx and the filling pressure is maintained as long as the geometry of the inlet and plasma grid do not change. This is the case for all simulations considered in this work.

The calculated pressure profile resulting from the experimentally measured inlet flux at $t_{\mathrm{grid}} = 0.17$ is almost uniform throughout the whole ion source, as shown in figure 4.6. Except for the inlet and outlet regions, where the pressure is increased

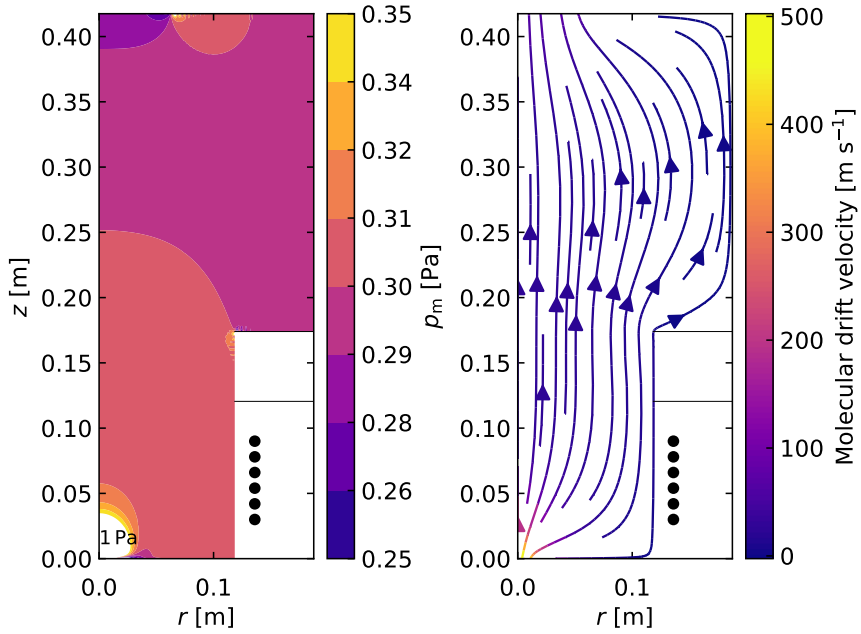

Figure 4.6: *Calculated spatial profile of the almost uniform filling pressure* $p_\mathrm{m} = n_\mathrm{m} k_\mathrm{B} T_\mathrm{m}$ *(left plot) and streamline plot of the molecular drift velocity* $\boldsymbol{u}_m$ *(right plot). The plots are at the experimentally measured inlet flux that corresponds to a filling pressure of 0.3 Pa. The plasma grid transparency* t_grid *is set to* 0.17.

to values of around 1 Pa directly at the inlet (not shown) and reduced to 0.28 Pa in front of the plasma grid. In these regions the molecular drift velocity reaches values well above 200 m s^{-1}, whereas in the bulk of the ion source typical speeds are much lower than 50 m s^{-1}.

4.4 RF power coupling validation

The BUG ion source is typically operated in the 'high magnetic RF field region' of the local skin effect regime, which is situated above the nonlinear regime, as shown in figure 2.3. This suggests that the skin effect should be local. However, the operating points are also close to the nonlinear regime, wherefore both regimes are investigated. As a further comparison, the anomalous regime is also modeled. Figure 4.7 shows the RF coil current amplitude I_0 and the electron density ratio $n_\mathrm{e,s}/n_\mathrm{e,c}$ (see figure 4.1 for the local positions of the electron density in the RF

sheath and in the driver center) at 0.3 Pa for various generator powers. Plotted

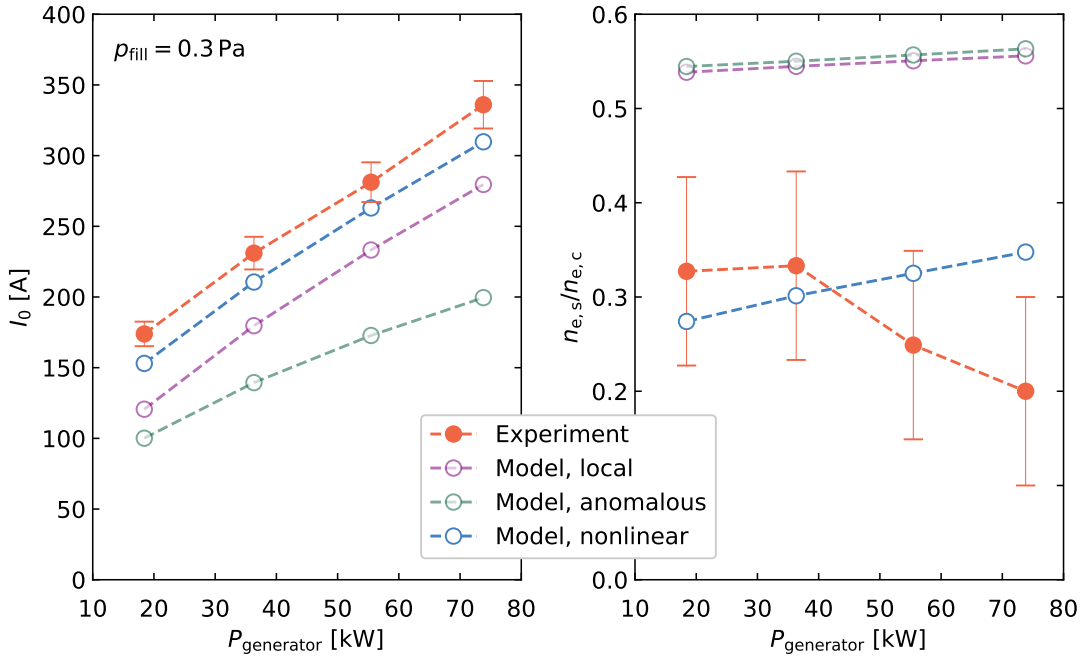

Figure 4.7: *Experimentally obtained (full symbols) RF coil current I_0 and electron density ratio $n_{e,s}/n_{e,c}$ for a fixed $p_{fill} = 0.3$ Pa at various generator powers. Plotted along are model results (open symbols) with different assumptions about the RF power coupling regime.*

are the experimental results (full symbols), where I_0 increases almost linearly with increasing generator power and $n_{e,s}/n_{e,c}$ slightly decreases from around 0.3 at 20 kW to 0.2 at 70 kW. Plotted along are the model results, where different approximations regarding the RF skin effect regime are made, as explained in section 3.5.5.

- *Local regime:* This is the most simple approximation of the electron momentum transport equation (3.62) that results in Ohm's law (3.68). The RF Lorentz force is neglected in all components of the electron momentum transport equation in this approximation. The resulting RF coil current amplitudes scale linearly with power, as in the experiment. However, they are systematically too small, as shown in the left plot of figure 4.7, denoted as 'model, local'. The neglect of the RF Lorentz force in equation (3.61) yields that the ratio of the electron densities is systematically too large, as shown

in the right plot of figure 4.7. These results indicate that using the local approach to simulate the RF power coupling in the BUG ion source is an oversimplification that is not valid.

- *Anomalous regime without RF Lorentz force:* In this approximation the Lorentz force is neglected but the divergence of the stress tensor is retained in equation (3.62). For the viscosity the non-local expression given by equation (3.70) is used. The resulting values for I_0 and $n_{\mathrm{e,s}}/n_{\mathrm{e,c}}$ are even further away from the experimentally obtained values than the values obtained in the local approximation. This is so because the diffusion introduced by the viscosity extends the region of power absorption further radially inwards beyond the collisional RF sheath, wherefore a lower RF coil current is needed.

- *Anomalous regime with RF Lorentz force:* Here all components of the RF Lorentz force, as given in equations (3.60) and (3.63), and the viscosity in its non-local formulation according to equation (3.70) are retained. In this approximation the RF-averaged component of the Lorentz force strongly compresses the plasma, wherefore no steady state solution is obtained. The same result was also obtained by Hagelaar et al. [22]. The compression effect is even more pronounced when no viscosity is retained.

- *Nonlinear regime:* Here all components of the RF Lorentz force, as given in equations (3.60) and (3.63) and the viscosity in its local formulation, as given in equation (3.71) are retained. The resulting values are denoted as 'model, nonlinear'. The RF coil currents scale as in the experiment and are almost within the experimental error bars for all powers. Also the modeled electron density ratio is within the experimental error bars for all powers, except for the highest power, where it is slightly too large.

As shown in figure 4.7, using the RF Lorentz force together with the viscosity in its local formulation yields results that are in closest agreement with the experiment, compared to all other approximations. The underlying physical mechanism of the RF power coupling is hereby an interplay between the RF-averaged Lorentz force that compresses the plasma and the viscosity that considerably increases the radially inward diffusion of the current density $\tilde{J}_{\mathrm{RF},\varphi}$ and thus counteracts the

compression. The diffusion of the RF current is shown in figure 4.8, where in the left plot the RF Lorentz force as well as the diffusion are active ('model, nonlinear'), whereas both effects are switched off in the right plot ('model, local'). These

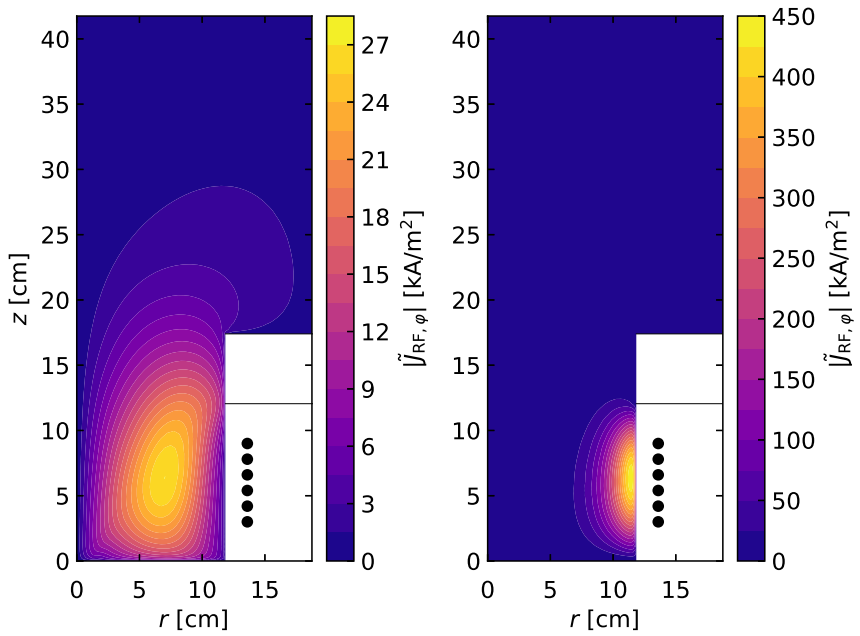

Figure 4.8: *Calculated absolute value of the RF current density* $|\tilde{J}_{\mathrm{RF},\varphi}|$ *at* $P_{\mathrm{generator}} = 60\,\mathrm{kW}$ *and* $p_{\mathrm{fill}} = 0.3\,\mathrm{Pa}$. *Values in the left plot are obtained using the nonlinear regime approximation, whereas values in the right plot are obtained using the local regime approximation.*

results indicate that the use of the local collisional viscosity $\eta_{\mathrm{e,visc}}$ is appropriate for the 'high magnetic RF field region' of the local regime. In contrast to that, the diffusion that is associated with the anomalous regime $\eta_{\mathrm{e,stoc}}$ does not counteract enough the compression, since it is too small by roughly one order of magnitude, i.e. $\eta_{\mathrm{e,stoc}} \approx 0.1\eta_{\mathrm{e,visc}}$. This is consistent, since $\eta_{\mathrm{e,stoc}}$ is valid only in the anomalous regime. Hence no steady state is obtained, if $\eta_{\mathrm{e,stoc}}$ is used instead of $\eta_{\mathrm{e,visc}}$.

To summarize: by using the various different approximations of the electron momentum balance it is revealed that the usual collisional or anomalous descriptions (that are appropriate for describing more standard ICP that are operated at higher applied frequencies and lower RF powers and thus considerably lower magnetic RF fields) result in RF coil current amplitudes that are far away from the experimentally

obtained values. The same is true for the ratio of the plasma densities. Instead it is shown in this work, that by retaining the RF Lorentz force combined with the electron viscosity in its local formulation a good match between the experimentally obtained RF coil currents as well as of the plasma density ratio is obtained. In this way it is possible for the first time to quantitatively describe the self-consistent RF power coupling in the regime of low filling pressures of around 0.3 Pa, a low driving frequency of 1 MHz and at high powers around 60 kW.

4.5 Impact of the neutrals

The plasma and neutral particles are strongly coupled via elastic and inelastic collisions in the discharge volume. At low pressures, also processes at the walls, where ions recombine according to the probabilities given in table 3.3 are highly important. Because of this strong coupling, the electron density and thus the RF current amplitude I_0 and also the RF power transfer efficiency η are sensitive on the spatial profiles of the neutrals, wherefore their description has to be as realistic as possible. This excludes the approach of assuming a constant neutrals background, which is usually followed [99, 114]. For typical ion source operational parameters the mean free paths of the neutrals are calculated using equation (2.12), resulting in around 10 cm and 30 cm for the molecules and atoms, respectively. I.e. both mean free paths are comparable to the discharge size. To investigate the kinetic effects associated with these long mean free paths, a direct simulation Monte Carlo (DSMC) method is used in [35] for the neutrals. However, as is shown in [35], the effort to implement, verify and validate the DSMC method is huge. Also the run-time of the resulting hybrid code (i.e. kinetic neutrals and fluid charged particles) increases considerably compared to a fluid model, that typically runs for a few hours rather than several days, that might be necessary for a hybrid code. For these two reasons, the RF power coupling model at the present state foregoes a kinetic description of the neutrals. Nevertheless, the results from the DSMC model can at least partly be incorporated in the fluid model to demonstrate the impact on the plasma behavior. This approach is described in the following.

The energy distribution functions of the neutrals resulting from the DSMC simulations are non-Maxwellian with a pronounced high energy tail, as indicated

in figure 4.9 for the atoms in front of the wall at a filling pressure of 0.3 Pa and an absorbed plasma power of 60 kW. The high energy tail has two origins.

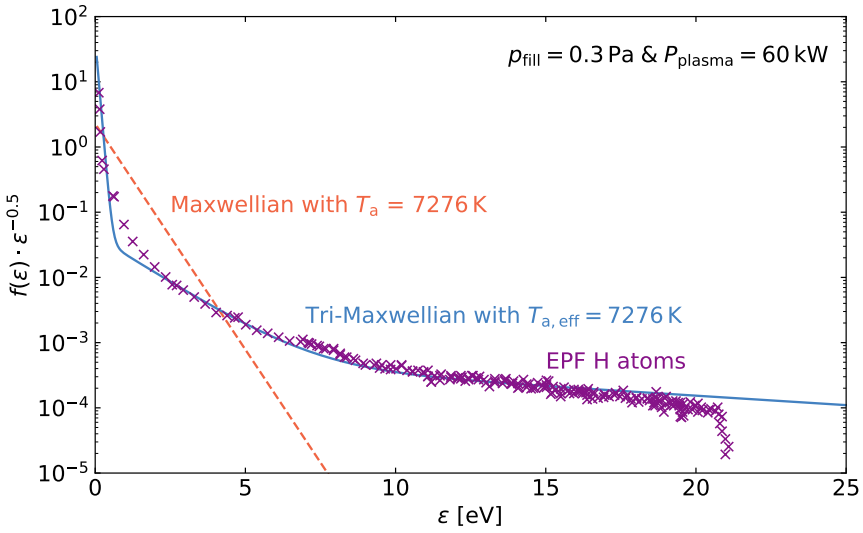

Figure 4.9: *The atomic energy probability function (EPF) in front of the wall at* $p_{fill} = 0.3\,Pa$ *and* $P_{plasma} = 60\,kW$ *resulting from DSMC simulations of the ion source [35] shows a pronounced high energy tail. Depicted are also a Tri-Maxwellian fit as well as a Maxwellian EPF at the same mean energy. Figure adapted from [35].*

Firstly, hydrogen atoms are created in the discharge volume by dissociation of hydrogen molecules. Hereby, each newly created atom obtains 3.7 eV, which is half of the dissociation threshold energy 7.4 eV [73]. Secondly, atoms are created at the discharge walls by recombination of ions. The total energy of these ions is mainly determined by the plasma sheath potential, which is around 50 V. The probabilities for this recombination and the amount of energy that is transferred to the neutrals are specified in table 3.3. Note that because of the infrequent collisions at low pressure the atomic distribution function looks similar throughout the whole discharge [35].

In the neutrals module, a Maxwellian distribution function is assumed for calculating the particle and energy boundary fluxes of the neutrals, as described in section 3.4.2. For the atoms, using a Maxwellian instead of a non-Maxwellian energy distribution function with the same mean energy (cf. figure 4.9) has two effects [35]:

1. The effective velocity towards the wall $u_{\mathrm{a,eff}}$, as obtained from equation (3.38), is overestimated yielding a too low atomic density in the whole discharge volume.

2. The heat flux towards the walls obtained from equation (3.41) is underestimated. This too low heat loss yields a too high atomic temperature in the whole discharge volume.

Both effects lead to an overestimation of neutral depletion when a Maxwellian boundary flux is assumed for the atoms.

To account for these effects and thus describe neutral depletion in a quantitatively correct way, the effective velocity as well as the heat flux in the neutrals module are adjusted in the following manner. At first, the energy probability function (EPF) obtained in [35] is fitted by a Tri-Maxwellian distribution function to account for the pronounced high energy tail, as shown in figure 4.9. Using a Tri-Maxwellian has the advantage, that analytical expressions are obtained for the effective velocity and heat flux that are calculated by using the defining equations (3.38) and (3.41). The resulting effective velocities and heat fluxes are shown in figure 4.10 (a) and (b), respectively. Depending on the drift velocity towards the wall $u_{\mathrm{a},\perp}$, the Maxwellian result for $u_{\mathrm{a,eff}}$ has to be damped by a factor $s_{u_{\mathrm{a,eff}}} \in [0.5, 0.65]$, as shown in figure 4.10 (c) whereas the Maxwellian atomic energy flux has to be amplified by a factor $s_{n_{\mathrm{a}} u_{\mathrm{a,eff}} U_{\mathrm{a}}} \in [3.5, 4.5]$, as shown in figure 4.10 (d). Typical atomic drift velocities directly in front of the walls point outwards with $u_{\mathrm{a},\perp} \approx +500\,\mathrm{m/s}$.

The same correction is applied to the molecular boundary fluxes resulting in damping and amplification factors of $s_{u_{\mathrm{m,eff}}} \in [0.9, 1]$ and $s_{n_{\mathrm{m}} u_{\mathrm{m,eff}} U_{\mathrm{m}}} \in [1, 2]$, respectively. Thus the effect of a non-Maxwellian energy distribution function is by far not as pronounced for the molecules as for the atoms. However, it is also not negligible, wherefore the correction factors are applied to the boundary fluxes of the molecules as well.

The flux scaling based on the atomic and molecular distribution functions calculated by the DSMC code for $p_{\mathrm{fill}} = 0.3\,\mathrm{Pa}$ and $P_{\mathrm{plasma}} = 60\,\mathrm{kW}$ is only valid in exactly these conditions, which are the only ones that are published [35]. The impact on the RF power transfer efficiency is quantified exemplarily at these conditions. The resulting η is 0.65, when the non-Maxwellian shape of the distribution function

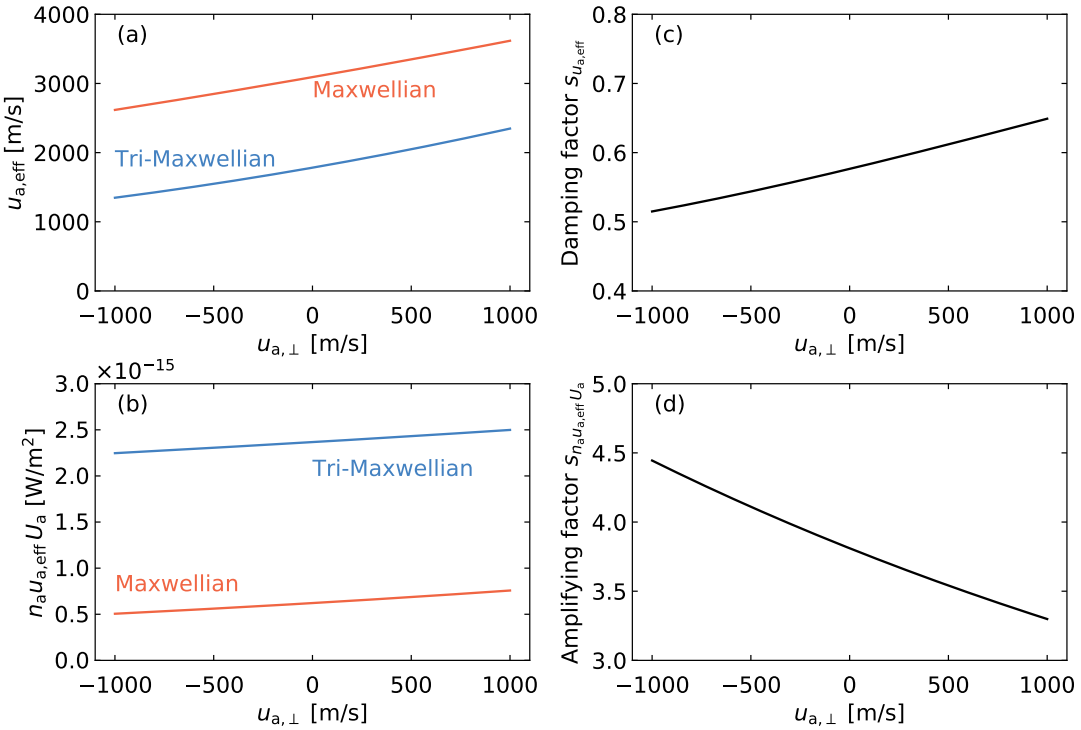

Figure 4.10: *Effective forward velocity $u_{a,eff}$ (a) and energy flux $n_a u_{a,eff} U_a$ (b) towards the walls for Maxwellian and Tri-Maxwellian distribution functions of the atoms plotted over the drift velocity at the walls $u_{a,\perp}$. Plots (c) and (d) depict the resulting damping of the Maxwellian $u_{a,eff}$ and amplification of the Maxwellian $n_a u_{a,eff} U_a$, respectively.*

is considered, whereas it is 0.53 when no flux correction is applied. This means that η is increased by around 0.12 (mostly) due to the higher atomic density resulting from the non-Maxwellian boundary fluxes. Assuming the numbers for the flux scaling from above introduces an error, when e.g. the power or presumably even more important the pressure are changed. From a physical point of view, one would expect that for lower pressures the above explained effect should be even more pronounced, because there are even less collisions that could drive the distribution functions back to a Maxwellian one. At the same time, a lower pressure goes along with a higher electron temperature and plasma potential, wherefore the ions that impinge on the walls and recombine have even larger energies. Due to the lack of self-consistent neutrals distribution functions at various operation conditions, the flux scaling as shown in figure 4.10 is used for $p_{fill} \leq 0.3$, whereas no flux correction

is applied for $p_{\mathrm{fill}} > 0.3$. With this approach, it is possible to include kinetic effects of the neutrals in a qualitative way in the fluid equations.

4.6 Impact of the hydrogen isotope

The ITER NNBI heating and current drive systems will be operated in hydrogen and in deuterium [3]. Regarding the RF power coupling, it is experimentally demonstrated at the ITER RF prototype ion source, that using deuterium instead of hydrogen leads to values of η, which are increased by around 0.05 in all measured trends [24]. This systematic increase can be reproduced with the model by simply doubling the ion masses in the deuterium case. The underlying effect is a decrease in plasma losses because of a smaller Bohm velocity (see equation (2.19)), wherefore the electron density in the RF sheath is increased. The RF power coupling improves in this case, because more electrons are heated. These first results indicate that the increased mass in essence explains the isotope effect on the RF power coupling. However, to investigate the isotope effect in more detail, also all (in-)elastic collisional processes in the volume and at the walls have to be exchanged in the model. The issue here is that data for deuterium is not as readily available as for hydrogen. It is left for future studies to quantify how this additional effect influences the RF power coupling.

4.7 Impact of the magnetic cusp field

The idea of the magnetic cusp field created by permanent magnets in the driver back plate is to produce a magnetic field that reduces the plasma particle losses onto the Faraday screen back plate and in this way increases the plasma confinement in the driver. At the same time it is crucial that the cusp field does not interfere with the inductive heating mechanism that takes place in the RF heating zone, which is axially only 5 cm away from the Faraday screen back plate. Hence, the arrangement of the 28 permanent magnets that are located within the driver back plate is chosen in a way that the produced axial field decay is as large as possible. This arrangement is shown in figure 4.11. The polarity of the magnets depicted in

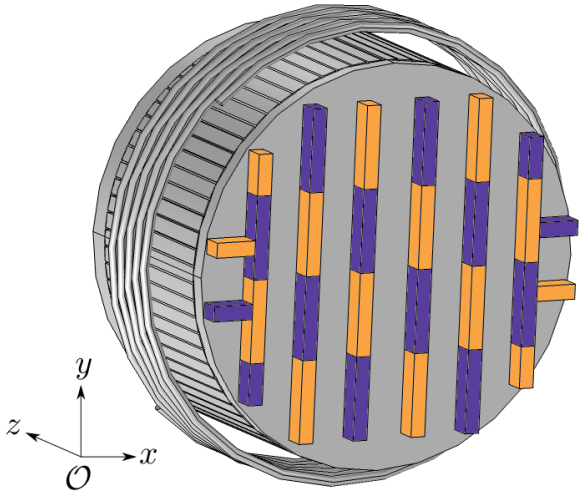

Figure 4.11: *Schematic view of the 28 cusp magnets located within the driver backplate. The magnets are right behind the the Faraday screen back plate, as shown in figure 4.1. Magnets depicted in purple are magnetized along the positive axial z direction, whereas magnets depicted in orange are magnetized in negative z direction.*

purple is along the axial z direction, whereas the polarity of the magnets depicted in orange is in negative axial z direction. The magnetostatic cusp field $\boldsymbol{B}_{\text{cusp}}$ resulting from this configuration is calculated with the AC/DC magnetostatics module of COMSOL Multiphysics® for a full 3D geometry of the ion source, which was implemented during a master thesis [102]. A code to code benchmark with a previously validated magnetostatic code [115] was successfully performed using the geometry of the permanent magnets as depicted in figure 4.11. The absolute value B_{cusp} for this configuration at different axial positions is shown in figure 4.12. Note that $\boldsymbol{B}_{\text{cusp}}$ is mainly directed in the xy-plane, i.e. $B_{\text{cusp}} \approx (B^2_{\text{cusp},x} + B^2_{\text{cusp},y})^{1/2}$. The location $z = 0\,\text{cm}$ is directly at the inside of the Faraday screen back plate and $z = 3, 4$ and $5\,\text{cm}$ are roughly in the planes of the first three coil windings of the RF coil as seen from the driver back plate. Axially, B_{cusp} decreases sharply into the driver with a maximum value of around 840 G directly at the inside of the Faraday screen back plate. In the plane of the central coil winding ($z = 5\,\text{cm}$), B_{cusp} is reduced to a maximum value of 9 G, i.e. almost by two orders of magnitude. However, from the estimation in section 2.2 follows, that the electrons in the RF heating zone are still fully magnetized by the cusp field.

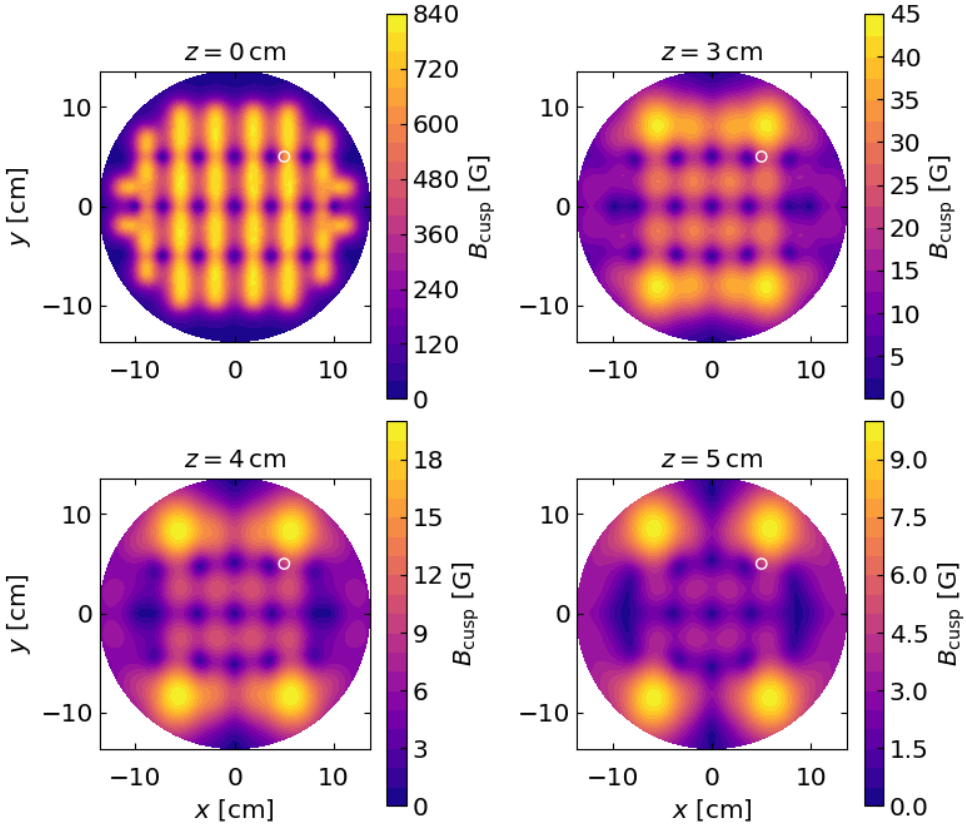

Figure 4.12: *Magnetic field produced by the cusp magnets in the driver back plate at different axial positions in the driver, measured from the Faraday screen back plate, where $z = 0$. The first three coil windings as seen from the back plate are at $z = 3, 4$ and 5 cm. These results are obtained with a 3D implementation of the ion source geometry using the magnetostatics module of COMSOL Multiphysics®. The white circles indicate a representative position used to simplify the field.*

The complex 3D topology of $\boldsymbol{B}_{\text{cusp}}$ is not cylindrically symmetric, wherefore it cannot be used in the cylindrically symmetric implementation of the model. However, to study the effect of an axially sharply decreasing cusp field on the RF power coupling in the model, an analytic fit of the 3D cusp field along an axial line-of-sight at a representative $x = y = 5\,\text{cm}$ is performed, as shown in figure 4.13.

The analytic fit is directed along the $\boldsymbol{e}_r$ direction and decreases in the z direction, wherefore it follows from equation (3.76) that the drifts are exclusively in the φ direction. Hence these drifts do not affect the transport of particles and energy,

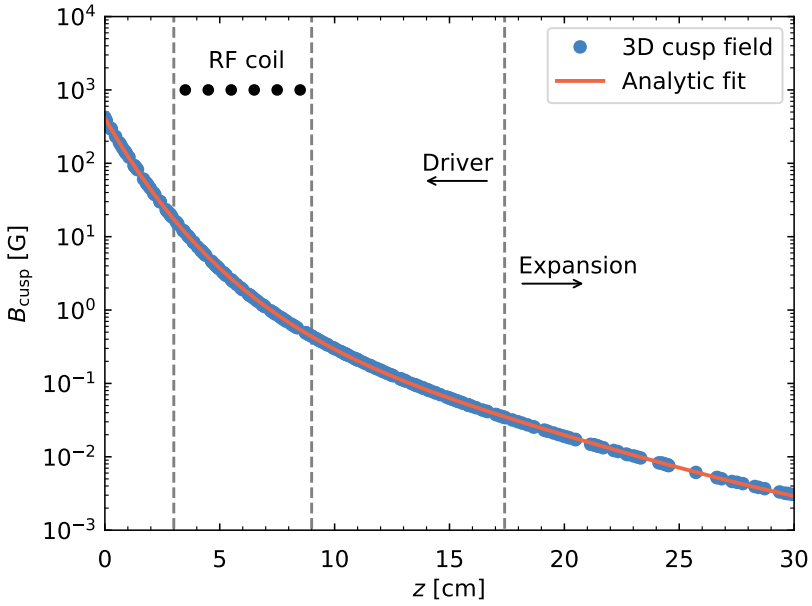

Figure 4.13: *Comparison of the axial decay of the 3D cusp field obtained at the representative position* $x = y = 5\,\mathrm{cm}$ *with its analytic fit.*

which is in the r and z direction. However, in the case of a complex 3D cusp field as shown in figure 4.12 the drifts might affect the fluxes beyond what can be modeled in the cylindrically symmetric model. Another important point that cannot be considered quantitatively is anomalous transport [116] - excited by various plasma instabilities [117] - that increases the total transport across the magnetic field lines and thus weakens the transport barrier, especially in a fully cylindrically symmetric discharge [118]. The numerical effort for a 3D simulation domain is considerably increased and the anomalous transport is very complex and not fully understood yet, wherefore it is left for future work to study how the drifts and anomalous transport quantitatively impact on the RF power coupling.

With the first approach taken in this work it is possible to qualitatively study the impact of the axial transport barrier on the electron particle and heat flux and thus on the RF power coupling mechanism. For this investigation the filling pressure and the RF generator output power are fixed at 0.3 Pa and 60 kW, respectively. Figure 4.14 shows a comparison of the electron density (upper row) and the absorbed

power (lower row), calculated according to equation (3.72), when the cusp field is neglected (left column) and when it is taken into account (right column). As expected, the cusp field creates a transport barrier for the axial electron flux, i.e. the electron flux onto the Faraday screen back plate is decreased by roughly one order of magnitude, whereas the flux onto the radial wall remains almost constant. Hence in the vicinity of the Faraday screen back plate the electrons are depleted. Consequently, the RF power coupling in this region is also strongly decreased, as is evident from a comparison of the two plots of the absorbed power in the second row of figure 4.14. This results in an increased RF coil current and a decreased η when the cusp field is considered.

The increase of the RF coil current systematically shifts all modeled RF coil currents in figure 4.7 in the right direction, i.e. to larger values. However, the axial transport barrier that builds up when using this first approach overestimates the one in the experiment, presumably because of the missing drifts and anomalous transport: at 0.3 Pa and 60 kW generator power for instance, the calculated RF coil current of $I_0 \approx 353\,\mathrm{A}$ is too large and the RF power transfer efficiency of $\eta \approx 0.33$ too small compared with the experimental values of $I_0 = 281\,\mathrm{A}$ and $\eta = 0.57$.

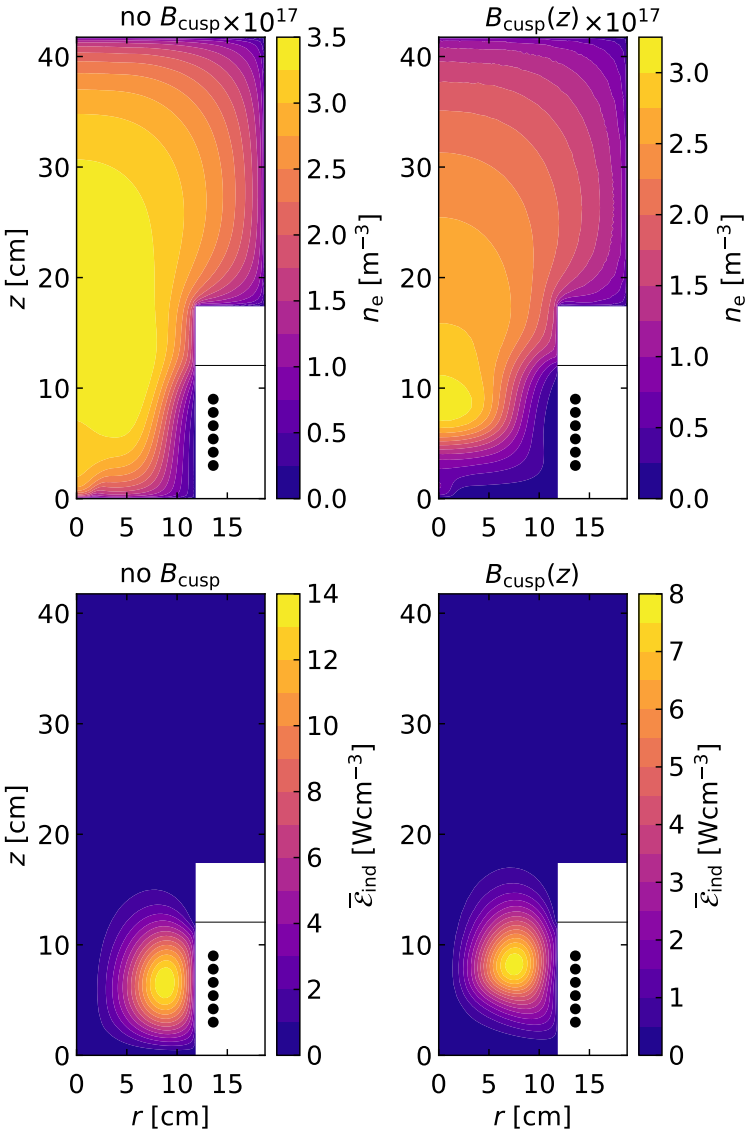

Figure 4.14: *Impact of the cusp magnetic field on electron density (upper row) and absorbed power (lower row) at* $p_{\mathrm{fill}} = 0.3\,\mathrm{Pa}$ *and* $P_{\mathrm{generator}} = 60\,\mathrm{kW}$*. In the left column no cusp field is taken into account, whereas in the right column the analytic approximation of* $\boldsymbol{B}_{\mathrm{cusp}}$*, as shown in figure 4.13, is used.*

4.8 Plasma module validation

Figure 4.15 shows the calculated plasma parameters electron density n_e, electron temperature T_e and plasma potential ϕ_{plasma} for the case of $p_{fill} = 0.3\,Pa$ and $P_{generator} = 60\,kW$. The results shown do not take any magnetostatic field into account. The electron density shows a broad maximum region with a maximum

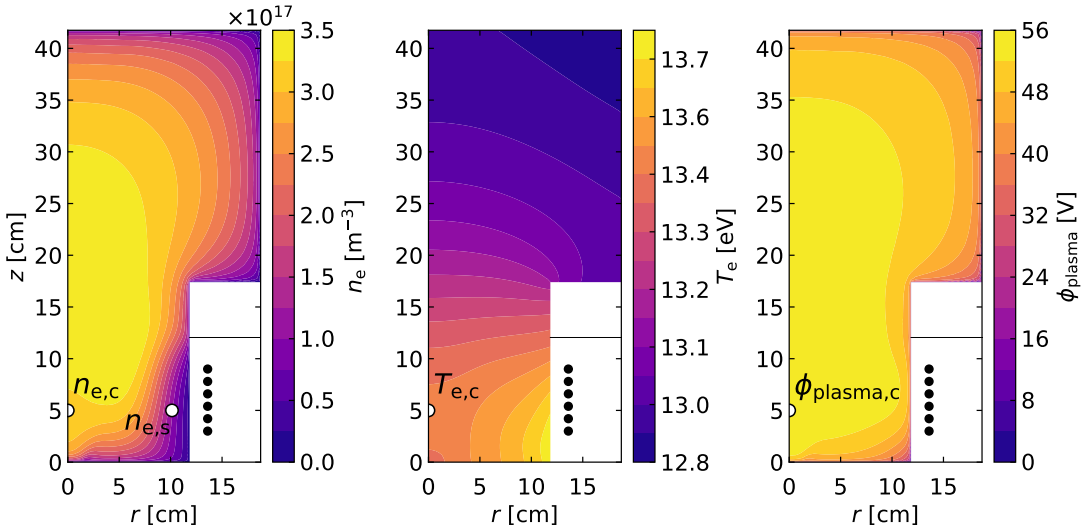

Figure 4.15: *Calculated plasma parameters n_e, T_e and ϕ_{plasma} at $p_{fill} = 0.3\,Pa$ and $P_{generator} = 60\,kW$. Circle markers indicate the locations of the Langmuir probe measurements that serve for a comparison with the modeled values.*

value of $3.5 \cdot 10^{17}\,m^{-3}$ that is centered around the transition between the driver and the expansion region. Pronounced gradients exist in front of the axial and radial driver walls. The electron temperature profile is rather flat at around 13 eV and decreases only slightly from the driver, where the heating takes place, to the expansion region. A flat plasma potential of around 56 V is present throughout a considerable part of the driver and extends deep into the expansion region. Especially towards the radial driver wall the plasma potential decreases steeply. The circles mark the positions in the driver where the Langmuir probes are located for the comparison of the calculated plasma parameters with the ones obtained from the experimental measurements (see also figure 4.1 for the measurement positions of the Langmuir probes). As explained in section 4.2.3, due to the large magnetic

RF field, it is not possible to obtain the values of $T_{e,s}$ and $\phi_{plasma,s}$ in the RF sheath experimentally.

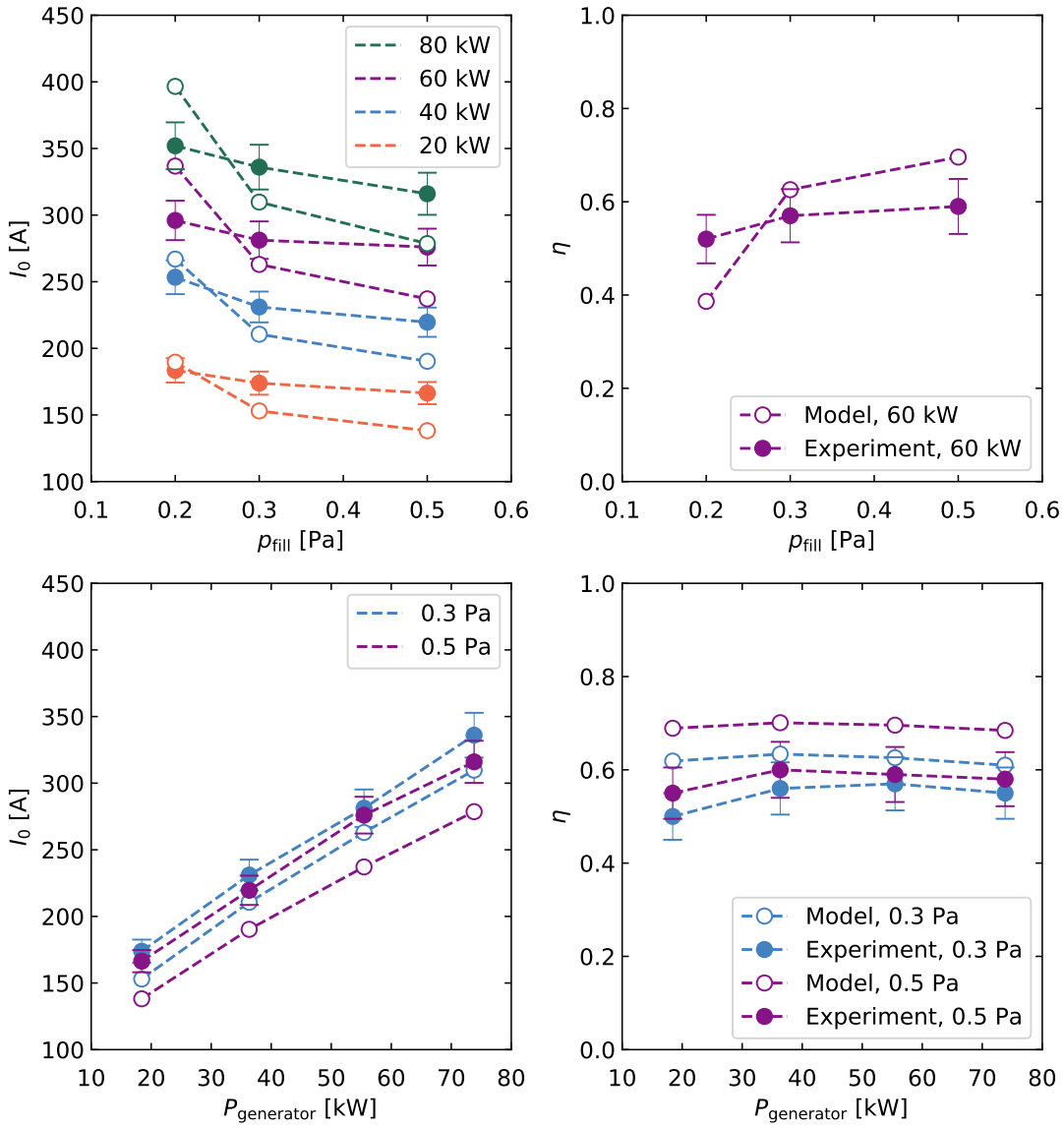

Figure 4.16: *Comparison of the electrical parameters obtained from measurements at the BUG ion source (full symbols) and from the model (open symbols). Left column: RF coil current amplitude I_0 as a function of the filling pressure (upper left plot) and as a function of the generator power (lower left plot). Right column: the corresponding RF power transfer efficiencies η.*

Figure 4.16 shows the electrical parameters RF coil current amplitude I_0 in the left column and RF power transfer efficiency η in the right column. Plotted along with the experimentally obtained values (full symbols) are the corresponding values obtained from the model (open symbols). In the upper row plots on the abscissa the filling pressure p_{fill} is varied, whereas in the lower row plots on the abscissa the generator power is varied.

The RF coil current amplitude I_0 shows the same trend in the experiment and in the model: with increasing filling pressure I_0 decreases, whereas I_0 increases almost linearly with increasing generator power. The former trend is resembled in the upper right plot (exemplarily shown for $P_{\mathrm{generator}} = 60\,\mathrm{kW}$), where the values for η obtained from experiment and model increase with increasing p_{fill}. The linearly increasing RF coil current with RF generator power corresponds to a flat RF power transfer efficiency η, as shown in the lower right plot.

Considering $p_{\mathrm{fill}} = 0.3\,\mathrm{Pa}$ and $P_{\mathrm{generator}} = 80\,\mathrm{kW}$ in the upper left plot, the modeled I_0 is almost within the experimental error bars and when the pressure is increased the numerical and experimental trends agree quite well. This is also the case for the other power levels. However, when p_{fill} decreases the increase in the modeled I_0 is systematically too steep, when compared to the one in the experiment. This too steep increase is caused by the correction of the boundary fluxes that is done to account for the neutral depletion, which is best at $p_{\mathrm{fill}} = 0.3\,\mathrm{Pa}$, where the distribution function is known from the DSMC code. Hence the resulting flux correction yields results that are closest to the experimentally obtained values. As explained in section 4.5, the flux correction should be even more pronounced at lower pressures, wherefore the modeled RF currents at 0.2 Pa are systematically too large.

Figure 4.17 shows the central plasma potential $\phi_{\mathrm{plasma,c}}$ and electron temperature $T_{\mathrm{e,c}}$. Plotted are the values obtained from Langmuir probe measurements (full symbols) and the corresponding values calculated with the model (open symbols) over the pressure for the two different generator powers 20 and 60 kW. All curves behave systematically also for 40 kW and 80 kW (not shown). The modeled plasma potential and electron temperature show the same trend as their experimentally obtained counterparts: they increase with decreasing pressure and with increasing power. The scaling of T_{e} with pressure can be explained by a simplified particle

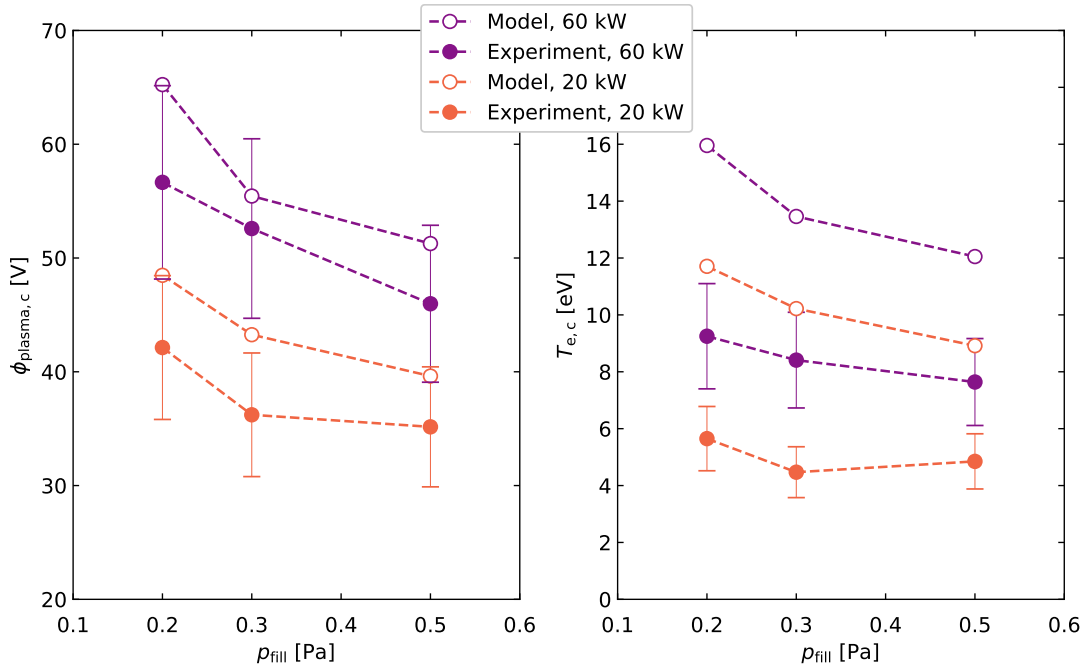

Figure 4.17: *Experimentally obtained (full symbols) and modeled (open symbols) values of the plasma potential $\phi_{\mathrm{plasma,c}}$ and the electron temperature $T_{\mathrm{e,c}}$ as a function of the filling pressure at two different generator powers of 20 and 60 kW.*

transport equation (3.46), where in steady state ($\partial_t = 0$) the ionization in the discharge volume V is balanced by the flux towards the discharge walls with the surface A, i.e.

$$\begin{aligned} &\int \mathcal{R}_{\mathrm{i}} \,\mathrm{d}V = \int \nabla \cdot n_{\mathrm{i}} \boldsymbol{u}_{\mathrm{i}} \,\mathrm{d}V = \oint n_{\mathrm{i}} \boldsymbol{u}_{\mathrm{i}} \cdot \hat{\boldsymbol{n}} \,\mathrm{d}A \\ &\Rightarrow X_{\mathrm{ioniz}}(T_{\mathrm{e}}) \varkappa_{\mathrm{e}} n_{\mathrm{n}} V = \varkappa_{\mathrm{i}} u_{\mathrm{Bohm}}(T_{\mathrm{e}}) A \\ &\Rightarrow f(T_{\mathrm{e}}) = \frac{X_{\mathrm{ioniz}}(T_{\mathrm{e}})}{u_{\mathrm{Bohm}}(T_{\mathrm{e}})} = \frac{A}{V} \frac{1}{n_{\mathrm{n}}}. \end{aligned} \tag{4.11}$$

Herein, X_{ioniz} and u_{Bohm} denote the rate coefficient for ionization and the Bohm speed, as defined in equation (2.19), respectively. Since $f(T_{\mathrm{e}})$ is a monotonically increasing function (cf. [23]), it follows that for an increasing neutral particles density $n_{\mathrm{n}} \propto p_{\mathrm{fill}}$ the electron temperature has to decrease. The model shows that neutral depletion increases with increasing power. This is evident from figure 4.19, where for a constant filling pressure the total neutral particle density decreases

with increasing power. Having this in mind equation (4.11) also explains that an increase in power yields a higher T_e.

Considering the electron momentum transport equation (3.57) in a state of dynamic equilibrium (i.e. neglecting all quantities except for the pressure gradient and the electrostatic field) results in the well known Boltzmann relation [37]. This relation states that electrons are easily pulled towards regions of higher potentials. Using the Boltzmann relation to express the electron flux in then (pre-)sheath as a function of the thermal flux at the wall and equating this flux to the ion Bohm flux ($= n_\mathrm{i} u_\mathrm{i,Bohm}$, as defined in equation (2.19)) yields a useful relation between the plasma potential and the electron temperature for a floating wall, i.e.

$$\frac{\phi_\mathrm{plasma}}{T_\mathrm{e}} = \frac{1}{2}\left(1 + \left|\ln\frac{2\pi m_\mathrm{e}}{m_\mathrm{i}}\right|\right) \approx 4. \tag{4.12}$$

Herein, the ion mass $m_\mathrm{i} \approx 1.8\, m_{\mathrm{H}^+}$ is approximated using the ratio between the three ion species as given in section 4.2.3. Relation (4.12) is well fulfilled for the values obtained with the model. However, the value of $\frac{\phi_\mathrm{plasma}}{T_\mathrm{e}}$ obtained from experimental measurements is around 6.5, i.e. even though the modeled plasma potential in the left plot of figure 4.17 is within the experimental error bars, the modeled electron temperatures are systematically too large, as shown in the right plot of figure 4.17. A possible reason for this discrepancy is the cusp field. Due to its considerable strength directly in front of the driver back plate (see figure 4.12), also the ions are magnetized there. Hence a transport barrier for the ions is created, wherefore the charged particle losses towards the axial walls are reduced. This leads to a larger plasma density and a lower electron temperature, that is needed to sustain the discharge.

Figure 4.18 shows the central electron density $n_\mathrm{e,c}$ as well as the ratio of the electron density in the RF sheath $n_\mathrm{e,s}$ to $n_\mathrm{e,c}$ as a function of the filling pressure for two different generator powers. The central electron density in the left plot of figure 4.18 shows the same trends in the model and in the experiment when either the power or the pressure are varied. These trends can be explained by a simplified power balance

$$\eta P_\mathrm{generator} = P_\mathrm{plasma} = \mathrm{e} A_\mathrm{eff} n_\mathrm{e} u_\mathrm{Bohm}(T_\mathrm{e}) \mathcal{E}_\mathrm{total}(T_\mathrm{e}), \tag{4.13}$$

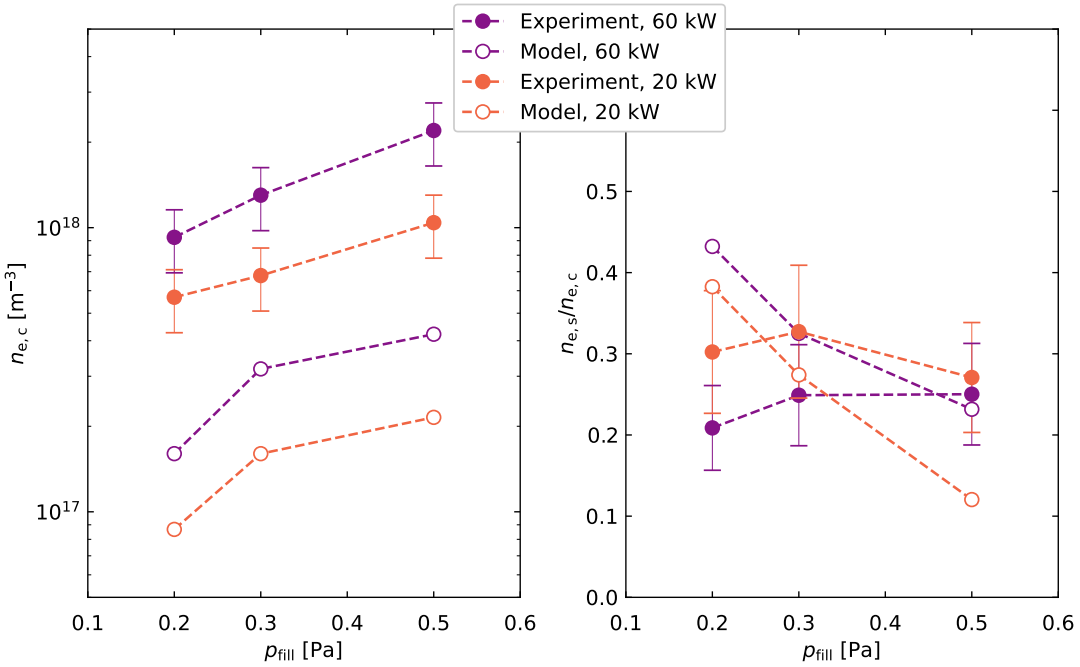

Figure 4.18: *Experimentally obtained (full symbols) and modeled (open symbols) values of the electron density $n_{e,c}$ in the center of the driver (left plot) as well as the ratio of the RF sheath to central electron density $\frac{n_{e,s}}{n_{e,c}}$ (right plot) as a function of the filling pressure at two different generator powers of 20 and 60 kW.*

where P_{plasma} is the power absorbed by the plasma as defined in equation (3.73), A_{eff} an effective surface area for charged particle losses and $\mathcal{E}_{\text{total}}$ the energy (measured in electron volts) that is lost per electron-ion pair.

When increasing the pressure at a fixed $P_{\text{generator}}$, η increases, as shown in the upper right plot of figure 4.16, and T_e decreases, as shown in the right plot of figure 4.17. Since also $u_{\text{Bohm}}(T_e)$ and $\mathcal{E}_{\text{total}}(T_e)$ decrease with increasing pressure (i.e. with decreasing T_e), it follows from equation (4.13) that n_e has to increase, when the pressure is increased.

For a fixed pressure (i.e. fixed T_e) it follows from equation (4.13) that n_e increases with increasing generator powers. This is so because the relative change in η is small compared to the corresponding change of $P_{\text{generator}}$. E.g. from 20 kW to 60 kW, $P_{\text{generator}}$ increases by a factor of three, whereas the change in η is only around 10% (cf. lower right plot of figure 4.16).

The left plot of figure 4.18 shows that the modeled values of the electron densities in the driver center and in the RF sheath (not shown) are systematically too low by a factor of roughly five, when compared to the experimental ones. This discrepancy could again be caused by the magnetic cusp field, since the ion transport barrier in front of the axial driver wall increases the plasma density in the discharge. The magnetization of the ions in the vicinity of the driver back plate has no direct effect on the RF power coupling, as the ions do almost not contribute to the plasma current. It is verified by artificially increasing the electron volume production rate, that the systematically larger n_e (and lower T_e) in the experiment do not change the trends obtained in the validation and optimization studies. Another effect that becomes relevant only at high powers and at pressures below 0.3 Pa is the bi-Maxwellian electron distribution function, which is known from Langmuir probe measurements [69]. This also tends to increase the plasma density.

The right plot of figure 4.18 shows a good agreement between the experimentally obtained and the modeled trends. Depending on the used RF power coupling mechanism the calculated values of $\frac{n_\mathrm{e,s}}{n_\mathrm{e,c}}$ deviate considerably, as shown in the right plot of figure 4.7. Against this background the absolute agreement at 0.3 Pa between experimentally obtained and modeled values can be considered very good.

The left plot of figure 4.19 shows the calculated neutral densities obtained as the sum of the volume averaged atomic and molecular densities at the three different filling pressures 0.2, 0.3 and 0.5 Pa for varying generator powers. The corresponding molecular densities before plasma ignition are $4.8 \cdot 10^{19}\,\mathrm{m}^{-3}$, $7.2 \cdot 10^{19}$ (not shown) and $1.2 \cdot 10^{20}$ (not shown), respectively. Therefore neutral depletion is present at each of the three filling pressures. The sum of the atomic density n_a and the molecular density n_m (nonlinearly) decreases even further with increasing generator power. This neutral depletion goes along with a saturating electron density $n_\mathrm{e,c}$ with power at 0.2 Pa, as shown in the right plot of figure 4.19. Here all modeled absolute values of $n_\mathrm{e,c}$ are increased by a factor of five to emphasize the coinciding experimental and modeled trends with generator power.

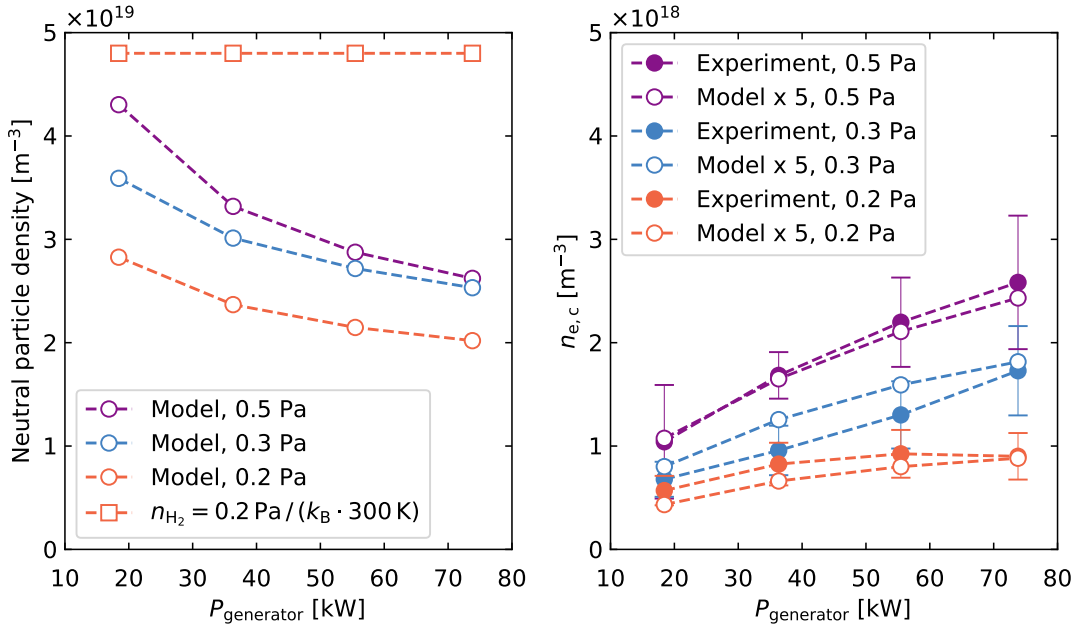

Figure 4.19: *Left plot: sum of the volume averaged atomic density n_a and molecular density n_m obtained from the model as a function of the generator power at three different filling pressures 0.2, 0.3 and 0.5 Pa, respectively. Right plot: corresponding values of the experimentally obtained and modeled electron density in the driver center, where the modeled electron densities are multiplied by a factor of five to emphasize the coinciding trends with power.*

4.9 Summary and conclusion

One of the major challenges when predicting the inductive power coupling in an RF-driven negative ion source is the low applied frequency of 1 MHz, where due to large magnetic RF fields nonlinear effects such as the RF Lorentz force dominate the spatial distribution of the plasma parameters and hence the RF power coupling. To describe this regime self-consistently, appropriate approximations for the RF Lorentz force as well as for the electron viscosity are combined in this work. Using these formulations, the plasma compression by the RF Lorentz force is mitgated by the electron viscosity. In this way self-consistent steady state solutions are obtained for the first time. Moreover, the power and pressure trends (as well as a considerable fraction of the absolute values) of the experimentally obtained electrical and plasma parameters are captured. As a comparison it is

shown that by assuming a purely collisional or anomalous regime the model results are systematically shifted away from the experimental results. For all investigated $p_{\text{fill}} \in [0.2, 0.5]\,\text{Pa}$ and $P_{\text{generator}} \in [20, 80]\,\text{kW}$ neutral depletion has an important non-beneficial impact on the RF power coupling. It is shown that by appropriate scaling of the neutrals boundary fluxes it is possible to properly account for neutral depletion in a fluid model. Furthermore, first studies using a simplified topology of the magnetostatic cusp field reveal that its presence decreases the plasma's capability to absorb RF power because it depletes the electron density in front of the radial driver walls, where the RF heating takes place.

Remaining limitations of the model are the missing 3D description and the fluid neutrals. A 3D description is needed to model the plasma drifts resulting from the cusp and filter field [21, 83], whereas a fully kinetic description of the neutrals (e.g. by a DSMC code) is capable of describing neutral depletion in great detail [35]. However, because of the increased effort for implementing and executing a model, where one or even both of these limitations are removed, systematic validation and optimization studies will hardly be possible anymore. Hence the successfully validated self-consistent fluid model will be used in the following to optimize the RF power coupling within the broad space of external parameters. Dedicated studies to investigate the drifts and kinetic neutrals in more details are left for future work.

5 Optimizing RF power coupling

In this chapter it is studied how external parameters such as various discharge and coil geometries, as well as the applied frequency impact on the RF power coupling. As explained in the introduction and in section 2.3, the external parameters do not only affect the plasma resistance R_{plasma}, but also the network resistance R_{network}. Hence for the optimization of each external parameter, R_{network} is calculated in a first step with the 3D electromagnetic model as a function of the external parameter. Following that, R_{plasma} is obtained from the 2D RF power coupling model using R_{network} from step one as an input. The RF power transfer efficiency η and the effective coil voltage $U_{\mathrm{coil,eff}}$ follow then as functions of the external parameter from equations (2.25) and (2.26), respectively. For most of the external parameters maximizing η (i.e. minimizing the RF coil current amplitude I_0) is equivalent to minimizing $U_{\mathrm{coil,eff}}$. However it follows from equation (2.26) that this is not the case for the driving frequency, wherefore here both quantities have to be assessed explicitly.

For producing a plasma with certain envisaged plasma parameters P_{plasma} is the relevant quantity [24]. Therefore in principle P_{plasma} should be fixed in all parameter optimization studies. However, it does not make a difference for all trends of η and $U_{\mathrm{coil,eff}}$ shown in this chapter whether P_{plasma} or $P_{\mathrm{generator}}$ is fixed as a model input. In the experiment $P_{\mathrm{generator}}$ is set, wherefore it is more convenient in view of a comparison to fix $P_{\mathrm{generator}}$ in the model as well. Hence this is done at a representative value of $P_{\mathrm{generator}} = 60\,\mathrm{kW}$ (and $p_{\mathrm{fill}} = 0.3\,\mathrm{Pa}$) for all investigated parameters. The only exception to that is the driving frequency, where P_{plasma} instead of $P_{\mathrm{generator}}$ is fixed to obtain more relevant absolute values of $U_{\mathrm{coil,eff}}$. Note that all trends shown in this chapter also persist for other set values of power and filling pressure.

5.1 Discharge geometry

The RF power coupling takes place exclusively in the driver region, as is evident from the power deposition profiles depicted in figure 4.14. Consequently, all geometric optimization studies in this section focus on the driver. The simulation domain with the dimensions of the expansion region as well as the driver length and radius are shown in figure 3.2. Variations of the expansion radius and length yield changes in η of less than 0.05, wherefore they are not considered further.

5.1.1 Driver length

Figure 5.1 shows the network resistance R_{network} as a function of the driver length L_{driver}. Starting from the smallest possible L_{driver} at 15 cm, R_{network} increases from

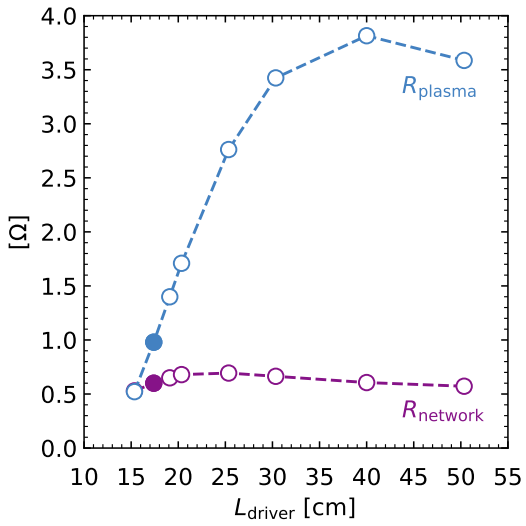

Figure 5.1: *Network resistance R_{network} as a function of the driver length L_{driver}, obtained from the 3D electromagnetic model. The full symbol indicates the validated $R_{\text{network}} = 0.6\,\Omega$ of the current BUG ion source configuration at $L_{\text{driver}} = 17.4\,\text{cm}$, as obtained from experimental measurements in section 4.2.2. Plotted along is the plasma resistance R_{plasma}, obtained from the 2D RF power coupling model, where the full symbol indicates the validated $R_{\text{plasma}} = 1\,\Omega$.*

0.53 Ω to its maximum value of 0.7 Ω at 25 cm. This increase is explained by the larger amount of eddy currents in the larger surface of a longer Faraday screen. For

a rather long Faraday screen, i.e. for L_{driver} larger than 25 cm, R_{network} decreases slightly as the distances between the outermost coil windings and the Faraday screen back plate and support ring, respectively, increase and less eddy currents are driven along these structures [102].

Plotted along is R_{plasma}, where the considerable increase for L_{driver} up to 40 cm results mainly from the larger driver volume. Figure 5.2 shows the resulting absorbed RF power for the validated $L_{\mathrm{driver}} = 17.4\,\mathrm{cm}$ compared to a simulation domain with $L_{\mathrm{driver}} = 35\,\mathrm{cm}$. Even though the spatially resolved peak value of

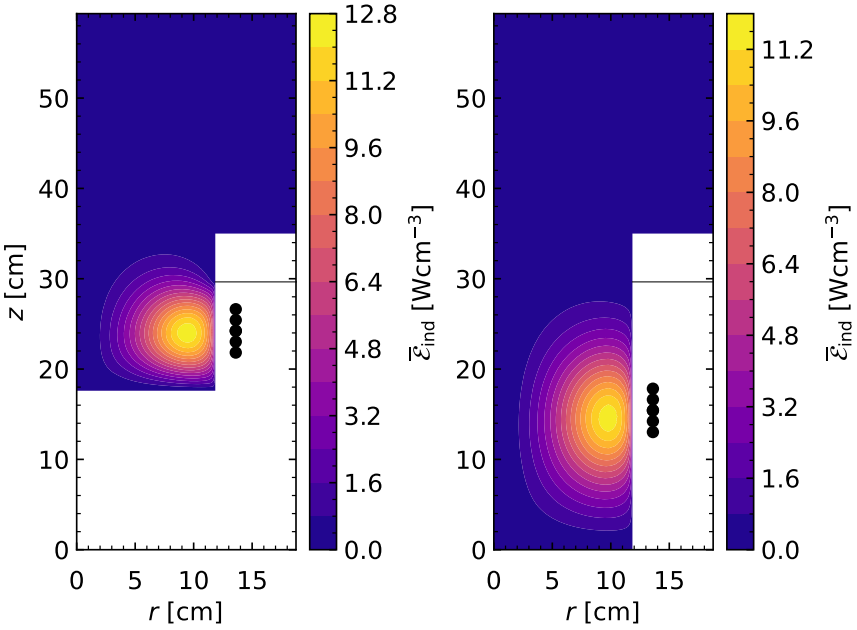

Figure 5.2: *Absorbed RF power* $\bar{\mathcal{E}}_{\mathrm{ind}}$*, as calculated from equation* (3.72)*, for the validated* $L_{\mathrm{driver}} = 17.4\,\mathrm{cm}$ *(left plot) and for a longer* $L_{\mathrm{driver}} = 35\,\mathrm{cm}$ *(right plot).*

the absorbed power is slightly lower in the case of the longer driver, the integral value P_{plasma} calculated from equation (3.73) exceeds the one of the shorter driver. For L_{driver} larger than 40 cm the axial extension of the power deposition profile does not increase any further. Also the surface area of the driver radial wall and hence the electron energy losses to the walls increase. The combination of these two effects yields that R_{plasma} decreases slightly for L_{driver} larger than 40 cm.

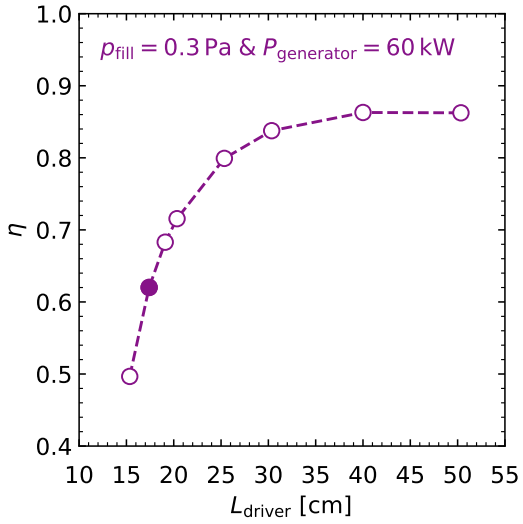

Figure 5.3: *RF power transfer efficiency η as a function of the driver length L_{driver}, obtained from the RF power coupling model. The full symbol indicates the validated $\eta = 0.63$ of the current BUG ion source configuration at $L_{\mathrm{driver}} = 17.4\,\mathrm{cm}$.*

Figure 5.3 shows the RF power transfer efficiency η as a function of L_{driver}. The resulting trend is almost entirely dominated by the large change in R_{plasma}. Quantitatively, a value of η as large as 0.85 is reachable, when L_{driver} larger than 35 cm is used.

5.1.2 Driver radius

Figure 5.4 shows the network resistance R_{network} as a function of the driver radius R_{driver}. The reason for the almost linear increase are the cylindrical surface of the Faraday screen and the coil length that both scale as $2\pi R_{\mathrm{driver}}$. The network resistance increases considerably from $0.2\,\Omega$ for the smallest possible R_{driver} to $0.9\,\Omega$, when R_{driver} is almost equal to the expansion radius.

Plotted along is R_{plasma}. The driver volume increases as $\pi R_{\mathrm{driver}}^2$, which is (as in the case of the increased L_{driver}) beneficial for the RF power coupling, because in the larger volume there are in total more electrons that are heated. However, the increase in R_{plasma} with increasing R_{driver} is not as pronounced as it is the case for the increased driver length. The main reason for this is the RF-averaged

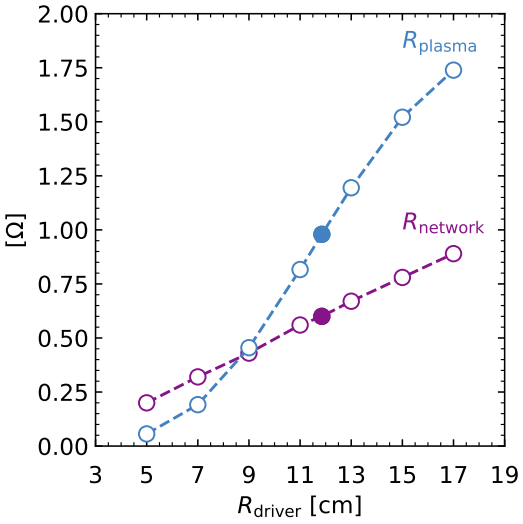

Figure 5.4: *$R_{network}$ and R_{plasma} as a function of the driver radius R_{driver}. The full symbols are the experimentally validated $R_{network} = 0.6\,\Omega$ and $R_{plasma} = 1\,\Omega$ at $R_{driver} = 11.85\,cm$.*

Lorentz force from equation (3.60), that pushes the plasma away from the RF coil radially inwards, as shown in the upper row plots of figure 5.5. For a larger driver radius of e.g. 17 cm the resulting inward pointing radial component of the RF-averaged Lorentz force is increased by a factor of $\frac{-2.4}{-1.5} \approx 1.6$. The RF-averaged Lorentz force also extends further into the plasma in radial direction. Hence the radial compression of the plasma density towards the discharge axis increases with increasing R_{driver}. As a consequence, the electron density in the vicinity of the RF coil where the RF power coupling takes place is depleted, as shown in the lower row plots of figure 5.5. Therefore the RF power coupling is affected by this more pronounced RF Lorentz force in a negative way.

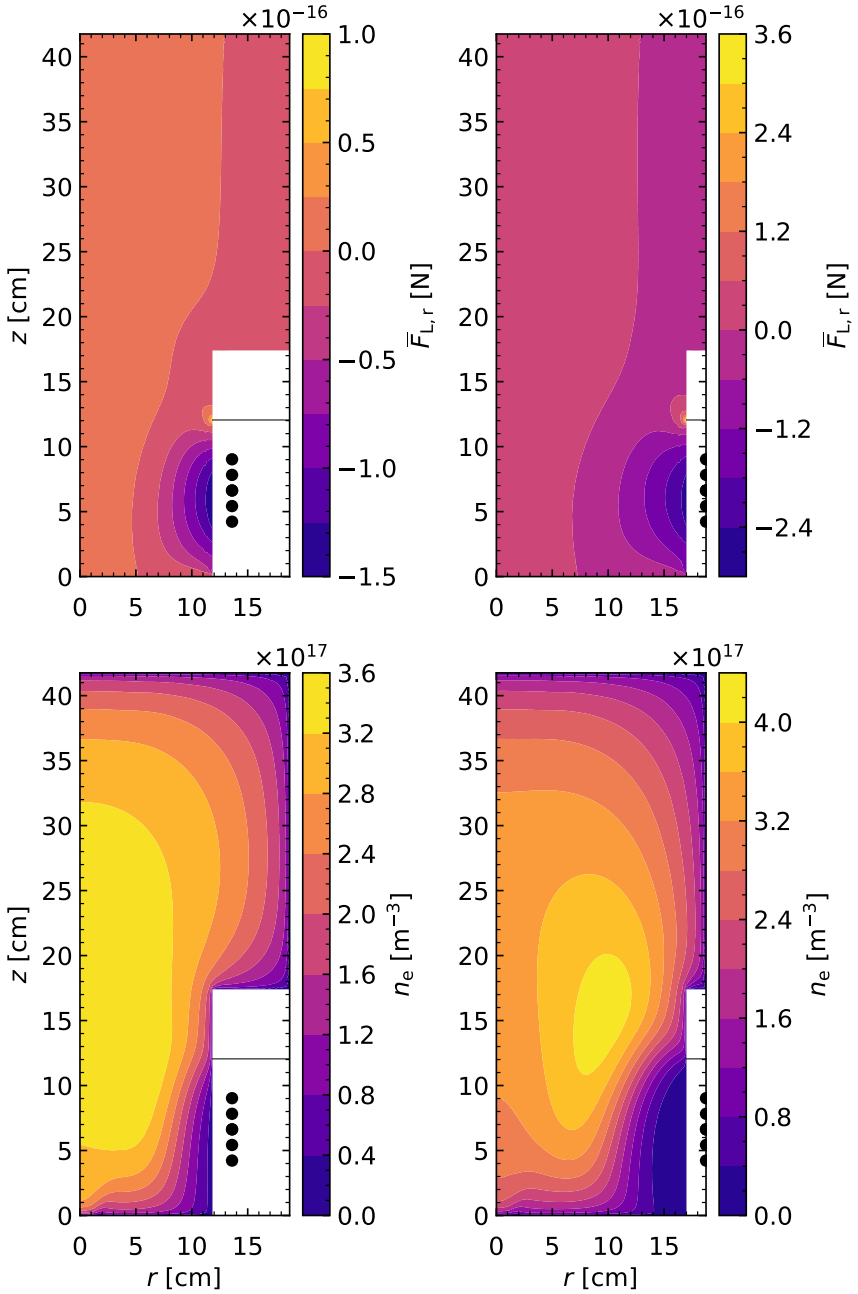

Figure 5.5: *Upper row: radial component of the RF-averaged Lorentz force for the validated* $R_{\text{driver}} = 11.85\,\text{cm}$ *(left) and for a larger* $R_{\text{driver}} = 17\,\text{cm}$ *(right). Lower row: corresponding electron density profiles.*

Figure 5.6 shows the resulting trend of η, which is not entirely determined by the change in R_{plasma}. This becomes evident from a comparison with η values obtained

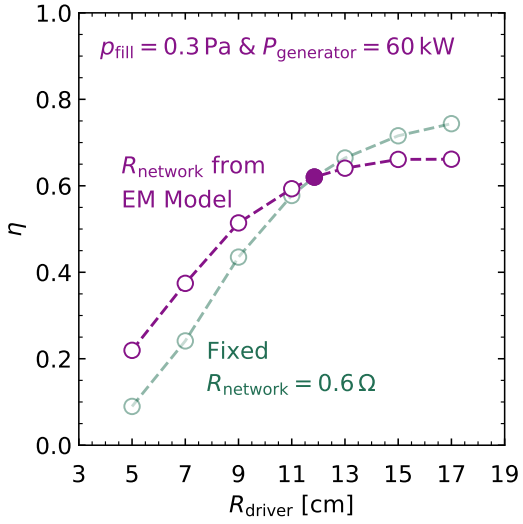

Figure 5.6: *RF power transfer efficiency η as a function of the driver radius R_{driver}. The full symbol is the experimentally validated $\eta = 0.63$ at $R_{\text{driver}} = 11.85\,\text{cm}$. Plotted along in green are the values for a fixed $R_{\text{network}} = 0.6\,\Omega$ to estimate the impact of the changing R_{network}.*

from the RF power coupling model using a fixed $R_{\text{network}} = 0.6\,\Omega$. Note that the changing R_{network} is most relevant at small and large values of R_{driver}. In summary there is almost no increase in η, when R_{driver} is increased beyond its current value.

A decrease of the Faraday screen and dielectric wall thicknesses are mimicked in the model by decreasing the radial distance between the RF coil and the radial driver wall at a fixed R_{driver} (see figure 3.2). This results in an increase in η of only 0.01 per mm reduced distance. The high power absorption in the Faraday screen requires active water cooling by internal cooling channels, wherefore its radial wall thickness of 3 mm is already minimal. The 8 mm thick dielectric has to withstand the pressure drop between ambient pressure and the low pressure inside the driver. Hence reducing the thickness of the dielectric wall will most likely lead to mechanical stability issues. When the whole driver is in vacuum, as planned for the NNBI system in the ITER experiment, it is in general possible to decrease the thickness of the dielectric wall but with a high risk at a low gain in η.

5.2 RF coil

5.2.1 Number of coil windings

Figure 5.7 shows an increasing R_{network} as a function of the number of coil windings $N_{\text{coil windings}}$. This increase is a combined effect of the longer RF coil and higher

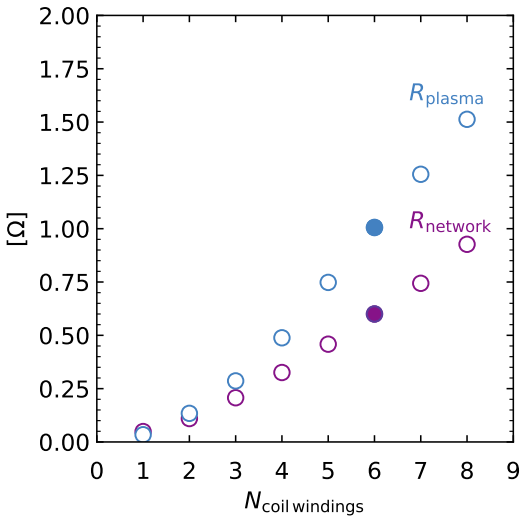

Figure 5.7: *R_{network} and R_{plasma} as a function of the number of coil windings $N_{\text{coil windings}}$. The full symbols indicate the experimentally validated $N_{\text{coil windings}} = 6$.*

eddy currents that are driven in the Faraday screen. Plotted as well is R_{plasma}, which also increases when $N_{\text{coil windings}}$ is increased due to the lower RF coil current needed to sustain the plasma.

The left plot of figure 5.8 shows the resulting η, which saturates when more than two coil windings are used. The increasing R_{network} with increasing $N_{\text{coil windings}}$ is counteracted by a decreasing RF coil current I_0. As a consequence the lost power $P_{\text{loss}} = \frac{1}{2} R_{\text{network}} I_0^2$ and thus also η remain constant. In this case the trend of η is heavily affected by the changing R_{network}, as is evident from a comparison with η values that are obtained by using a fixed $R_{\text{network}} = 0.6\,\Omega$ as input.

Since the probability for electric arcs between individual coil windings is determined by the effective coil voltage per winding $U_{\text{coil,eff}}/N_{\text{coil windings}}$, this quantity is evaluated as well. As shown in the right plot of figure 5.8 the number of coil

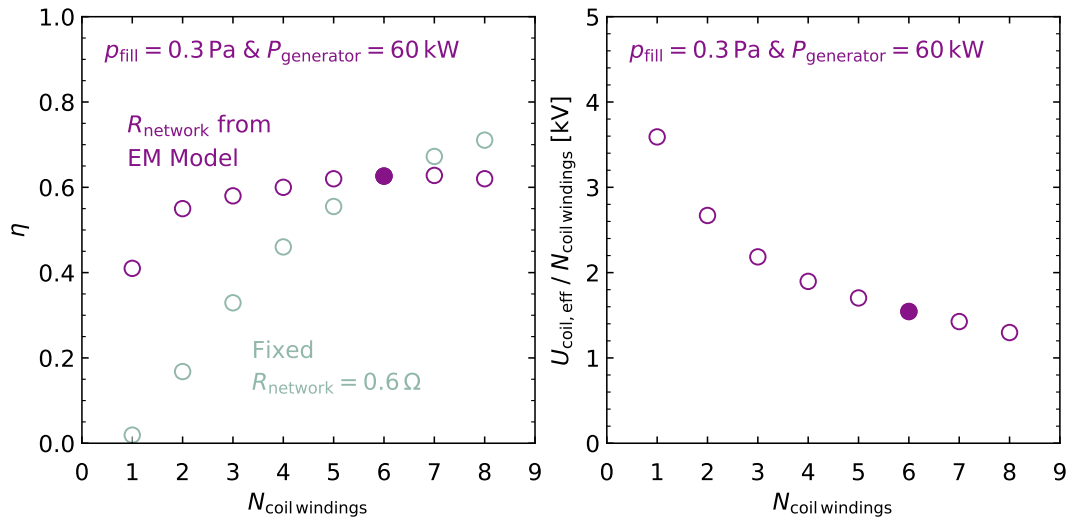

Figure 5.8: *Left plot: η as a function of the number of coil windings $N_{\text{coil windings}}$. Plotted along in green are the values obtained from the RF power coupling model for a fixed $R_{\text{network}} = 0.6\,\Omega$. Right plot: corresponding effective coil voltage per winding. The full symbols indicate the experimentally validated values.*

windings strongly affects the effective coil voltage per winding. For this reason it is beneficial to use a larger number of coil windings. However, using more coil windings inevitably decreases the distance between the coil windings and the conducting back plates (see figure 3.2), where eddy currents are driven. Hence, the impact of the distance from the coil to the back plates is investigated in detail in the next section.

5.2.2 Coil position

The impact of the distance between the RF coil and the surrounding metallic structure such as the driver and source back plates is studied by shifting the coil away from its axially central position at $z = 6\,\text{cm}$ towards the back plates. To isolate the effect of the coil position, a small coil with only two windings is used. In figure 5.9 R_{network} is shown to be rather flat when the coil is shifted axially away from its central position. R_{network} decreases slightly when the RF coil gets close to one of the back plates, because in this case less eddy currents are driven in the Faraday screen. Plotted along is the corresponding R_{plasma}, which decreases when

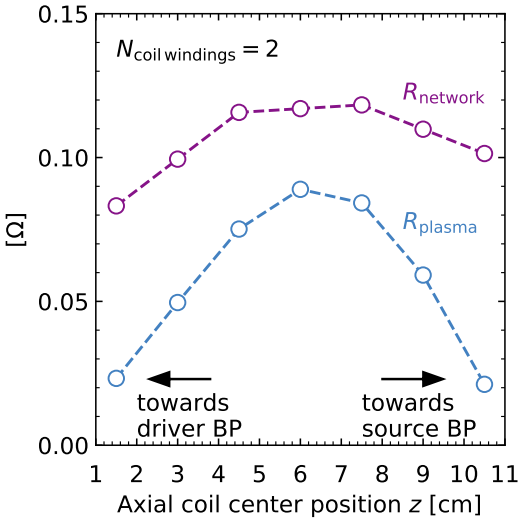

Figure 5.9: *R_{network} and R_{plasma} for $N_{\text{coil windings}} = 2$ as a function of the axial coil center position z between the driver back plate and the source back plate.*

the coil gets closer to one of the back plates. This decrease has two reasons. Firstly, the electric component of the RF field gets pinched, as exemplarily shown for a coil shifted towards the source back plate in the right plot of figure 5.10. In this case, the field pinch is caused by the source back plate at $z = 12\,\text{cm}$, since the RF field component (which is parallel to the boundary) cannot penetrate and thus is zero directly at the back plate. Secondly, a considerable amount of the plasma volume is not penetrated by the RF field, when the coil is positioned close to a back plate instead of being axially centered.

The resulting η is shown in figure 5.11. Quantitatively, η is decreased by around 0.1 for an axial shift of $\pm 3\,\text{cm}$ from the center, corresponding to a distance of 2 cm between the outer coil winding closest to the back plate and the back plate. For an axial shift from the center of $\pm 1.5\,\text{cm}$, the resulting decrease in η is below 0.05. This corresponds to a shortest distance between the outer coil winding closest to the back plate and the back plate of 3.5 cm.

To completely avoid the pinch effect, the RF coil should be kept as far away as possible from the back plates, i.e. axially centered. For the current setup of the BUG ion source driver with $N_{\text{coil windings}} = 6$, the distances of the outer coil windings to the source and the driver back plate, respectively are around 2.5 cm. However,

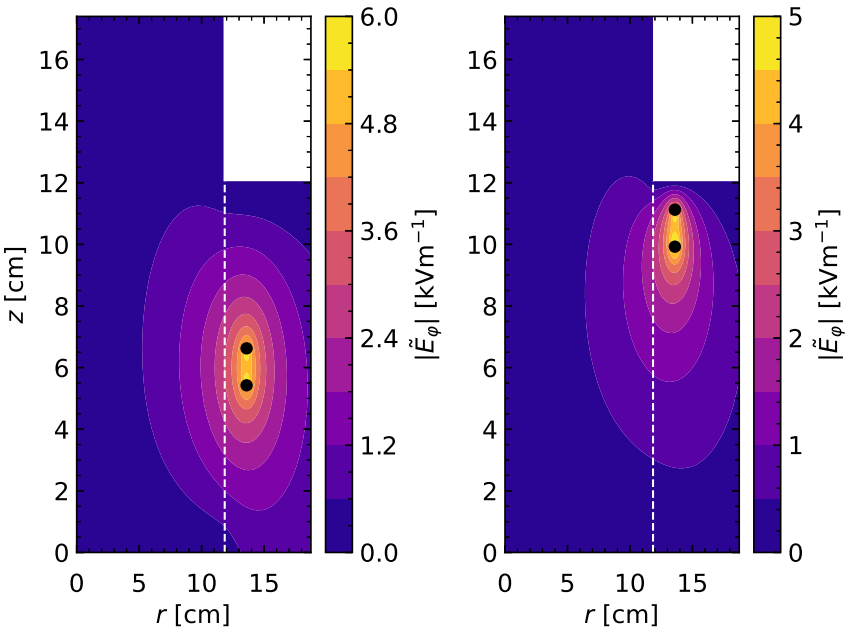

Figure 5.10: *Amplitude of the electric RF field component $|\tilde{E}_\varphi|$ for two different axial positions of the RF coil with $N_{\text{coil windings}} = 2$. Left plot: RF coil axially centered at $z = 6$ cm in between the driver back plate (at $z = 0$ cm) and the source back plate (at $z = 12$ cm). Right: axial coil center position $z = 10.5$ cm, i.e. the RF coil is shifted close to the source back plate.*

using more coil windings and thus decreasing the minimum distance between the outermost coil winding and back plate to around 1.5 cm for $N_{\text{coil windings}} = 8$ does not decrease η, as shown in the left plot of figure 5.8. Hence the pinch effect is not so relevant for the RF power coupling. However, it is of great importance that the electric RF field component occupies as much as possible of the available driver volume in order to facilitate the RF power coupling. This is achieved by axially centering the coil between the back plates, as shown in the left plot of figure 5.10.

The spread between the coil windings is also investigated numerically in the $N_{\text{coil windings}} = 2$ configuration. The result is that the impact of the spread on η is negligible even for comparatively large distances up to 6 cm between the two coil windings. This is so because even in this case the electric field occupies the full plasma volume that lies axially between the two coil windings.

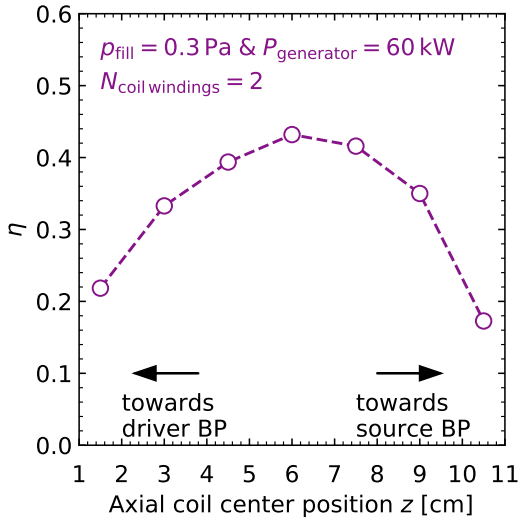

Figure 5.11: *RF power transfer efficiency η for $N_{\text{coil windings}} = 2$ as a function of the axial coil center position between the driver back plate and the source back plate.*

5.3 Applied frequency

Due to the RF skin effect in a conducting medium the RF current flows in a thin skin layer within the skin depth $\delta_{\text{RF,conductor}}$, as given by equation (2.27). Herein the skin depth scales as $f_{\text{RF}}^{-1/2}$, i.e. it decreases with increasing frequency f_{RF}. The resistance of a lumped resistive component R can be expressed as in equation (2.28). Together with the above scaling, it follows

$$R \propto f_{\text{RF}}^{1/2}. \tag{5.1}$$

The network resistance shown in figure 5.12 is subject to this scaling, because the main network losses are in the RF coil and the Faraday screen. Both objects are made of copper, where $\delta_{\text{RF,copper}} = 65\,\mu\text{m}$ at 1 MHz.

The frequency scaling from equation (5.1) is used in the RF power coupling model to obtain R_{plasma}, as shown in figure 5.12. R_{plasma} increases considerably when f_{RF} is increased because of the lower RF coil current amplitude I_0 needed to produce the same absorbed power. For example at 30 MHz an I_0 of only around 30 A is needed, whereas at 1 MHz $I_0 \approx 300\,\text{A}$ is needed to produce the same absorbed

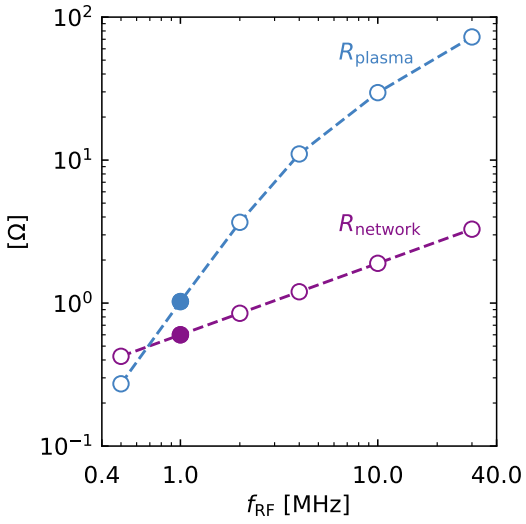

Figure 5.12: *$R_{network}$ and R_{plasma} as a function of the driving frequency f_{RF}. Full symbols indicate the validated values at $f_{RF} = 1$ MHz.*

power (cf. figure 4.16). The increase in R_{plasma} is so large that it dominates the trend of the RF power transfer efficiency. As shown in the left plot of figure 5.13, η increases when the applied frequency is increased reaching values slightly above 0.95 at 30 MHz.

It follows from equation (2.26) that also $U_{coil,eff}$ increases with the applied frequency. Since I_0 decreases with increasing f_{RF}, it is not a priori clear how $U_{coil,eff}$ scales with f_{RF}. For this reason $U_{coil,eff}$ is calculated using the RF coil current amplitudes obtained from the RF power coupling model. For the inductance $L_{coil} = 9.4\,\mu$H is used, as measured with a precision LCR meter (Agilent Technologies model E4980A) [24]. The right plot of figure 5.13 shows the resulting functional dependency. Up to 2 MHz, the increasing frequency is almost fully compensated by the decreasing RF coil current, wherefore $U_{coil,eff}$ remains substantially unchanged at around 10 kV. However, for $f_{RF} > 2$ MHz, $U_{coil,eff}$ starts to increase resulting in $U_{coil,eff} \approx 35$ kV at 30 MHz. As a conclusion to this, using a higher applied frequency of 2 MHz would lead to a considerable increase in η of 0.2, whereas the effective coil voltage remains constant, i.e. there is no increased probability for electric arcs. By using larger frequencies, $U_{coil,eff}$ starts to increase, wherefore it is

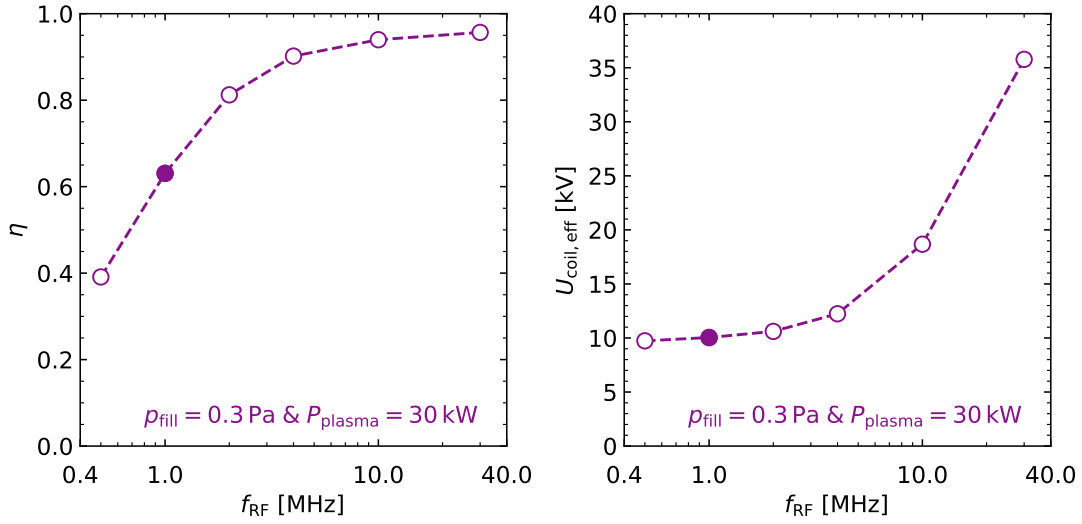

Figure 5.13: *RF power transfer efficiency η (left plot) and effective coil voltage $U_{\mathrm{coil,eff}}$ (right plot) as a function of the applied frequency f_{RF}. The full symbols indicate the values for the validated case of $f_{\mathrm{RF}} = 1\,\mathrm{MHz}$.*

not advisable to use an applied frequency that is larger than 2 MHz despite the even higher RF power transfer efficiency.

5.4 Global optimization

The optimization studies show that the two most promising external parameters for optimizing η are the driver length L_{driver} and the applied frequency f_{RF}. The η values for the status quo as well as the ones for optimized parameters (individually or together) are shown in table 5.1.

Table 5.1: *Global optimization of the RF power transfer efficiency η.*

	Status quo	L_{driver} optimized	f_{RF} optimized	L_{driver} & f_{RF} optimized
η	0.63	0.85	0.81	0.9

The globally optimized value of η is 0.9 for $L_{\mathrm{driver}} = 40\,\mathrm{cm}$ and $f_{\mathrm{RF}} = 2\,\mathrm{MHz}$. Hence, the combined optimization increases η by 0.05 and 0.09, respectively, when compared to the individual optimization of the two parameters. For optimizing η

in an already existing ion source, such as the one at the BUG test bed, it might be preferable to optimize only L_{driver}, since this is less expensive and time demanding than procuring and commissioning a new RF generator inclusive the RF circuit with matching transformer and capacities. The most laborious part is the design and the manufacturing of a Faraday screen that has to be customized to the increased driver length. For new ion sources that are still in the design phase both parameters should be optimized to achieve the globally optimized η. However, installation space constraints for a longer driver have to be taken into consideration, since it might have to fit into a vacuum chamber of a specific size.

6 Conclusion

In this work a predictive numerical model was developed to self-consistently simulate the RF power coupling and maximize the RF power transfer efficiency in negative hydrogen RF ion sources.

As a modeling approach a 3D electromagnetic (EM) model, developed in the framework of a master thesis [102], was used for the calculation of the network losses. These are Joule losses in the RF coil antenna, as well as eddy current losses in the Faraday screen and in the conducting components surrounding the discharge. The resulting power losses were used as one of the input parameters in the self-consistent RF power coupling model. In this model the plasma and neutral species are described as fluids, coupled to Maxwell's equations for the description of the electromagnetic fields. The fluid approach was chosen, since on the one hand kinetic models are numerically too expensive for the rather large volume and high plasma densities in an ion source. On the other hand zero dimensional global models are not capable of describing the spatially resolved bidirectional coupling between the RF fields and the electrons in the plasma. A 2D cylindrically symmetric simulation domain was assumed to improve the numerical efficiency of the model.

There are numerous fluid models for the description of RF ion source discharges in the literature. However, none of these models describes the RF power coupling in an ion source self-consistently. The reason for this is the complex interplay of various nonlinear phenomena that take place in an RF ion source plasma.

The most significant challenge resulted from the low driving frequency of 1 MHz combined with the high applied power of up to 100 kW, where magnetic RF field strengths in the plasma are well above 100 G. Hence the discharges were found to operate in the 'high magnetic RF field region' of the local skin effect regime. In this region the magnetic RF fields are even larger than in the so-called nonlinear

regime, where it is known that the nonlinear RF Lorentz force plays an important part in the RF power coupling. The typical behavior of the state-of-the-art models was confirmed, where the RF Lorentz force compresses the plasma such that no steady state solution of the models was obtained. However, during the validation studies performed in this work, it was shown that by retaining the RF Lorentz force as well as the term associated with the electron viscosity the increased RF current diffusion decreases the RF current density in the plasma. This in turn reduces the compression. By using the Navier-Stokes limit for the kinematic viscosity in the 'high magnetic RF field region' of the local skin effect regime, a self-consistent steady state solution was obtained for the first time with an RF power coupling model. Moreover, a fairly good match between the experimentally obtained electrical and local plasma parameters and the modeled ones was achieved.

Another important part in the description of RF ion source discharges at low pressures between 0.2 and 0.5 Pa is neutral depletion, i.e. the neutrals are significantly depleted due to ionization. To describe this in a fluid model, the Navier-Stokes equations for the hydrogen atoms and molecules (including energy transport equations) were used, in contrast to a uniform neutrals background approximation, that is often applied. Thereby it was shown that neutral depletion is present at all investigated pressures and becomes even more pronounced at higher RF powers. By additionally scaling the boundary fluxes using the highly non-Maxwellian neutrals distribution functions from existing kinetic simulations, it was shown that the impact of the higher atomic densities (resulting from the non-Maxwellian distribution function) on the RF power transfer efficiency is slightly above 0.1 and thus cannot be neglected.

First studies regarding the impact of a simplified magnetostatic cusp field on the RF power coupling were performed. The purpose of the cusp field is to reduce the plasma losses to the wall and thus increase the plasma density in the driver. However, in the model validation studies it was qualitatively shown that the presence of a cusp field also decreases the plasma's ability to absorb RF power, because the transport barrier for the electrons due to the magnetic field leads to a depletion of the electrons in the vicinity of the RF coil antenna, where the power coupling takes place. This suggests that dedicated optimization studies of the cusp field are worthwhile.

A comprehensive data set of electrical parameters such as RF coil current and RF power transfer efficiency as well as local plasma density, potential and electron temperature were experimentally obtained for the first time at the ITER prototype RF ion source. Hereby it was demonstrated, that typical values of η are surprisingly low between 0.5 and 0.6, depending on the operation point. This data set may also serve for comparison with other RF ion sources or more standard inductively coupled plasma setups. The RF power coupling model was successfully validated using the comprehensive experimental data set, i.e. the model reproduces all measured trends. Furthermore, a considerable fraction of the modeled absolute values are within the experimental error bars. Hence the unique characteristic of the model is its ability to self-consistently calculate a steady state solution as well as its successful validation, wherefore it is predictive, as opposed to previously existing models.

In the subsequent optimization studies it was found that the two most promising external parameters for the optimization of η are the driver length and the applied frequency.

- *Driver length optimization:* Increasing the axial length of the driver has the largest positive impact on η of all parameters. The reason for this is the larger plasma volume that comes with the larger length, where the RF fields can couple to more electrons in the plasma. The model shows that by increasing the driver length a maximum increase in η of around 0.25 to a value of 0.85 is possible. At the same time the coil voltage and thus the probability for electrical breakdowns and arcs is minimized.

- *Frequency optimization:* Applying higher frequencies than 1 MHz yields lower RF coil currents. This is found to dominate over the increased losses in the RF network at higher frequencies. η increases by 0.2 to a value of 0.81 when the applied frequency is changed from 1 to 2 MHz. This increase is associated with an almost constant coil voltage, wherefore the probability for electrical breakdowns and arcs remains substantially unchanged. When going to higher frequencies the coil voltage starts to increase, wherefore this is not advisable, despite the even larger η.

- *Global optimization:* Optimizing both parameters simultaneously yields the global optimum of $\eta = 0.9$. This is an improvement of around 0.3 compared to the status quo. At the same time the coil currents and voltages are reduced.

- *Further external parameters:* Changing the driver radius, as well as optimizations regarding the RF coil such as changing the number of coil windings and the coil position are found to have no significant effect on η.

As a conclusion of the optimization studies it is in principle advisable to implement both optimization measures, since the nonlinearity of both effects yields a globally optimized η of 0.9, which is even larger than the individually optimized ones.

Outlook

Several extensions of the model are conceivable. The remaining systematic quantitative differences between model and experiment in the electron temperature (slightly too large in the model) and plasma density (too small by a factor of roughly five in the model) could most probably be eliminated by accounting for the magnetization of the ions via the magnetic cusp field. However, there is (as opposed to the electrons, where inertia can be neglected) no convenient way to introduce the magnetization of the ions in a 2D cylindrically symmetric model. Because of this and to study (and optimize) more realistic 3D topologies of the cusp field and the filter field, a *3D version of the model* is desirable. Here it is straight forward to account for the magnetization of electrons and ions in order to study the plasma drifts. However, because of the increased complexity, it is advisable to further validate the fluxes obtained from the 3D model. This can be done for example with a Mach probe.

Another important aspect is the kinetic description of the neutral particles. With the boundary flux scaling method developed in this work, it is possible to quantitatively account for the spatially resolved atomic and molecular densities in a fluid model, if the particle distribution functions of the neutrals are known. However, this is only the case at very few operation conditions. Nevertheless it is desirable to calculate the absolute values of the neutral densities and fluxes with a high precision at various operation conditions, because e.g. the atomic flux

towards the plasma grid directly influences the production yield of the surface created negative ions. This is possible by replacing the fluid neutrals with a *direct simulation Monte Carlo module for the neutrals*, which calculates the neutrals distribution function.

Note that both extensions lead to a significantly increased numerical effort, wherefore a computer cluster will become necessary for solving the equation system. However, implementing the two extensions enables not only RF power coupling investigations but also more global optimization studies of RF-driven ion sources.

Bibliography

[1] www.iter.org, accessed on 04.04.2021.

[2] F. Romanelli et al. *Fusion electricity - a roadmap to the realisation of fusion energy*. URL: https://www.euro-fusion.org/fileadmin/user_upload/Archive/wp-content/uploads/2013/01/JG12.356-web.pdf.

[3] *ITER Technical Basis*. ITER EDA Documentation Series 24. Vienna: International Atomic Energy Agency, 2002. URL: https://www.iaea.org/publications/6492/iter-technical-basis.

[4] R. S. Hemsworth et al. "Overview of the design of the ITER heating neutral beam injectors". In: *New Journal of Physics* 19.2 (Feb. 2017), p. 025005. DOI: 10.1088/1367-2630/19/2/025005. URL: https://doi.org/10.1088/1367-2630/19/2/025005.

[5] K. H. Berkner et al. "Intense, mixed-energy hydrogen beams for CTR injection". In: *Nuclear Fusion* 15.2 (Apr. 1975), pp. 249–254. DOI: 10.1088/0029-5515/15/2/009. URL: https://doi.org/10.1088/0029-5515/15/2/009.

[6] U. Fantz et al. "Fundamental experiments on evaporation of cesium in ion sources". In: *Review of Scientific Instruments* 81.2 (2010), 02B102. DOI: 10.1063/1.3258428. URL: https://doi.org/10.1063/1.3258428.

[7] W. Kraus et al. "The development of the radio frequency driven negative ion source for neutral beam injectors (invited)". In: *Review of Scientific Instruments* 83.2 (2012), 02B104. DOI: 10.1063/1.3662957. URL: https://doi.org/10.1063/1.3662957.

[8] B. Heinemann et al. “Upgrade of the BATMAN test facility for H^- source development”. In: *AIP Conference Proceedings* 1655.1 (2015), p. 060003. DOI: 10.1063/1.4916472. URL: https://aip.scitation.org/doi/abs/10.1063/1.4916472.

[9] B. Heinemann et al. “Towards large and powerful radio frequency driven negative ion sources for fusion”. In: *New Journal of Physics* 19.1 (Jan. 2017), p. 015001. DOI: 10.1088/1367-2630/aa520c. URL: https://doi.org/10.1088/1367-2630/aa520c.

[10] B. Heinemann et al. “The negative ion source test facility ELISE”. In: *Fusion Engineering and Design* 86.6 (2011). Proceedings of the 26th Symposium of Fusion Technology (SOFT-26), pp. 768–771. ISSN: 0920-3796. DOI: https://doi.org/10.1016/j.fusengdes.2010.11.031. URL: https://www.sciencedirect.com/science/article/pii/S0920379610005028.

[11] U. Fantz et al. “Development of negative hydrogen ion sources for fusion: Experiments and modelling”. In: *Chemical Physics* 398 (2012). Chemical Physics of Low-Temperature Plasmas, pp. 7–16. ISSN: 0301-0104. DOI: https://doi.org/10.1016/j.chemphys.2011.05.006. URL: https://www.sciencedirect.com/science/article/pii/S0301010411001601.

[12] U. Fantz et al. “Size scaling of negative hydrogen ion sources for fusion”. In: *AIP Conference Proceedings* 1655.1 (2015), p. 040001. DOI: 10.1063/1.4916443. URL: https://aip.scitation.org/doi/abs/10.1063/1.4916443.

[13] U. Fantz et al. “Towards powerful negative ion beams at the test facility ELISE for the ITER and DEMO NBI systems”. In: *Nuclear Fusion* 57.11 (Aug. 2017), p. 116007. DOI: 10.1088/1741-4326/aa778b. URL: https://doi.org/10.1088/1741-4326/aa778b.

[14] J. Hopwood. “Planar RF induction plasma coupling efficiency”. In: *Plasma Sources Sci. Technol.* 3.4 (1994), p. 460. URL: http://stacks.iop.org/0963-0252/3/i=4/a=002.

[15] V. A. Godyak et al. "Experimental setup and electrical characteristics of an inductively coupled plasma". In: *Journal of Applied Physics* 85.2 (1999), pp. 703–712. DOI: 10.1063/1.369150. URL: https://doi.org/10.1063/1.369150.

[16] E. A. Kralkina et al. "RF power absorption by plasma of a low-pressure inductive discharge". In: *Plasma Sources Science and Technology* 25.1 (Jan. 2016), p. 015016. DOI: 10.1088/0963-0252/25/1/015016. URL: https://doi.org/10.1088%2F0963-0252%2F25%2F1%2F015016.

[17] D. Rauner et al. "RF power transfer efficiency of inductively coupled low pressure H_2 and D_2 discharges". In: *Plasma Sources Science and Technology* 26.9 (Aug. 2017), p. 095004. DOI: 10.1088/1361-6595/aa8685. URL: https://doi.org/10.1088/1361-6595/aa8685.

[18] P. Jain et al. "Evaluation of power transfer efficiency for a high power inductively coupled radio-frequency hydrogen ion source". In: *Plasma Physics and Controlled Fusion* 60.4 (Apr. 2018), p. 045007. DOI: 10.1088/1361-6587/aaab19. URL: https://doi.org/10.1088/1361-6587/aaab19.

[19] P. Jain et al. "Improved Methodology to Estimate the Power Transfer Efficiency in an Inductively Coupled Radio Frequency Ion Source". In: *IEEE Access* 6 (2018), pp. 29665–29676. DOI: 10.1109/ACCESS.2018.2829618.

[20] A. Shivarova et al. "Discharge regime of non-ambipolarity with a self-induced steady-state magnetic field in plasma sources with localized radio-frequency power deposition". In: *Physics of Plasmas* 22.10 (2015), p. 100705. DOI: 10.1063/1.4933411. URL: https://doi.org/10.1063/1.4933411.

[21] S. Lishev et al. "Fluid-model analysis on discharge structuring in the RF-driven prototype ion-source for ITER NBI". In: *Plasma Sources Science and Technology* 27.12 (Dec. 2018), p. 125008. DOI: 10.1088/1361-6595/aaf536. URL: https://doi.org/10.1088/1361-6595/aaf536.

[22] G. J. M. Hagelaar et al. "Model of an inductively coupled negative ion source: I. General model description". In: *Plasma Sources Sci. Technol.* 20.1 (2011), p. 015001. DOI: 10.1088/0963-0252/20/1/015001. URL: https://doi.org/10.1088%2F0963-0252%2F20%2F1%2F015001.

[23] J. P. Boeuf et al. “Model of an inductively coupled negative ion source: II. Application to an ITER type source”. In: *Plasma Sources Sci. Technol.* 20.1 (2011), p. 015002. DOI: 10.1088/0963-0252/20/1/015002. URL: https://doi.org/10.1088%2F0963-0252%2F20%2F1%2F015002.

[24] D. Zielke et al. “RF power transfer efficiency and plasma parameters of low pressure high power ICPs”. In: *Journal of Physics D: Applied Physics* 54.15 (Feb. 2021), p. 155202. DOI: 10.1088/1361-6463/abd8ee. URL: https://doi.org/10.1088/1361-6463/abd8ee.

[25] E. Speth et al. “Overview of the RF source development programme at IPP Garching”. In: *Nuclear Fusion* 46.6 (May 2006), S220–S238. DOI: 10.1088/0029-5515/46/6/s03. URL: https://doi.org/10.1088/0029-5515/46/6/s03.

[26] M. Bacal. “Physics aspects of negative ion sources”. In: *Nuclear Fusion* 46.6 (May 2006), S250–S259. DOI: 10.1088/0029-5515/46/6/s05. URL: https://doi.org/10.1088/0029-5515/46/6/s05.

[27] M. Fröschle et al. “Recent developments at IPP on evaporation and control of caesium in negative ion sources”. In: *Fusion Engineering and Design* 84.2 (2009). Proceeding of the 25th Symposium on Fusion Technology, pp. 788–792. ISSN: 0920-3796. DOI: https://doi.org/10.1016/j.fusengdes.2008.12.063. URL: https://www.sciencedirect.com/science/article/pii/S092037960800519X.

[28] P. McNeely and D. Wünderlich. “Neutral depletion in an H^- source operated at high RF power and low input gas flow”. In: *Plasma Sources Science and Technology* 20.4 (May 2011), p. 045005. DOI: 10.1088/0963-0252/20/4/045005. URL: https://doi.org/10.1088/0963-0252/20/4/045005.

[29] A. Krylov and R. S. Hemsworth. “Gas flow and related beam losses in the ITER neutral beam injector”. In: *Fusion Engineering and Design* 81.19 (2006), pp. 2239–2248. ISSN: 0920-3796. DOI: https://doi.org/10.1016/j.fusengdes.2006.03.006. URL: https://www.sciencedirect.com/science/article/pii/S0920379606001396.

[30] L. Schiesko et al. "Magnetic field dependence of the plasma properties in a negative hydrogen ion source for fusion". In: *Plasma Physics and Controlled Fusion* 54.10 (Aug. 2012), p. 105002. DOI: 10.1088/0741-3335/54/10/105002. URL: https://doi.org/10.1088/0741-3335/54/10/105002.

[31] R. K. Janev et al. *Collision processes in low-temperature hydrogen plasmas*. Vol. 4105. Berichte des Forschungszentrums Jülich. Record converted from VDB: 12.11.2012. Jülich: Forschungszentrum, Zentralbibliothek, 2003. URL: http://juser.fz-juelich.de/record/38224.

[32] U. Fantz et al. "Plasma expansion across a transverse magnetic field in a negative hydrogen ion source for fusion". In: *Plasma Sources Science and Technology* 23.4 (July 2014), p. 044002. DOI: 10.1088/0963-0252/23/4/044002. URL: https://doi.org/10.1088/0963-0252/23/4/044002.

[33] M. A. Lieberman and A. J. Lichtenberg. *Principles of Plasma Discharges and Materials Processing*. Second Edition. John Wiley & Sons, Inc., Hoboken, New Jersey, 2005.

[34] R. Schunk and A. Nagy. *Ionospheres: Physics, Plasma Physics and Chemistry*. Second Edition. Cambridge University Press, 2009.

[35] N. Kohen. "Physique et modélisation d'une source d'ions négatifs pour l'injection du faisceau de neutres sur ITER". PhD thesis. Université de Toulouse, 2015. URL: http://thesesups.ups-tlse.fr/2785/.

[36] A. Fruchtman. "Neutral gas depletion in low temperature plasma". In: *Journal of Physics D: Applied Physics* 50.47 (Oct. 2017), p. 473002. DOI: 10.1088/1361-6463/aa87a9. URL: https://doi.org/10.1088/1361-6463/aa87a9.

[37] F. F. Chen. *Introduction to Plasma Physics and Controlled Fusion*. Third Edition. Springer International Publishing, 2016. ISBN: 978-3-319-22308-7. DOI: 10.1007/978-3-319-22309-4.

[38] D. Lee et al. "Exact Solution for the Generalized Bohm Criterion in a Two-Ion-Species Plasma". In: *Phys. Rev. Lett.* 99 (15 Oct. 2007), p. 155004. DOI: 10.1103/PhysRevLett.99.155004. URL: https://link.aps.org/doi/10.1103/PhysRevLett.99.155004.

[39] P. Chabert and N. Braithwaite. *Physics of Radio-Frequency Plasmas*. First Edition. Cambridge Univ. Press, 2011. ISBN: 978-0-521-76300-4.

[40] G. J. M. Hagelaar and N. Oudini. "Plasma transport across magnetic field lines in low-temperature plasma sources". In: *Plasma Physics and Controlled Fusion* 53.12 (Nov. 2011), p. 124032. DOI: 10.1088/0741-3335/53/12/124032. URL: https://doi.org/10.1088/0741-3335/53/12/124032.

[41] P. Franzen et al. "Magnetic filter field dependence of the performance of the RF driven IPP prototype source for negative hydrogen ions". In: *Plasma Physics and Controlled Fusion* 53.11 (Oct. 2011), p. 115006. DOI: 10.1088/0741-3335/53/11/115006. URL: https://doi.org/10.1088/0741-3335/53/11/115006.

[42] A. V. Phelps. "Cross Sections and Swarm Coefficients for H^+, H_2^+, H_3^+, H, H_2, and H^- in H_2 for Energies from 0.1 eV to 10 keV". In: *Journal of Physical and Chemical Reference Data* 19.3 (1990), pp. 653–675. DOI: 10.1063/1.555858. URL: http://dx.doi.org/10.1063/1.555858.

[43] W. Kraus et al. "Ways to improve the efficiency and reliability of radio frequency driven negative ion sources for fusion". In: *Rev. Sci. Instrum.* 85.2 (2014), 02B309. DOI: 10.1063/1.4832137.

[44] E. Gaio et al. "Studies on the radio frequency power supply system for the ITER NB injector ion source". In: *Fusion Engineering and Design* 82.5 (2007). Proceedings of the 24th Symposium on Fusion Technology, pp. 912–919. ISSN: 0920-3796. DOI: https://doi.org/10.1016/j.fusengdes.2007.07.028. URL: https://www.sciencedirect.com/science/article/pii/S0920379607003584.

[45] F. F. Chen. *Capacitor tuning circuits for inductive loads*. 1992. URL: http://www.seas.ucla.edu/~ffchen/Publs/Chen144.pdf.

[46] Elsyscom. *50 kW Solid State MF Broadcast Transmitter TRAM 50 Datasheet*. URL: https://elsyscom.de/wp-content/uploads/2019/11/Datasheet_TRAM-50AN_ELS.pdf.

[47] R. B. Piejak et al. "A simple analysis of an inductive RF discharge". In: *Plasma Sources Science and Technology* 1.3 (1992), p. 179. URL: http://stacks.iop.org/0963-0252/1/i=3/a=006.

[48] J. D. Jackson. *Classical electrodynamics*. Third Edition. New York, NY: Wiley, 1999. ISBN: 9780471309321.

[49] M. Bauccio. *ASM engineered materials reference book*. English. Materials Park, OH: ASM International, 1994. ISBN: 9780871705020.

[50] A. M. Froese et al. "Nonlinear skin effect in a collisionless plasma". In: *Physics of Plasmas* 16.8 (2009), p. 080704. DOI: 10.1063/1.3211196. URL: https://doi.org/10.1063/1.3211196.

[51] G. J. M. Hagelaar. "Effective-Viscosity Approach for Nonlocal Electron Kinetics in Inductively Coupled Plasmas". In: *Phys. Rev. Lett.* 100 (2 Jan. 2008), p. 025001. DOI: 10.1103/PhysRevLett.100.025001. URL: https://link.aps.org/doi/10.1103/PhysRevLett.100.025001.

[52] V. Vahedi and M. A. Lieberman. "Analytic model of power deposition in inductively coupled plasma sources". In: *Journal of Applied Physics* 78 (1995), pp. 1446–1458. DOI: 10.1063/1.360723.

[53] M. M. Turner. "Collisionless heating in radio-frequency discharges: a review". In: *Journal of Physics D: Applied Physics* 42.19 (Sept. 2009), p. 194008. DOI: 10.1088/0022-3727/42/19/194008. URL: https://doi.org/10.1088/0022-3727/42/19/194008.

[54] D. Zielke et al. "Self-consistent fluid model for simulating power coupling in hydrogen ICPs at 1 MHz including the nonlinear RF Lorentz force". In: *Plasma Sources Science and Technology* (2021). URL: http://iopscience.iop.org/article/10.1088/1361-6595/ac0396.

[55] A. I. Smolyakov et al. "Effect of the electron thermal motion on the ponderomotive force in inductive plasma". In: *Physics of Plasmas* 8.9 (2001), pp. 3857–3860. DOI: 10.1063/1.1386941. URL: https://doi.org/10.1063/1.1386941.

[56] A. I. Smolyakov et al. “Nonlinear effects in inductively coupled plasmas”. In: *Physics of Plasmas* 10.5 (2003), pp. 2108–2116. DOI: 10.1063/1.1566443. URL: https://doi.org/10.1063/1.1566443.

[57] D. Y. Sydorenko et al. “Simulations of ponderomotive effects in inductively coupled plasmas”. In: *Physics of Plasmas* 12.3 (2005), p. 033503. DOI: 10.1063/1.1849797. URL: https://doi.org/10.1063/1.1849797.

[58] V. I. Kolobov and V. A. Godyak. “Inductively coupled plasmas at low driving frequencies”. In: *Plasma Sources Science and Technology* 26.7 (July 2017), p. 075013. DOI: 10.1088/1361-6595/aa7584. URL: https://doi.org/10.1088%2F1361-6595%2Faa7584.

[59] V. V. Aristov. *Direct Methods for Solving the Boltzmann Equation and Study of Nonequilibrium Flows*. Fluid Mechanics and Its Applications. Springer Netherlands, 2001.

[60] G. A. Bird. *Molecular Gas Dynamics and the Direct Simulation of Gas Flows*. Clarendon Press, 1994.

[61] S. I. Braginskii. “Transport Processes in Plasma”. In: *Reviews of Plasma Physics* 1 (1965), pp. 205–311.

[62] L. L. Alves et al. “Foundations of modelling of nonequilibrium low-temperature plasmas”. In: *Plasma Sources Science and Technology* 27.2 (Feb. 2018), p. 023002. DOI: 10.1088/1361-6595/aaa86d. URL: https://doi.org/10.1088%2F1361-6595%2Faaa86d.

[63] K. Nanbu. “Probability theory of electron-molecule, ion-molecule, molecule-molecule, and Coulomb collisions for particle modeling of materials processing plasmas and cases”. In: *IEEE Transactions on Plasma Science* 28.3 (2000), pp. 971–990. DOI: 10.1109/27.887765.

[64] S. Mattei et al. “A fully-implicit Particle-In-Cell Monte Carlo Collision code for the simulation of inductively coupled plasmas”. In: *Journal of Computational Physics* 350.Supplement C (2017), pp. 891–906. ISSN: 0021-9991. DOI: https://doi.org/10.1016/j.jcp.2017.09.015. URL: http://www.sciencedirect.com/science/article/pii/S0021999117306745.

[65] S. Briefi et al. "Experimental benchmark of the NINJA code for application to the Linac4 H^- ion source plasma". In: *New Journal of Physics* 19.10 (Oct. 2017), p. 105006. DOI: 10.1088/1367-2630/aa8679. URL: https://doi.org/10.1088/1367-2630/aa8679.

[66] I. M. Montellano et al. "3D-PIC modelling of a low temperature plasma sheath with wall emission of negative particles and its application to NBI sources". In: *Journal of Physics D: Applied Physics* 52.23 (Mar. 2019), p. 235202. DOI: 10.1088/1361-6463/ab0f44. URL: https://doi.org/10.1088/1361-6463/ab0f44.

[67] R. Zorat et al. "Global model of a radiofrequency H_2 plasma in DENISE". In: *Plasma Sources Science and Technology* 9.2 (Mar. 2000), pp. 161–168. DOI: 10.1088/0963-0252/9/2/308. URL: https://doi.org/10.1088/0963-0252/9/2/308.

[68] C. M. Samuell and C. S. Corr. "Low-pressure hydrogen plasmas explored using a global model". In: *Plasma Sources Science and Technology* 25.1 (Dec. 2015), p. 015014. DOI: 10.1088/0963-0252/25/1/015014. URL: https://doi.org/10.1088/0963-0252/25/1/015014.

[69] P. McNeely et al. "A Langmuir probe system for high power RF-driven negative ion sources on high potential". In: *Plasma Sources Science and Technology* 18.1 (Nov. 2008), p. 014011. DOI: 10.1088/0963-0252/18/1/014011. URL: https://doi.org/10.1088/0963-0252/18/1/014011.

[70] V. E. Golant et al. *Fundamentals of Plasma Physics*. Wiley Series in Plasma Physics. John Wiley, 1980. ISBN: 9780471045939.

[71] S. Chapman et al. *The Mathematical Theory of Non-uniform Gases: An Account of the Kinetic Theory of Viscosity, Thermal Conduction and Diffusion in Gases*. Cambridge Mathematical Library. Cambridge University Press, 1990. ISBN: 9780521408448.

[72] J. Yoon et al. "Cross Sections for Electron Collisions with Hydrogen Molecules". In: *Journal of Physical and Chemical Reference Data* 37.2 (2008), pp. 913–931. DOI: 10.1063/1.2838023. URL: http://dx.doi.org/10.1063/1.2838023.

[73] J. Yoon et al. “Electron-impact cross sections for deuterated hydrogen and deuterium molecules”. In: *Reports on Progress in Physics* 73.11 (Oct. 2010), p. 116401. DOI: 10.1088/0034-4885/73/11/116401. URL: https://doi.org/10.1088/0034-4885/73/11/116401.

[74] O. Fukumasa et al. “Numerical simulation of hydrogen ion species in the steady-state plasma of a low-pressure ion source”. In: *Journal of Physics D: Applied Physics* 18.12 (1985), p. 2433. URL: http://stacks.iop.org/0022-3727/18/i=12/a=012.

[75] I. Koleva et al. “Surface-wave produced discharges in hydrogen: I. Self-consistent model of diffusion-controlled discharges”. In: *Plasma Sources Science and Technology* 12.4 (2003), p. 597. URL: http://stacks.iop.org/0963-0252/12/i=4/a=311.

[76] L. Marques et al. “Capacitively coupled radio-frequency hydrogen discharges: The role of kinetics”. In: *Journal of Applied Physics* 102.6 (2007), p. 063305. DOI: 10.1063/1.2779268. URL: https://doi.org/10.1063/1.2779268.

[77] A. T. Hjartarson et al. “Low pressure hydrogen discharges diluted with argon explored using a global model”. In: *Plasma Sources Science and Technology* 19.6 (Nov. 2010), p. 065008. DOI: 10.1088/0963-0252/19/6/065008. URL: https://doi.org/10.1088/0963-0252/19/6/065008.

[78] F. Taccogna et al. “Modeling of a negative ion source. III. Two-dimensional structure of the extraction region”. In: *Physics of Plasmas* 17.6 (2010), p. 063502. DOI: 10.1063/1.3431635. URL: https://doi.org/10.1063/1.3431635.

[79] Ts. Paunska et al. “Negative hydrogen ion maintenance in small radius discharges: Two-dimensional modeling”. In: *Physics of Plasmas* 18.2 (2011), p. 023503. DOI: 10.1063/1.3553463. URL: https://doi.org/10.1063/1.3553463.

[80] F. Gaboriau and J. P. Boeuf. “Chemical kinetics of low pressure high density hydrogen plasmas: application to negative ion sources for ITER”. In: *Plasma Sources Science and Technology* 23.6 (Oct. 2014), p. 065032. DOI:

10.1088/0963-0252/23/6/065032. URL: https://doi.org/10.1088/0963-0252/23/6/065032.

[81] F. Taccogna et al. "Non-equilibrium in low-temperature plasmas". In: *The European Physical Journal D* 70.11 (Nov. 2016), p. 251. ISSN: 1434-6079. DOI: 10.1140/epjd/e2016-70474-0. URL: https://doi.org/10.1140/epjd/e2016-70474-0.

[82] Dirk Wünderlich and Ursel Fantz. "Evaluation of State-Resolved Reaction Probabilities and Their Application in Population Models for He, H, and H_2". In: *Atoms* 4.4 (2016). ISSN: 2218-2004. DOI: 10.3390/atoms4040026. URL: https://www.mdpi.com/2218-2004/4/4/26.

[83] G. Fubiani et al. "Modeling of plasma transport and negative ion extraction in a magnetized radio-frequency plasma source". In: *New Journal of Physics* 19.1 (Jan. 2017), p. 015002. DOI: 10.1088/1367-2630/19/1/015002. URL: https://doi.org/10.1088/1367-2630/19/1/015002.

[84] A. Mimo et al. "Modelling of caesium dynamics in the negative ion sources at BATMAN and ELISE". In: *AIP Conference Proceedings* 1869.1 (2017), p. 030019. DOI: 10.1063/1.4995739. URL: https://aip.scitation.org/doi/abs/10.1063/1.4995739.

[85] G. Fubiani et al. "Modeling of negative ion extraction from a magnetized plasma source: Derivation of scaling laws and description of the origins of aberrations in the ion beam". In: *Physics of Plasmas* 25.2 (2018), p. 023510. DOI: 10.1063/1.4999707. URL: https://doi.org/10.1063/1.4999707.

[86] U. Fantz and D. Wünderlich. *Effective rate coefficients for molecular processes of hydrogen and hydrocarbons in edge plasmas*. Atomic and molecular physics. International Atomic Energy Agency: IAEA, 2008. URL: http://inis.iaea.org/search/search.aspx?orig_q=RN:39050276.

[87] U. Fantz and C. Wimmer. "Cesium dynamics in long pulse operation of negative hydrogen ion sources for fusion". In: *Review of Scientific Instruments* 83.2 (2012), 02B110. DOI: 10.1063/1.3670347. URL: https://doi.org/10.1063/1.3670347.

[88] IST-Lisbon database. URL: https://www.lxcat.net (visited on 03/20/2018).

[89] M. Mukherjee et al. “Elastic electron-hydrogen scattering at intermediate energies”. In: *Phys. Rev. A* 36 (2 July 1987), pp. 937–940. DOI: 10.1103/PhysRevA.36.937. URL: https://link.aps.org/doi/10.1103/PhysRevA.36.937.

[90] I. Bray et al. “Convergence of an L^2 approach in the coupled-channel optical-potential method for e-H scattering”. In: *Phys. Rev. A* 43 (3 Feb. 1991), pp. 1301–1305. DOI: 10.1103/PhysRevA.43.1301. URL: https://link.aps.org/doi/10.1103/PhysRevA.43.1301.

[91] International Atomic Energy Agency. *Atomic and Plasma–Material Interaction Data for Fusion.* Atomic and Plasma–Material Interaction Data for Fusion 8. Vienna, 1999. URL: http://www-pub.iaea.org/books/IAEABooks/4710/Atomic-and-Plasma-Material-Interaction-Data-for-Fusion.

[92] P. S. Krstic and D. R. Schultz. “Elastic processes involving vibrationally excited molecules in cold hydrogen plasmas”. In: *Journal of Physics B: Atomic, Molecular and Optical Physics* 36.2 (Jan. 2003), pp. 385–398. DOI: 10.1088/0953-4075/36/2/318. URL: https://doi.org/10.1088/0953-4075/36/2/318.

[93] T. Tabata and T. Shirai. “Analyic cross sections for collisions of H^+, H_2^+, H_3^+, H, H_2, and H^- with hydrogen molecules”. In: *Atomic Data and Nuclear Data Tables* 76.1 (2000), pp. 1–25. ISSN: 0092-640X. DOI: https://doi.org/10.1006/adnd.2000.0835. URL: http://www.sciencedirect.com/science/article/pii/S0092640X00908350.

[94] R. K. Janev et al. *Elementary Processes in Hydrogen-Helium Plasmas.* Springer Series on Atoms and Plasmas. Springer, 1978.

[95] X. Si et al. “Fluid simulations of frequency effects on nonlinear harmonics in inductively coupled plasma”. In: *Physics of Plasmas* 18.3 (2011), p. 033504. DOI: 10.1063/1.3566007. URL: https://doi.org/10.1063/1.3566007.

[96] C. H. Chang and D. Bose. “Viscous effects on motion and heating of electrons in inductively coupled plasma reactors”. In: *IEEE Transactions on Plasma Science (Institute of Electrical and Electronics Engineers)* 27 (5 Oct. 1999). DOI: 10.1109/27.799807.

[97] D. P. Lymberopoulos and D. J. Economou. "Two-Dimensional Self-Consistent Radio Frequency Plasma Simulations Relevant to the Gaseous Electronics Conference RF Reference Cell". In: *Journal of research of the National Institute of Standards and Technology* 100.4 (1995), pp. 473–494. ISSN: 1044-677X. URL: https://doi.org/10.6028/jres.100.036.

[98] D. Bose et al. "A Continuum Model for the Inductively Coupled Plasma Reactor in Semiconductor Processing". In: *Journal of The Electrochemical Society* 146.7 (July 1999), pp. 2705–2711. DOI: 10.1149/1.1391996. URL: https://doi.org/10.1149%2F1.1391996.

[99] P. Scheubert et al. "Experimental and theoretical characterization of an inductively coupled plasma source". In: *Journal of Applied Physics* 90.2 (2001), pp. 587–598. DOI: 10.1063/1.1375009. URL: https://doi.org/10.1063/1.1375009.

[100] G. J. M. Hagelaar. "Fluid description of non-local electron kinetics in inductively coupled plasmas". In: *Plasma Sources Science and Technology* 17.2 (Apr. 2008), p. 025017. DOI: 10.1088/0963-0252/17/2/025017. URL: https://doi.org/10.1088%2F0963-0252%2F17%2F2%2F025017.

[101] W. Baumjohann and R. A. Treumann. *Basic Space Plasma Physics*. Revised Edition. Imperial College Press, 2012. DOI: 10.1142/p850. URL: https://www.worldscientific.com/doi/abs/10.1142/p850.

[102] R. Sperber. "Elektromagnetische Simulation der HF-Einkopplung an leistungsstarken ICPs mit Faradayschirm". MA thesis. Ostbayerische Technische Hochschule Regensburg, 2020.

[103] P. Zhao et al. "RF simulation and improvements of an ion source test facility at HUST". In: *Fusion Engineering and Design* 132 (2018), pp. 29–36. ISSN: 0920-3796. DOI: https://doi.org/10.1016/j.fusengdes.2018.05.016. URL: https://www.sciencedirect.com/science/article/pii/S0920379618304459.

[104] COMSOL AB, Stockholm, Sweden. *COMSOL Multiphysics®, version 5.6*. www.comsol.com.

[105] O. C. Zienkiewicz et al. *The Finite Element Method for Fluid Dynamics*. Seventh Edition. Oxford: Butterworth-Heinemann, 2014. ISBN: 978-1-85617-635-4. DOI: https://doi.org/10.1016/B978-1-85617-635-4.00001-7. URL: https://www.sciencedirect.com/book/9781856176354/the-finite-element-method-for-fluid-dynamics.

[106] A. Ern and J. Guermond. *Theory and Practice of Finite Elements*. Springer, New York. ISBN: 978-1-4757-4355-5. DOI: 10.1007/978-1-4757-4355-5.

[107] O. C. Zienkiewicz et al. *The Finite Element Method: Its Basis and Fundamentals*. Seventh Edition. Oxford: Butterworth-Heinemann, 2013. ISBN: 978-1-85617-633-0. DOI: https://doi.org/10.1016/B978-1-85617-633-0.00020-4. URL: http://www.sciencedirect.com/science/article/pii/B9781856176330000204.

[108] M. S. Alnæs et al. "Unified Form Language: A Domain-Specific Language for Weak Formulations of Partial Differential Equations". In: *ACM Trans. Math. Softw.* 40.2 (Mar. 2014). ISSN: 0098-3500. DOI: 10.1145/2566630. URL: https://doi.org/10.1145/2566630.

[109] P. J. Roache. *Verification and Validation in Computational Science and Engineering*. Hermosa Publishers, 1998. ISBN: 9780913478080.

[110] F. F. Chen. "Langmuir probe measurements in the intense RF field of a helicon discharge". In: *Plasma Sources Science and Technology* 21.5 (Sept. 2012), p. 055013. DOI: 10.1088/0963-0252/21/5/055013. URL: https://doi.org/10.1088/0963-0252/21/5/055013.

[111] M. J. Druyvesteyn. "Der Niedervoltbogen". In: *Zeitschrift für Physik 64* (1930), pp. 781–798. DOI: 10.1007/BF01773007. URL: https://doi.org/10.1007/BF01773007.

[112] F. F. Chen. "Langmuir probes in RF plasma: surprising validity of OML theory". In: *Plasma Sources Science and Technology* 18.3 (May 2009), p. 035012. DOI: 10.1088/0963-0252/18/3/035012. URL: https://doi.org/10.1088/0963-0252/18/3/035012.

[113] H. M. Mott-Smith and I. Langmuir. "The Theory of Collectors in Gaseous Discharges". In: *Phys. Rev.* 28 (4 Oct. 1926), pp. 727–763. DOI: 10.1103/PhysRev.28.727. URL: http://link.aps.org/doi/10.1103/PhysRev.28.727.

[114] F. Gao et al. "Comparison between experiment and simulation for argon inductively coupled plasma". In: *Physics of Plasmas* 16.11 (2009), p. 113502. DOI: 10.1063/1.3261836. URL: https://doi.org/10.1063/1.3261836.

[115] D. Ćirić. PerMag Manual (Abingdon: UKAEA Fusion/Euratom Association, Culham Science Centre). private communication. 2007.

[116] D. Bohm. *The characteristics of electrical discharges in magnetic fields*. Ed. by A. Guthrie and R. K. Wakerling. New York: McGraw-Hill.

[117] L. Spitzer. "Particle Diffusion across a Magnetic Field". In: *The Physics of Fluids* 3.4 (1960), pp. 659–661. DOI: 10.1063/1.1706104. URL: https://aip.scitation.org/doi/abs/10.1063/1.1706104.

[118] S. Sadouni. "Modélisation fluide du transport et des instabilités dans une source plasma froid magnétisé". PhD thesis. Université de Toulouse, 2020. URL: http://thesesups.ups-tlse.fr/4632/.

Acknowledgements

I would like to offer my special thanks to

- Prof. Dr.-Ing. Ursel Fantz for the opportunity to do my PhD at the Max-Planck-Institut für Plasmaphysik and for the excellent supervision and support throughout my time as a PhD student.
- Prof. Dr. Liviu Chioncel for being my second supervisor.
- Dr. Stefan Briefi for the numerous scientific and private discussions, which greatly helped me to broaden my view on various topics.
- Dr. Stiliyan Lishev for the intense and fruitful discussions about the rich ion source physics that we had during my stay at Sofia University.
- Dr. Omar Maj for always having an open door and for sharing your knowledge about the mathematical and numerical aspects of the plasma fluid theory.
- Dr. David Rauner for providing detailed and reliable experimental data, which significantly helped validating my numerical model.
- my former and present colleagues Dr. Federica Bonomo, Dr. Emile Carbone, Dr. Sofia Cristofaro, Dr. Niek den Harder, Adrian Heiler, Dr. Federico D'Isa, Dr. Roland Friedl, Dr. Ante Hecimovic, Dr. Christian Hopf, Dr. Andrew Hurlbatt, Dr. Werner Kraus, Dr. Uwe Kurutz, Max Lindqvist, Dr. Isabella Mario, Frederik Merk, Dr. Alessandro Mimo, Dr. Mauricio Montellano, Dr. Loic Schiesko, Giuseppe Starnella, Dr. Christian Wimmer, Vinzenz Wolf, Dr. Dirk Wünderlich and Dr. Dimitar Yordanov.
- the two most important persons in my life: my daughter Lara and my wife Daniela for your conditionless love, understanding and cheerfulness.